High-Resolution Photography of Clouds from the Surface: Retrieval of Optical Depth of Thin Clouds down to Centimeter Scales

Stephen E. Schwartz[1], Dong Huang[2*], and Daniela Viviana Vladutescu[3]

[1]Environmental and Climate Sciences, Brookhaven National Laboratory; ORCID 0000-0001-6288-310X. [2]Environmental and Climate Sciences, Brookhaven National Laboratory; ORCID 0000-0001-9715-6922. [3]New York City College of Technology of the City University of New York; ORCID 0000-0003-1001-533X.

Corresponding author: Stephen E. Schwartz (ses@bnl.gov)

*Current address, Science Systems and Applications Inc., Greenbelt, MD

Key Points:

- Radiance and optical depth of thin clouds are retrieved pixel-by-pixel from digital camera images at resolution of ~4 cm for cloud at 2 km
- Cloud radiance and optical depth exhibit rich spatial structure for example order of magnitude variation over 30 m × 30 m domain
- Variation in radiance on scales down to ~10 cm is attributed to variation in cloud optical depth

Abstract

This paper describes the approach and presents initial results, for a period of several minutes in north central Oklahoma, of an examination of clouds by high resolution digital photography from the surface looking vertically upward. A commercially available camera having 35-mm equivalent focal length up to 1200 mm (nominal resolution as fine as 6 μrad, which corresponds to 9 mm for cloud height 1.5 km) is used to obtain a measure of zenith radiance of a 30 m × 30 m domain as a two-dimensional image consisting of 3456 × 3456 pixels (12 million pixels). Downwelling zenith radiance varies substantially within single images and between successive images obtained at 4-s intervals. Variation in zenith radiance found on scales down to about 10 cm is attributed to variation in cloud optical depth (COD). Attention here is directed primarily to optically thin clouds, COD less than about 2. A radiation transfer model used to relate downwelling zenith radiance to COD and to relate the counts in the camera image to zenith radiance, permits determination of COD on a pixel-by-pixel basis. COD for thin clouds determined in this way exhibits considerable variation, for example, an order of magnitude within 15 m, a factor of 2 within 4 m, and 25% (0.12 to 0.15) over 14 cm. This approach, which examines cloud structure on scales 3 to 5 orders of magnitude finer than satellite products, opens new avenues for examination of cloud structure and evolution.

1 Introduction

Perhaps the most commonly accepted technical definition of a cloud is that given by the glossary of the American Meteorological Society [Glickman, 1999] as a "A visible aggregate of minute water droplets and/or ice particles in the atmosphere above the earth's surface." There is considerable merit to such a definition. All of us, scientists and non-scientists, have an inherent sense of whether a given patch of sky is cloudy or clear, or, in some instances, ambiguous. Such human observations have been made systematically by meteorological observers for decades, and the spatial and seasonal variations in the abundance of cloudiness so determined have become an important component of the record of Earth's climate [Warren et al., 1986, 1988; Eastman and Warren, 2013]. On the other hand, concerns can be raised with such a definition and mode of determination of cloudiness. The term "visible" implies a human observer, and the criterion that clouds be "visible" depends on viewing conditions and on the observer and is at best subjective and prone to large random and systematic error. In principle, and as with other atmospheric phenomena and phenomena in other disciplines of science, one might, and indeed might be encouraged to, substitute an instrumental measurement for the human observer, as such an instrumental measurement is, in principle, quantifiable and reproducible. However, even if the instrument returns some sort of a quantitative measure of cloud, the binary decision of whether a particular piece of the sky is cloudy or clear, initially reached intuitively by the observer, is replaced by an arbitrary and subjective choice of a threshold, on one side of which a piece of sky is declared clear and on the other side of which is declared cloud. As a consequence, the use of an instrumental measurement to determine the presence or absence of cloud might seem just as arbitrary as the decision of a human observer [e.g., Pincus et al., 1999; Charlson et al., 2007; Koren et al., 2007], albeit reproducible. Still, much is to be said for the use of instrumental measurements of clouds (and more generally of other observables), not just the reproducibility of the measurements, but also the ability to quantitatively relate the measurements to the physical processes giving rise to the observations and to quantitatively calculate the effects of the observed amount and properties of cloud, for example, on the amount of shortwave radiation absorbed by the earth-atmosphere system at a given time and location. As well, instrumental measurements, especially by imagers, afford the possibility of detailed characterization of cloud properties as a function of space and time.

Stimulated by the above considerations, and also by recognition of the substantial influence of clouds on short- and longwave irradiance at the top of the atmosphere, and by the necessity of accurately representing radiative and other effects of clouds in models, we initiated a project, of which the present paper is the first account, to characterize clouds by high-resolution digital photography looking vertically upward from the surface; the present analysis is limited to thin, boundary-layer cumulus clouds. Cloud properties are characterized by cloud contribution to zenith radiance. This approach has the strength of yielding a quantitative measure of the effect of clouds on radiance at the surface and affords the prospect of inverting the measured radiance to infer cloud properties. High spatial resolution is achieved with a commercially available digital camera having a nominal resolution of 6 μrad, which, for a cloud at 1 km above the surface, corresponds to a spatial resolution of 6 mm. Such a resolution is some three orders of magnitude finer than available in specialized satellite products previously used in high-resolution cloud studies (15 m, [Zhao and Di Girolamo, 2007]; 30-60 m, [Wielicki and Parker, 1992; Barker et al., 1996; Lewis et al., 2004]) and a further one to two orders of magnitude finer than resolution customarily employed in developing widely used satellite-based cloud cover products or cloud screening masks [Xi et al, 2010; Pincus et al., 2012]. Here attention must be called to an important early study using film photography to characterize the spatial variation of radiance and cloud fractal properties at scales down to 1 m [Sachs and Lovejoy, 2002]. In addition to resolution, photography from the surface looking upward affords the advantage over satellite imagery in quantitative interpretation of measured signal in that the background radiance is the black of outer space, with contributions to measured radiance only from light scattering by air (Rayleigh scattering), aerosol particles, and cloud drops, with minimal confounding contribution to the signal from surface-leaving radiance.

Here we describe the use of a commercial high-resolution, long-focal-length digital camera at a single location and for a short period of time to obtain images consisting of some 3 million independent determinations of normalized zenith radiance (zenith radiance per downwelling irradiance) in each of two color channels, red and blue. We use a radiation transfer model to invert those measurements to yield shortwave cloud optical depth (COD, the vertical integral of the scattering coefficient) for clouds of COD less than about 2 and report initial findings to show the capabilities of this approach for characterization of cloud radiance and its variation on fine spatial scales. This use of passive imaging of cloud radiance to determine cloud properties such as COD is analogous to such imaging from space by satellite-borne instruments. As the findings presented here are based on very limited observations, no inference about cloud climatology can or should be drawn. Nonetheless the observations presented here would seem to be pertinent to clouds generally, and the method presented here widely applicable to the study of clouds on such scales and capable of lending much insight into scales of variation of cloud properties.

Section 2 presents the background and motivation for this study. The theory used to invert the measurements to COD is presented in Section 3. Section 4 describes the measurements. Section 5 presents the results including inversion to yield an effective COD and examines spatial variation. Section 6 presents a discussion of results, measurement uncertainties, and implications of the findings. Conclusions and possible future directions are presented in Section 7. Details of the radiation transfer calculations, camera properties and calibrations, deployment, and supporting Doppler lidar and sun photometer measurements are presented in the Supporting Information (SI).

2 Background and motivation

Clouds exert a strong influence on absorbed shortwave and emitted longwave radiation, greatly affecting Earth's energy budget, by about -48 W m^{-2} in the shortwave and +30 W m^{-2} in the longwave [Harrison et al, 1990; Kay et al., 2012]. Such estimates rely on identification of cloud free scenes and the difference, between all-sky and cloud-free sky, of the upwelling short- and longwave radiation as measured by satellite-borne instruments. Clouds of course also are the source of precipitation. Because of the importance of clouds to Earth's climate it is recognized as essential that clouds and their radiative effects be accurately represented in models on a variety of scales, from direct numerical simulation to large eddy simulations to global-scale models of Earth's climate. In turn, assessing the accuracy of such representations requires accurate measurement of cloud extent and properties affecting radiation, importantly optical depth. For some time many climate models have exhibited an apparent error of too little cloud and, in compensation, too great an optical depth of clouds when present [Kay et al., 2012; Nam et al., 2012; Wang and Su, 2013]. However it is likely that the uncertainty associated with measurements of these properties is comparable to the apparent error between climate models and observations [Pincus et al., 2012]. Thus for many reasons much effort has been, and continues to be, directed to characterization of cloud amount and properties, and spatial distribution. Surface-based approaches may be classified as passive remote sensing by non-imaging [e.g., Chiu et al., 2006, 2009, 2010; Leblanc et al., 2015; Niple et al., 2016] and imaging techniques [Long et al., 2006; Schade et al., 2009; Li et al., 2011; Qian et al., 2012; Schäfer et al., 2013; Mejia et al., 2016; Ewald et al., 2016], and active approaches such as lidar and radar [e.g., Ansmann et al., 1992; Clothiaux et al., 2000; Mitrescu, 2005; Giannakaki et al., 2007]. Similar approaches are used in airborne in-situ and remote sensing measurements [e.g., Davis et al., 1999; McFarquhar et al., 2000; Ewald et al., 2016], and satellite-based observations [e.g., Wielicki and Parker, 1992; Stephens et al., 2002; Iwabuchi and Hayasaka, 2002; Sun et al., 2011; Kay et al., 2012; Stubenrauch et al., 2013]. Despite much effort there remain many issues associated with quantification and characterization of clouds, arising in large part out of issues of sensitivity, resolution, and threshold in determining what constitutes a cloud especially for thin clouds [Marchand et al., 2010; Pincus et al., 2012].

With respect to threshold, as pointed out by Turner et al. [2007], although clouds of liquid-water path $\lesssim$ 100 g m^{-2} (equivalently, 100 µm), commonly taken as the threshold for thin clouds, are common and can exert substantial radiative effects, they are notoriously difficult to characterize accurately. In a study over the southeast Pacific Zuidema et al. [2012] reported in 22% of the measurements the presence of thin boundary-layer clouds that were detectible by lidar but whose tops could not be detected by a sensitive cloud radar, with liquid water path mostly less than 40 g m^{-2}, which would correspond to COD roughly 5 to 10. For perspective, the disk of the sun is just discernible against the forward scattered diffuse radiation for a cloud optical thickness (path integral of scattering coefficient) of about 10 [Bohren et al., 1995]; of course such a cloud is readily discernible by a human observer. However, even much thinner clouds, optical depth 0.01 to 1, can be prevalent and are quite important radiatively [e.g., Turner et al., 2007].

Quite thin clouds (COD 0.001 to 0.3) are commonly observed in the tropics in limb observations from satellite [Wang et al., 1998]. More recently the prevalence of thin clouds has been quantified by satellite-borne lidar, CALIOP (Cloud–Aerosol Lidar with Orthogonal Polarization). Winker et al. [2008] report global cloud fraction 0.76 exceeding optical depth threshold of about 0.01, substantially greater than the value 0.61 reported from visual observations from the surface [Warren et al., 1986] and the value, also 0.61, determined by passive radiance measurements from satellite in the ISCCP project (International Satellite Cloud Climatology Project; [Rossow and Schiffer, 1999]); the greater cloud fraction seen in CALIOP observations was attributed in part to sensitivity of lidar to thin clouds. Also using data from CALIOP, Martins et al. [2011] report the fraction of lidar retrievals with clouds of COD 0.001 to 0.03 to be commonly 30% in the tropics and typically 5 - 20% in midlatitudes, depending on season and longitude. Sun et al. [2011] report cirrus having COD $\lesssim$ 0.3 detected by CALIOP as 50% globally and as present in many scenes that are reported as cloud free in satellite passive observations. In another study using CALIOP data Leahy et al. [2012] report that over the non-polar oceans, clouds with optical depth $\lesssim$ 3 comprise about 45% of clouds with cloud-top height less than 3 km, with a range, 25% to 75%, that depends on region and season. The latter investigators find as well that optically-thin marine low clouds are present predominantly as small clouds, with horizontal dimension less than 2 km.

A related topic is enhancement of aerosol scattering coefficient in the vicinity of clouds. Koren et al. [2007] presented a digital photograph showing enhanced light scattering in the vicinity of an isolated dissipating cumulus cloud that they attributed to highly humidified aerosol, noting, however, the difficulty in discriminating between aerosols and clouds and the demarcation of cloud boundaries. These investigators also showed in direct sunphotometry systematic decrease of aerosol optical depth and increase of Ångström exponent consistent with decrease in size of scattering particle with increasing time from the nearest cloud, on time scales of ~10 to 100 min (1 – 10 km for wind speed 2 m s^{-1}). Twohy et al. [2009] similarly reported enhanced relative humidity from 100 m to 4 km from cloud edge manifested in enhanced aerosol light scattering.

Despite the difficulty in detection and quantification of clouds of low optical depth, these clouds are of great radiative importance in both the shortwave and longwave, locally and instantaneously, and on account of their prevalence, globally [Sun et al., 2011, 2014]. The instantaneous shortwave CRE of a cloud of COD 0.1 is about 10 W m^{-2} (cloud-top DNSI 1000 W m^{-2}; SZA 60°) and the average shortwave CRE (24-hour average at midlatitude equinox) is about 5 W m^{-2} [e.g., Turner et al., 2007]. Such large magnitude of CRE for even such thin clouds makes it essential that the radiative effects of these clouds be accurately understood, quantified, and represented in climate models. To that end, in particular, much modeling and measurement effort [Devenish et al., 2012; Grabowski and Wang, 2013; Beals et al., 2015] is directed to characterizing such clouds and the processes responsible for their properties, for example, the influence of turbulence on the evolution of cloud drops at scales down to 1 cm in order, ultimately, to improve understanding of cloud processes and represent them in models. Finally, clouds of low optical depth are the most susceptible to increased reflectance due to anthropogenic aerosols [Charlson et al., 1992; Platnick and Twomey, 1994] with the resultant need to accurately characterize such clouds and to represent their effects in climate models.

For all the above reasons it seems evident that improvement is needed in observational characterization of clouds as input to quantifying of the effects of clouds on Earth's radiation budget, for development of model-based representation of cloud processes and properties, and for evaluation of model representations of clouds on a variety of scales. Considerations such as these have motivated the present study, of which this paper is the initial account.

Much prior surface-based imaging work for cloud characterization has been directed to determination of cloud amount, often denoted cloud fraction or fractional cloud amount [e.g., Long et al., 2006; Schade et al., 2009; Li et al., 2011]. An important exception is the study of Schäfer et al [2013], which determined COD of thin cirrus from 1-dimensional images of radiance (line image oriented orthogonal to the wind direction), inferring COD from radiance by means of a radiation transfer model; 2-D images were constructed as an array of successive line images using the mean wind speed. Mejia et al., (2016) used a three-color electronic camera with a fish-eye lens (Urquhart et al., 2015) to obtain sky images from which radiance was inverted to yield cloud optical depth images.

3 Theory

3.1 Normalized zenith radiance

We define normalized zenith radiance NZR, denoted R_λ^{nz} (unit: sr^{-1}), at a given wavelength λ as the ratio of downwelling zenith radiance $I_\lambda^{\mathrm{z}}(\mu_0)$ (W m^{-2} nm^{-1} sr^{-1}) to incident downwelling irradiance at the top of the atmosphere (W m^{-2} nm^{-1}),

$$R_\lambda^{\mathrm{nz}}(\mu_0) = \frac{I_\lambda^{\mathrm{z}}(\mu_0)}{\mu_0 F_\lambda} , \tag{1}$$

where μ_0 is the cosine of the solar zenith angle SZA and F_λ is the direct normal solar irradiance at the top of the atmosphere; this definition differs by a factor of π from that of Marshak et al. (2009). Here we specialize to two wavelengths representing red (640 nm) and blue (460 nm) wavelengths, the peak wavelengths for the red and blue channels, respectively, in the camera employed (SI, Section 2.2). The dependence of NZR at the surface on optical depth of a liquid water cloud as calculated with a radiation transfer (RT) model for several different values of SZA is shown in Figure 1. A Rayleigh atmosphere was assumed (that is, aerosols are absent) to which is added cloud of increasing optical depth. Zenith radiance was calculated with the DISORT algorithm [Stamnes et al., 1998] for a horizontally homogeneous sky with cloud drop asymmetry parameter taken as 0.85, characteristic of drop radius ~ 5 μm [e.g., Kokhanovsky, 2004] as described in SI, Section S1. Surface reflectance was taken as zero.

In the absence of cloud the only contribution to zenith radiance is Rayleigh scattering; because of the low value of Rayleigh optical depth, zenith radiance is low at both wavelengths and for all solar zenith angles, indicated by the first inset sketch in Figure 1. As cloud is added, the NZR increases as a consequence of downward scattering by the cloud, indicated by the second sketch. The increase greatest at low SZA, a consequence of the strongly forward scattering by cloud drops. The increase in NZR exceeds downward Rayleigh scattering (COD = 0) even at quite low COD, depending on wavelength and SZA. As the cloud becomes increasingly thick multiple scattering becomes increasingly important, and ultimately downward radiance decreases at the expense of upward radiance out of the top of the cloud, third sketch, with NZR peaking at COD about 1 to 4, depending mainly on SZA. It is this dependence of zenith radiance on COD that is the basis for determination of COD from radiances determined from the digital photographic images of clouds looking vertically upward.

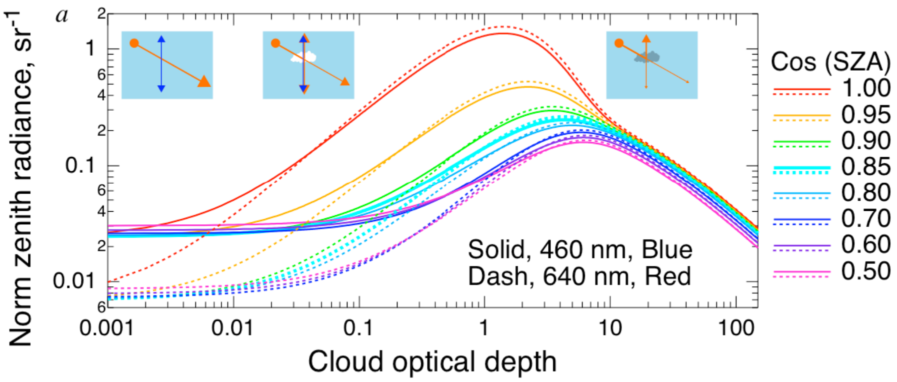

Figure 1. Double-logarithmic plot of dependence of normalized zenith radiance NZR on cloud optical depth COD at blue (460 nm, solid curves) and red (640 nm, dashed curves) wavelengths for liquid water clouds for indicated values of the cosine of the solar zenith angle cos(SZA). Radiance is normalized to incident hemispheric solar irradiance at each wavelength. Inset sketches show scattering processes contributing to zenith radiance.

A further feature seen in Figure 1 is the wavelength dependence of NZR. At low COD, NZR is much greater in the blue than the red because of the strong wavelength dependence of Rayleigh scattering. As COD increases, the relative increase is initially much greater in the red than in the blue, a consequence of the initially low radiance in the red together with the nearly wavelength-independent scattering coefficient of cloud drops. The rapid increase of Red/Blue ratio with increasing COD at low COD is the basis for cloud detection schemes using this ratio as a discriminant and is also the reason for cloud-free sky appearing blue but cloudy sky appearing white or neutral.

3.2 Determination of cloud optical depth

The dependence of zenith radiance on COD shown in Figure 1 can be inverted at a given solar zenith angle to yield COD, shown in Figure 2 as a function of NZR for 640 and 460 nm, and cos(SZA) = 0.85. At low NZR the relation is approximately linear suggesting the possibility of sensitive retrieval of COD from NZR. However with increasing NZR the curves become increasingly steep, decreasing the sensitivity of the retrieval. Ultimately, because of the maximum in the dependence of zenith radiance on COD, the same zenith radiance can result from either a thinner cloud (ascending branch of the curves in Figure 1) or a thicker cloud (descending branch of the curves) [Chiu et al. 2006]. Consequently it is necessary to ascertain whether the radiance measured in a given region of the image is from a cloud of optical depth less than or greater than the COD corresponding to the maximum normalized radiance, the so-called ambiguity problem in retrieval of COD from zenith radiance [Chiu et al., 2006; Schäfer et al., 2013; Niple et al., 2016; Mejia et al., 2016]. As COD obtained by the inversion is sensitive to zenith radiance only for clouds having COD $\lesssim$ 3, above which the COD can increase substantially with little increase in downwelling radiance, we restrict the retrievals for the present to clouds of optical depth less than about 3, depending on zenith angle, indicated by the circular markers. The inset in the figure shows the linear dependence of COD on normalized radiance and the greater relative increase (fractional increase relative to the cloud-free situation) with increasing COD at low COD exhibited by the red radiance than by the blue. As the inference of COD from NZR is based on a radiative transfer model that assumes horizontal homogeneity the retrieval should be restricted to clouds that meet this requirement. In the present study use of this model for retrieval of COD gains justification by the restriction of the retrieval to situations of single, optically thin layer clouds, in which single scattering dominates the downwelling radiance, manifested by the near linearity of the relation between COD and NZR shown in Figure 2 for COD $\lesssim$ 2.

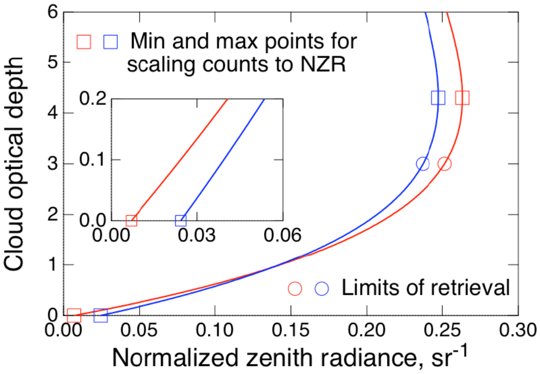

Figure 2. Dependence of cloud optical depth COD on normalized zenith radiance for red (640 nm) and blue (460 nm) wavelengths for liquid water clouds for cos (SZA) = 0.85 used in retrieval of COD from scaled normalized zenith radiance derived from images. Circular markers for COD = 3 denote maximum value of COD that is considered confidently retrieved on account of increasing slope. Square markers denote minimum (Rayleigh) and maximum (bright cloud) values of NZR that are used in two point calibration of camera counts to NZR. Inset shows dependence of COD on normalized radiance at low COD.

The use of counts from the red and blue channels of the images results in two independent determinations of the radiance field and in turn the COD field for each pixel of each image. This independent determination of two related quantities (or of the same quantity) provides a means of examining the consistency of the retrievals. Shown in Figure 3 is the relation between NZR in the blue and the red; the two branches of the relation refer to low COD (COD $\lesssim$ 4, depending on SZA; ascending branch of the curve) and high COD ($\gtrsim$ 4; descending branch). At low COD blue radiance substantially exceeds red radiance in a relative sense (Figure 1); at intermediate COD red slightly exceeds blue, and for thick clouds (COD $\gtrsim$ 10) the radiances at the two wavelengths become essentially equal. Figure 3 serves as a framework for assessment of the retrieval of the radiances obtained from the images.

Figure 2 displays a further feature of the radiative transfer calculations that is central to quantitative interpretation of the camera images. Specifically for each color, blue and red, the figure shows, by the square markers, the minimum (Rayleigh scattering) and maximum (brightest cloud) values of NZR that can result from any amount of cloud in the overhead column. These two points thus provide a two-point calibration of NZR from counts in the blue or red channels of the camera. Consequently, in a series of photos that encompass situations that extend from cloud free to bright cloud to thick (darker) clouds, identification of the regions in the images that are characterized by minimum and maximum counts, allows, to the accuracy of the RT calculations, scaling of counts to NZR for each pixel in the image. In carrying out these calibrations it is important to confirm that the bright regions are representative of relatively uniform regions of the cloud, avoiding any silver-lining effect at cloud edge, and that the dark regions are not influenced by shadowing; this confirmation is greatly facilitated by inspection of the images.

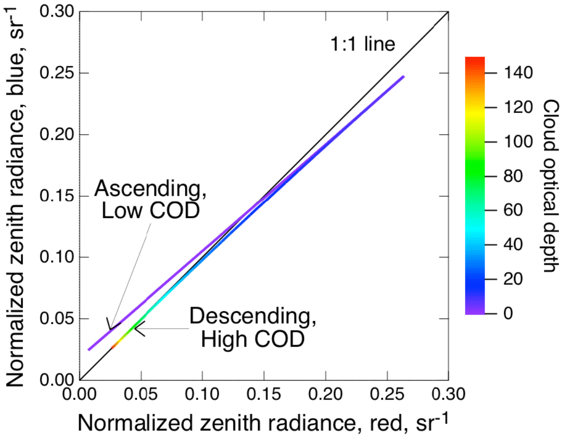

Figure 3. Normalized zenith radiance at the blue wavelength versus that at red wavelength, for cos(SZA) = 0.85; color indicates cloud optical depth.

Calibration of counts to NZR by this procedure automatically accounts for both the camera sensitivity and the solar spectral irradiance at the top of the atmosphere at the time of the measurement (a function of SZA on any given day, and also of Earth-Sun distance), yielding the values of NZR in the two (blue and red) channels of the camera, peaking respectively at 460 and 640 nm (SI, Section S2.2), from the counts in cloud-free and cloudy regions of one or multiple images. Specifically, the normalized zenith radiance R_{s} is obtained for both the red and blue channels on a pixel-by-pixel basis from the count rate in each pixel as

$$R_{\mathrm{s}} = R_{\min} + \frac{C - C_{\min}}{C_{\max} - C_{\min}} (R_{\max} - R_{\min}) \, . \tag{2}$$

Here C denotes red or blue counts in a given pixel of one or more camera images. $C_{\min}$ and $C_{\max}$ denote the minimum and maximum counts in the images, corresponding to cloud-free and maximum-brightness cloud pixels, respectively; determination of $C_{\min}$ and $C_{\max}$ thus requires identification of a nominally cloud-free region and of a region of maximum cloud brightness, respectively, in a single image or in temporally proximate images. $R_{\min}$ and $R_{\max}$ similarly denote the NZR determined from the RT calculations in the absence of cloud and at the maximum brightness as COD is increased, respectively, at the pertinent solar zenith angle. The calibration determined in this way is expected to be transferrable to temporally proximate images with approximately constant solar geometry. Using a cloud-free region in the image itself to determine $C_{\min}$ implicitly accounts for contribution to zenith radiance from aerosols, the contributions to radiance from clouds and aerosols being nearly additive at the low optical depths for which the method is applicable. The ability to determine NZR from the camera counts for each pixel (and separately for the red and blue channels) in turn permits determination of COD from the data for each channel on a pixel-by-pixel basis by means of the dependence of COD on NZR shown in Figure 2.

As the RT model used to invert radiance to COD is based on plane parallel horizontally uniform geometry (1-D), the COD retrieved from the images is denoted an effective COD, ECOD, that is potentially subject to 3-D effects. Here we analyze the radiance field as if it were plane parallel (independent pixel approximation) and return to concerns over this assumption in the discussion.

4 Measurements

4.1 Cameras

The cameras employed in this study were Fujifilm FinePix, model S1, which retails for less than \$400. This model, which was selected primarily because of the zoom telephoto lens which at maximum zoom is equivalent to a 1200 mm lens on a standard 35-mm film camera, yields a nominal resolution (angular field of view divided by number of pixels) of approximately 6 μrad and an actual resolution (as governed by camera optics and demonstrated by measurement) of about 20 μrad (SI, Section 2.1), corresponding, respectively to 6 mm and 20 mm for a cloud at 1 km altitude, making it very well suited for study of cloud structure at high spatial resolution. In the measurements reported here the cameras were deployed vertically (zenith) pointing, with 35-mm equivalent focal lengths 1200 mm and 217 mm (actual focal lengths 215 and 38.8 mm, respectively). At these two focal lengths the field of view of an image is 21 × 29 mrad and 120 × 160 mrad, respectively, denoted here narrow field of view, NFOV, and wide field of view WFOV. For perspective, the FOV for the NFOV camera is 2 × 3 sun diameters and for the WFOV camera 11 × 15 sun diameters. For the number of pixels in the sensor 3456 × 4608 (15.9 Mpixel), the angular resolution of a single pixel is 6.2 and 34 μrad for the NFOV and WFOV cameras, respectively. By comparison the resolution of the human eye, 0.3 arc-min [Clark, 2016], corresponds to 90 μrad; thus at highest zoom the camera might be considered equivalent to a 15 × telescope with FOV 22 × 29 m at 1000 m. Numerical aperture was *ƒ*/8 at both focal lengths. The actual length of the lens, about 100 mm (SI, Figure S11) is much less than that of an actual 1200-mm focal-length 35-mm lens, a consequence of folded optics and of the smaller sensor size (4.55 mm × 6.17 mm) than that of the standard 35 mm film image (24 mm × 36 mm). A 1200-mm, *ƒ*/5.6 lens for a standard 35 mm camera was manufactured in the late 1990's, and one such lens recently appeared on the used photographic equipment market for \$180,000 [Barron, 2015].

The camera sensor consists of a 3456 × 4608 (~16 M pixel) pixel array with sensors masked by red, green, or blue filters (Bayer pattern), so that only 1/4 of the pixels are red and 1/4 blue; the resultant image is interpolated yielding 3456 × 4608 × 3 sets of 16-bit numbers corresponding to the intensities (measured as counts) in each of the red, green, and blue (RGB) channels. The maximum sensitivities of the blue and red channels used for analysis of cloud contribution to observed radiance are at 460 and 640 nm, with minimal overlap (SI, Section S2.2); here we do not make use of the green channel data, which are largely redundant with the blue and red channel data. The dynamic range of counts C in an individual pixel is 0 to (2^{16} - 1), i.e., 0 to 65,535. Images are obtained initially in a proprietary "raw" format and converted by software provided with the camera (Raw File Converter EX, https://silkypix.isl.co.jp/en/) to tiff (Tagged Image File Format). As the image produced by the software exhibits a sublinear relation between radiant intensity and counts to artificially increase the dynamic range of digital photographs to enhance their visual appeal, it is necessary to calibrate the camera against a light source of variable intensity to linearize the counts, as described in SI, Section S2.3. Although the tiff images are quite large (96 Mbyte for 16-bit RGB 16 megapixel image) compared to compressed images such as the widely used jpeg (Joint Photographic Experts Group) format, the tiff format retains the count information of each individual pixel, instead relating that intensity to that of adjacent pixels, which would compromise analysis of spatial variation of counts and derived quantities. Tiff images are readily ingested by commercial graphics and image analysis software. The original rectangular images were trimmed to the central 3456 × 3456 pixels (~12 M pixel) for quantitative intensity analysis to avoid vignetting. Because only one in four pixels is red or blue the number of independent determinations of red or blue radiant intensity is 3 million. All the analyses reported here were carried out with the Igor Pro software package (www.wavemetrics.com), which ingests the RGB tiff image and permits extraction of count numbers C in each of the three channels as two-dimensional matrices representing the x and y coordinates of the image, algebraic manipulation of these quantities, further display of derived quantities as false-color images, zooming in on selected regions of images, calculation and display of line profiles and the like.

Because of production limitations most images in the printed and electronic versions of this article exhibit resolution that is greatly reduced from that of the original images and of false-color images of quantities derived from the original images. However the original resolution of the images is preserved in figures available from the journal website and linked to the electronic version of this paper.

4.2 Deployment

Measurements reported here were conducted at the Department of Energy's Atmospheric Radiation Measurement (ARM) Southern Great Plains (SGP) site in north central Oklahoma (36.6˚N, 97.5˚W, altitude 317 m) [Stokes and Schwartz, 1994; Mather and Voyles, 2013] to take advantage of other ongoing measurements at that site pertinent to characterizing the atmospheric state, clouds, and radiation. Cameras were located within 2 m of a Doppler lidar. Cameras were leveled to within 1.7 mrad of vertical. Images are oriented with top of image to the North; as one is looking “upward” at a given image East is on the left, West on the right, and South at the bottom of the image. Cameras were focused manually on a distant object, rather than using autofocus, which has difficulty focusing on fuzzy objects such as clouds. Exposure time was 1/2000 s, electronically controlled by the camera. Digital photographs were taken at automated 4-s intervals, the frequency being limited by the write speed of the data to the storage medium. Time of the photograph was recorded on the internal clock of each camera, which was calibrated regularly against a web-based UTC server, with slight drift of the internal clocks compensated by interpolation; times are considered accurate to ± 2 s. Images were obtained typically for periods of 3 hours on 13 days from mid July through August, 2015. Further description of the deployment is given in SI.

Other key measurements were a Doppler lidar (wavelength 1.5 µm; range gate, 30 m; integrating time, 1 s; full angle field of view, 66 µrad; Pearson et al., 2009) for detection of aerosols and clouds, determination of cloud heights, and determination of atmospheric vertical velocity; multi-filter rotating shadow band radiometer (MFRSR) [Harrison et al., 1994] for cloud detection and aerosol optical depth; and Cimel sun photometer [Holben et al., 1998] for aerosol optical depth.

5 Observations and analysis

5.1 Qualitative observations

Time series of images taken mid-morning, local time, July 31, 2015 are presented in Figure 4 for the wider FOV camera and in Figure 5 for the narrow FOV camera. Times indicated (16:33 - 16:40) and throughout this paper are UTC; at the longitude of 97.5°W, local sun time lags UTC by 6.5 hours. Successive images are at 4-s intervals; one row of images corresponds to 1 min, and each panel represents a 7-min interval. The spatial domain represented by the images is calculated from the camera FOV and cloud height determined by the Doppler Lidar (discussed below). For cloud height 2 km the FOVs are 240 × 320 m for the wider FOV camera and 42 × 58 m for the narrow FOV camera. Substantial variation in cloud amount within a given image is evident in many of the images. The time period represented in these images was selected for detailed analysis here, in part because of the high variation exhibited between periods of complete coverage by small cumulus humilis clouds (within the limited field of view of the images) to apparent cloud free, with numerous instances of broken clouds and cloud edges, a common situation during a 6-week deployment at the SGP site in July-August, 2015. Advection of clouds is seen in translation of identifiable cloud features in successive images from right to left (West to East) and, to lesser extent, from bottom to top (South to North). Identification of cloud features in proximate images permits calculation of an angular translational velocity, found, for images 3156-3160 with the WFOV camera, to be 1.8 and 0.88 mrad s^{-1} eastward and northward, respectively. For cloud height 2 km, this corresponds to translational velocity 3.6 and 1.8 m s^{-1}, respectively. Wind speeds determined in this way agree rather closely with those obtained from the drift rate of a radiosonde launched about one hour later, Figure S15 in SI, confirming attribution of translation of cloud features to advection.

Determination of the translational velocity also permits assessment of translational blurring during the time of exposure of an image. For an angular translational velocity of 2 mrad s^{-1} and exposure time of 1/2000 s the angular translation is 1 μrad, well less than the resolution of 6.2 and 34 μrad for the NFOV and WFOV cameras, respectively, establishing that such blurring is negligible.

Figure 4. Time series of photographs taken with wide FOV camera at the Department of Energy Atmospheric Radiation Measurement site in Oklahoma on July 31, 2015. Images are in RGB (red-green-blue) natural color. Angular dimension is 120 × 160 mrad corresponding to 240 × 320 m for cloud height 2 km. Images are oriented with North at top, East at left, West at right, and South at bottom. Time is UTC; 16:33 UTC corresponds to 10:03 local sun time. Successive images, serially numbered by camera, are taken at 4-s intervals; one row (15 images) corresponds to one minute and the total elapsed time is 7 min. Red rectangle in Image 3162 denotes locations of corresponding images with narrow-field-of-view camera, Figure 5.

Figure 5. Time series of photographs taken with narrow FOV camera, as in Figure 4. Angular dimension is 21 × 29 mrad corresponding to 42 × 58 m for cloud height 2 km. Red square in Image 1042 denotes central 3456 × 3456 pixel region used in quantitative analysis of the images.

[Figures are shown on succeeding 2 pages]

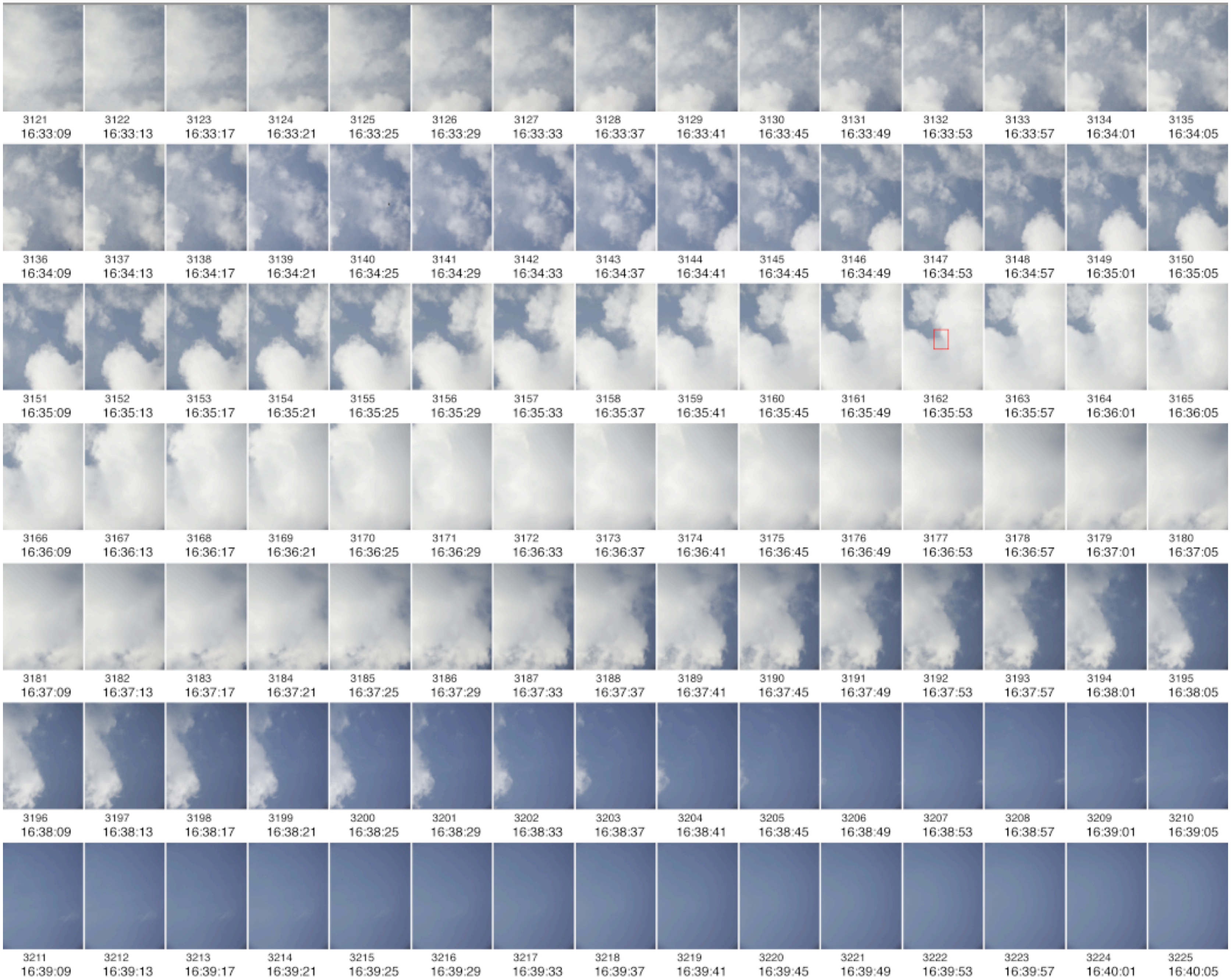
3121 16:33:09
3122 16:33:13
3123 16:33:17
3124 16:33:21
3125 16:33:25
3126 16:33:29
3127 16:33:33
3128 16:33:37
3129 16:33:41
3130 16:33:45
3131 16:33:49
3132 16:33:53
3133 16:33:57
3134 16:34:01
3135 16:34:05
3136 16:34:09
3137 16:34:13
3138 16:34:17
3139 16:34:21
3140 16:34:25
3141 16:34:29
3142 16:34:33
3143 16:34:37
3144 16:34:41
3145 16:34:45
3146 16:34:49
3147 16:34:53
3148 16:34:57
3149 16:35:01
3150 16:35:05
3151 16:35:09
3152 16:35:13
3153 16:35:17
3154 16:35:21
3155 16:35:25
3156 16:35:29
3157 16:35:33
3158 16:35:37
3159 16:35:41
3160 16:35:45
3161 16:35:49
3162 16:35:53
3163 16:35:57
3164 16:36:01
3165 16:36:05
3166 16:36:09
3167 16:36:13
3168 16:36:17
3169 16:36:21
3170 16:36:25
3171 16:36:29
3172 16:36:33
3173 16:36:37
3174 16:36:41
3175 16:36:45
3176 16:36:49
3177 16:36:53
3178 16:36:57
3179 16:37:01
3180 16:37:05
3181 16:37:09
3182 16:37:13
3183 16:37:17
3184 16:37:21
3185 16:37:25
3186 16:37:29
3187 16:37:33
3188 16:37:37
3189 16:37:41
3190 16:37:45
3191 16:37:49
3192 16:37:53
3193 16:37:57
3194 16:38:01
3195 16:38:05
3196 16:38:09
3197 16:38:13
3198 16:38:17
3199 16:38:21
3200 16:38:25
3201 16:38:29
3202 16:38:33
3203 16:38:37
3204 16:38:41
3205 16:38:45
3206 16:38:49
3207 16:38:53
3208 16:38:57
3209 16:39:01
3210 16:39:05
3211 16:39:09
3212 16:39:13
3213 16:39:17
3214 16:39:21
3215 16:39:25
3216 16:39:29
3217 16:39:33
3218 16:39:37
3219 16:39:41
3220 16:39:45
3221 16:39:49
3222 16:39:53
3223 16:39:57
3224 16:40:01
3225 16:40:05


1001 16:33:12
1002 16:33:16
1003 16:33:20
1004 16:33:24
1005 16:33:28
1006 16:33:32
1007 16:33:36
1008 16:33:40
1009 16:33:44
1010 16:33:48
1011 16:33:52
1012 16:33:56
1013 16:34:00
1014 16:34:04
1015 16:34:08
1016 16:34:12
1017 16:34:16
1018 16:34:20
1019 16:34:24
1020 16:34:28
1021 16:34:32
1022 16:34:36
1023 16:34:40
1024 16:34:44
1025 16:34:48
1026 16:34:52
1027 16:34:56
1028 16:35:00
1029 16:35:04
1030 16:35:08
1031 16:35:12
1032 16:35:16
1033 16:35:20
1034 16:35:24
1035 16:35:28
1036 16:35:32
1037 16:35:36
1038 16:35:40
1039 16:35:44
1040 16:35:48
1041 16:35:52
1042 16:35:56
1043 16:36:00
1044 16:36:04
1045 16:36:08
1046 16:36:12
1047 16:36:16
1048 16:36:20
1049 16:36:24
1050 16:36:28
1051 16:36:32
1052 16:36:36
1053 16:36:40
1054 16:36:44
1055 16:36:48
1056 16:36:52
1057 16:36:56
1058 16:37:00
1059 16:37:04
1060 16:37:08
1061 16:37:12
1062 16:37:16
1063 16:37:20
1064 16:37:24
1065 16:37:28
1066 16:37:32
1067 16:37:36
1068 16:37:40
1069 16:37:44
1070 16:37:48
1071 16:37:52
1072 16:37:56
1073 16:38:00
1074 16:38:04
1075 16:38:08
1076 16:38:12
1077 16:38:16
1078 16:38:20
1079 16:38:24
1080 16:38:28
1081 16:38:32
1082 16:38:36
1083 16:38:40
1084 16:38:44
1085 16:38:48
1086 16:38:52
1087 16:38:56
1088 16:39:00
1089 16:39:04
1090 16:39:08
1091 16:39:12
1092 16:39:16
1093 16:39:20
1094 16:39:24
1095 16:39:28
1096 16:39:32
1097 16:39:36
1098 16:39:40
1099 16:39:44
1100 16:39:48
1101 16:39:52
1102 16:39:56
1103 16:40:00
1104 16:40:04
1105 16:40:08

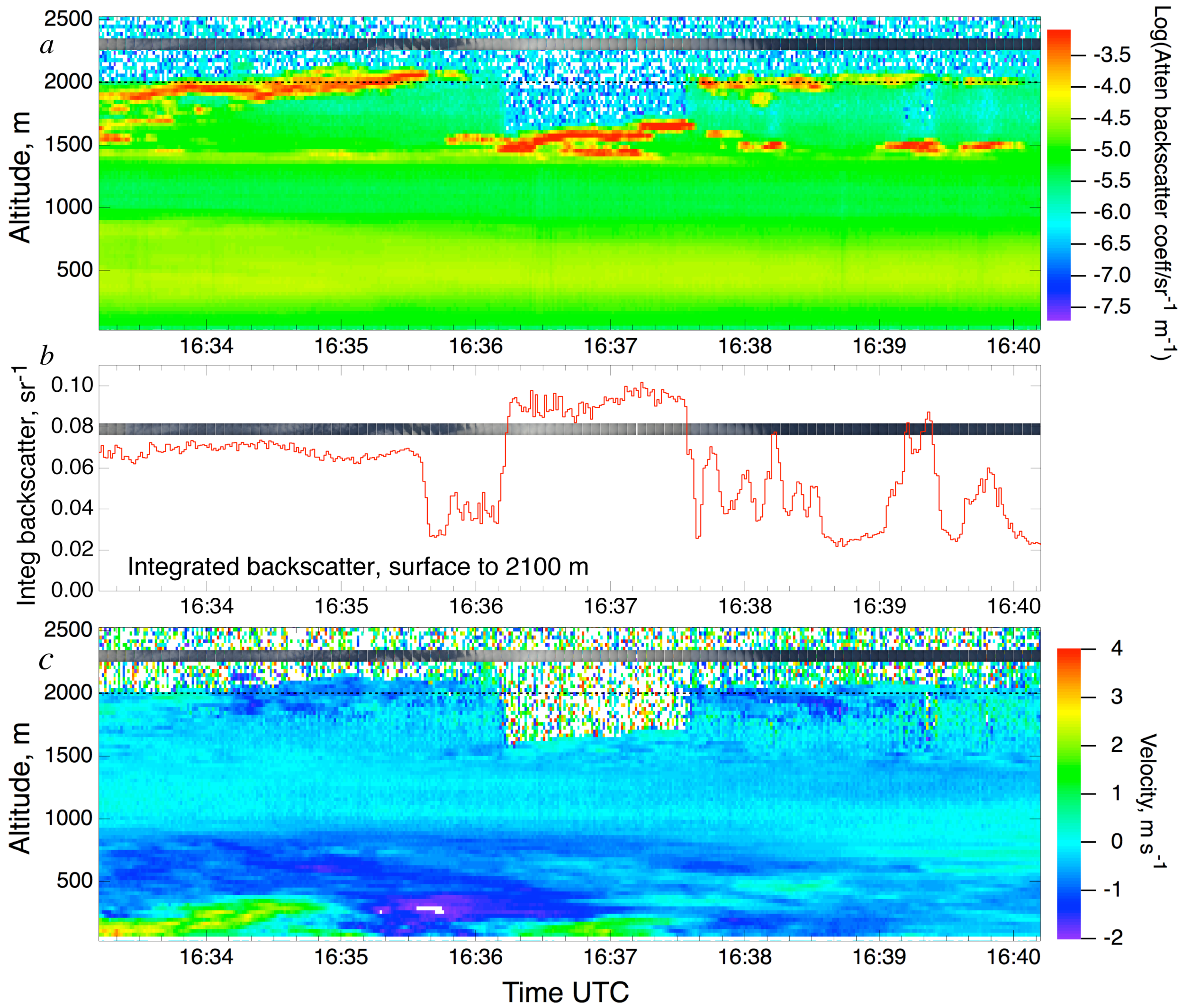

Figure 6. Doppler lidar measurements for the 7-min period 16:33:12 to 16:40:12 corresponding to the images presented in Figures 4 and 5; images from NFOV camera as function of time are superimposed on each panel. (*a*) Time-height profile of attenuated backscatter signal from Doppler Lidar. Color scale denotes logarithm (base 10) of return signal; white is below minimum value on color scale. Vertical scale denotes height above ground level. Dashed line at 2 km is shown for reference. (*b*) Vertically integrated lidar return from surface to 2.1 km over same time period. (*c*) Time-height profile, as in *a*, of vertical velocity (positive upward). White indicates absence of return signal or velocity less than minimum value on color scale. Citation to Doppler Lidar data in SI.

Valuable context for the atmospheric state at the time of these images and for interpretation of the images is provided by the Doppler Lidar, which yields time-height profiles of back-scattered intensity and vertical velocity, Figure 6; the wavelength of the lidar, 1.5 µm, minimizes return from Rayleigh scattering, emphasizing return from aerosols and clouds. Cloud layers are indicated by the regions of intense return (attenuated backscatter coefficient ~$10^{-3.5}$ sr^{-1} m^{-1}), for which the vertical profiles of returned intensity showed a strong peak at cloud altitude of 2 km above the surface, Figure 7*a*. The lidar return from an aerosol layer extending from the surface to about 1 km was much weaker than that from the clouds. This signal was temporally much more uniform than that from the clouds, consistent with a relatively uniform aerosol loading; the slight variation in aerosol over the 7-min period, and indeed over the several hour period of the measurements (SI), is likely due more to variation in relative humidity than to variation in aerosol loading. A second aerosol layer (or nascent cloud layer) at about 1.5 km briefly developed into a thin cloud layer from about 16:35:40 to 16:37:30, which then dominated the return signal in the vertical profiles, as shown in Figure 7*b*. As the cloud layers were fairly opaque to the outgoing beam and as any returned scattered light from above these cloud layers was quite weak and noisy, it is difficult to state with confidence that the low return signal from above the cloud was representative of low scattering coefficient above the cloud layers. However there were instances of apparent "holes" in the clouds, e.g., around 16:38:40, for which the vertical profiles, Figure 7*c*, showed little signal from cloud; the minima in attenuated backscatter signal are seen also in the integrated lidar return, Figure 6*b*. For these situations the transmittance through the cloud layers was sufficiently high that it can be inferred that the return from above 2 km is indicative of the absence of any significant aerosol or clouds above 2 km; this conclusion is supported also by the sounding, Figure S15. These observations support the conclusion that in the time period 16:34:00 – 16:35:30 the clouds consisted of a single thin layer at about 2 km and, as indicated by the associated negative vertical velocities, weakly dissipative.

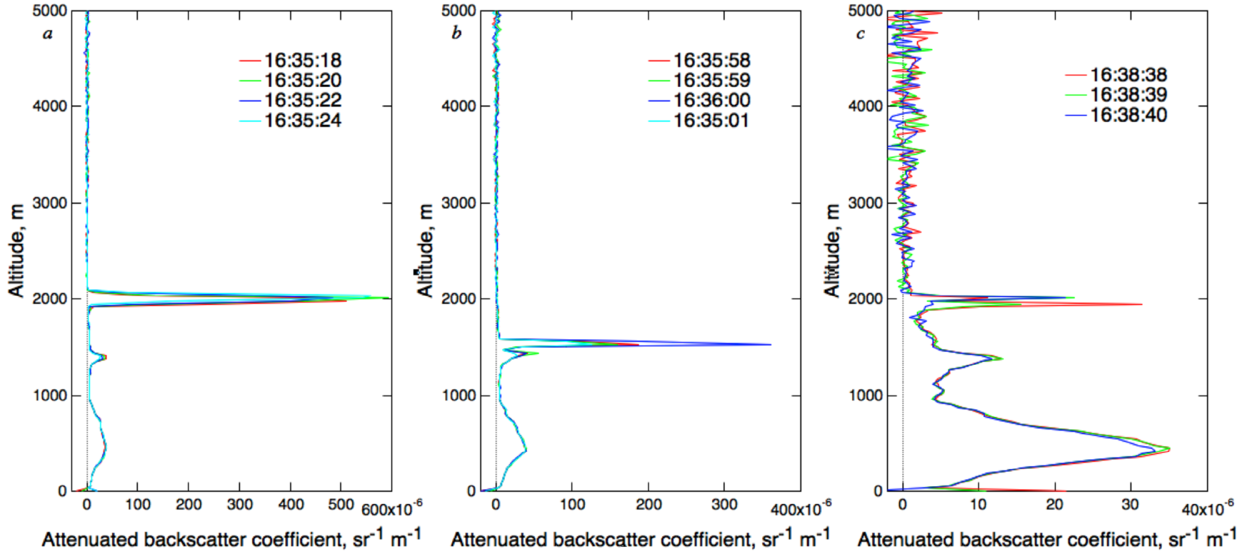

Figure 7. Vertical profiles of attenuated backscatter signal from Doppler Lidar for indicated times, corresponding to cloud layers at 2 km (*a*) and 1.5 km (*b*) and near absence of clouds (*c*). Each profile denotes a 1-s average. Vertical scale denotes height above ground level. Note differences in backscatter scales. Citation to Doppler Lidar data in SI.

It may be noted that the lidar signals in Figure 6 disagree slightly from expectation based on the images in Figure 5, superimposed as a strip of miniature images on each of the panels of Figure 6. For example the period of high integrated lidar return in panel *b* commencing at about 16:36:00 seems to lag the period of maximum brightness in the cloud images by some 20 s. Such disagreement can occur for several reasons Although the instruments are separated by only about 2 m, there is possible mismatch in orientation to the vertical; both the lidar and the cameras are nominally within 0.1° ≈ 1.7 mrad of the vertical which compares to the angular width of the image in the NFOV camera of about 22 mrad. The width of the lidar beam 66 μrad is about equal to 10 pixels of an NFOV image or 0.3% of the image width. Also, the lidar signals are 1-s averages versus the exposure times for the digital photographs of 0.5 ms; a wind speed 4 m s^{-1} at height of 2 km would result in translation of the cloud by about 4 m or 2 mrad for cloud height 2 km. This represents about 300 pixels or about 10% of a NFOV image. In contrast, for 0.5 ms exposure by the camera, the translation distance is 2 mm or about 0.16 pixel. Finally there is a systematic uncertainty in the time stamp of the camera images of about ± 2 s.

Optical depth was measured by a multifilter rotating shadowband radiometer (MFRSR) and by a Cimel sun photometer. As both measurements are made along the direct line of sight to the sun, they can be taken only as indicative of the general state of cloudiness at the time and location and not as measures of the clouds vertically above the cameras at the time of the photographs, the sun being well outside the field of view of the cameras, Figure S12. The MFRSR returned signal during much of the period 16:00 - 17:00 (SI, Section S4), with optical depth at 500 nm 0.4 to 0.5, but with excursions up to 1.5 earlier in the hour and 1.0 at 16:34:00; the high excursions were characterized by low Ångström exponent (0 - 0.2) indicative of optically thin clouds.

Additional perspective to the atmospheric state is provided by the radiosonde, Figure S15, which shows a region of high relative humidity between 1000 and 2000 m altitude above the surface, consistent with cloud height determined by lidar. Despite indication in the sounding of RH never reaching 100%, thin clouds were consistently present above the SGP site throughout the time period of the sonde rising through the 2000 m level. Based on the sounding the atmosphere is neutral to slightly stable at the altitude of the aerosol and cloud layers, supporting interpretation of the clouds as weakly dissipative.

5.2 Quantitative examination of images

This section examines selected cloud photographs and derived quantities and presents analysis and interpretation of these images. Perforce the number of images that can be presented and discussed here is limited. The intent is to illustrate the analyses conducted and to focus on several images of particular interest within the time series represented in Figure 5. Attention is called first to Figure 8*a*, which shows the RGB image of the central portion (3456 × 3456 pixels) of Image 1042 obtained with the NFOV camera, Figure 5. This image is selected as an example of a scene that encompasses a wide range of cloudiness within the small portion of the sky encompassed by the camera field of view (Figure S12), from low cloud in the upper left (northeast corner of the scene) to bright cloud in the upper right. A broader context of this image is shown in Image 3162 obtained with the WFOV camera, Figure 4, with the region encompassed by the NFOV image demarcated by the red rectangle. Greater visual contrast is obtained with the red channel image, Figure 8*b*. A quantitative rendering of the red-channel image is given by the false color image of the linearized counts, panel *c*; here the range of the color scale and of the image itself encompasses the entire range of the counts in the image; that range can be adjusted to bring out features of interest. The number of counts in this channel ranges from about 4000 to about 36,000, almost an order of magnitude, spanning a large fraction of the 16-bit dynamic range of the camera, 0 - 65,535. (The blue-channel image, not shown, is qualitatively similar.) Strong gradients are readily identified in the image and read off from the color scale. In addition to the overall gradient from upper left to upper right, there is evidence throughout the image of structure in the radiance field at finer scales. The length scale bar shows the horizontal distance calculated from the camera field of view, 21.5 mrad × 21.5 mrad, and the height of the cloud, 1.5 km, determined from the lidar (Figures 6, 7), from which it is seen that there can be substantial variation in the cloud at horizontal scales of 5 m and below, discussed in Section 5.8.

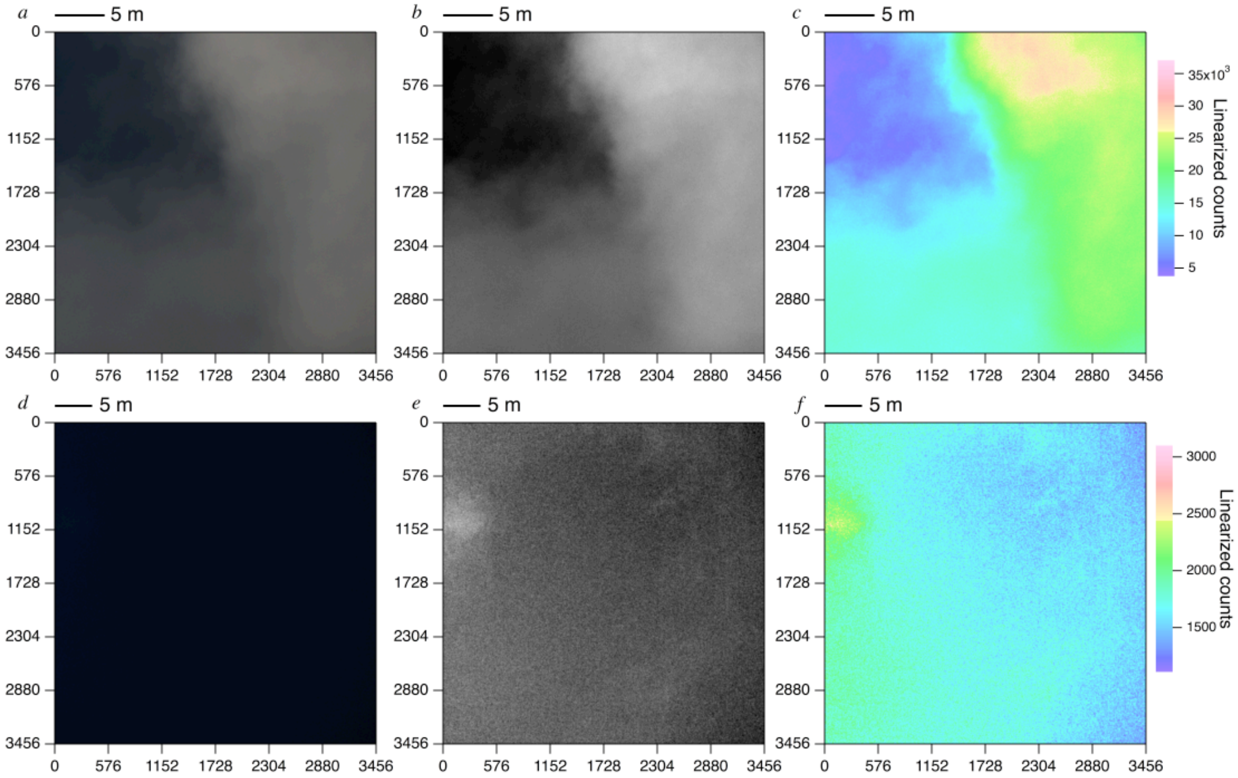

Figure 8. Multiple depictions of radiance field from narrow-field-of-view images for a bright cloud (Image 1042, 16:35:56, *a*-*c*) at 1.5 km (Figure 7*b*) and for a dark, largely cloud-free image (Image 1080, 16:38:28, *d*-*f*) at 2 km (Figure 7*c*). Vertical and horizontal axis scales denote pixels; one pixel corresponds to 6.2 µrad, or 9.3 mm and 12.4 mm for cloud height 1.5 and 2 km, respectively; length scale bars denote horizontal scale at those heights. Image dimensions are 32 × 32 m and 43 × 43 m, respectively. (*a*), (*d*) RGB; (*b*), (*e*) red channel shown in grayscale; (*c*), (*f*) red channel shown in false color, with linearized counts indicated by color scale at right; note different color scales for the two images.

A second example is image 1080; as discussed in Section 5.3, this image is the darkest in the series of images shown in Figure 5, and thus assumes some importance in the further analysis. Although no cloud is evident in the RGB image, panel *d*, examination of the red channel in gray scale or in false color reveals a bright spot at the left of the image, that appears to be a small thin cloud, as well as a gradient across the image; the maximum effective optical depth of this cloud, determined as described in Section 5.5 is about 0.13. The range of counts comprising image R1080 is much lower than for image R1042 (the prefix R denotes the red channel). Comparison with images immediately preceding, Figure 9, shows the same cloud translating from the center of the image to the left (eastward). The windspeed components calculated from the angular velocity at height of 2 km, which height is exhibiting the greatest magnitude lidar return at that time (Figure 7) are 1.4 m s^{-1} eastward and 0.12 m s^{-1} northward, consistent with lower wind speed at this height seen in the sounding (Figure S15).

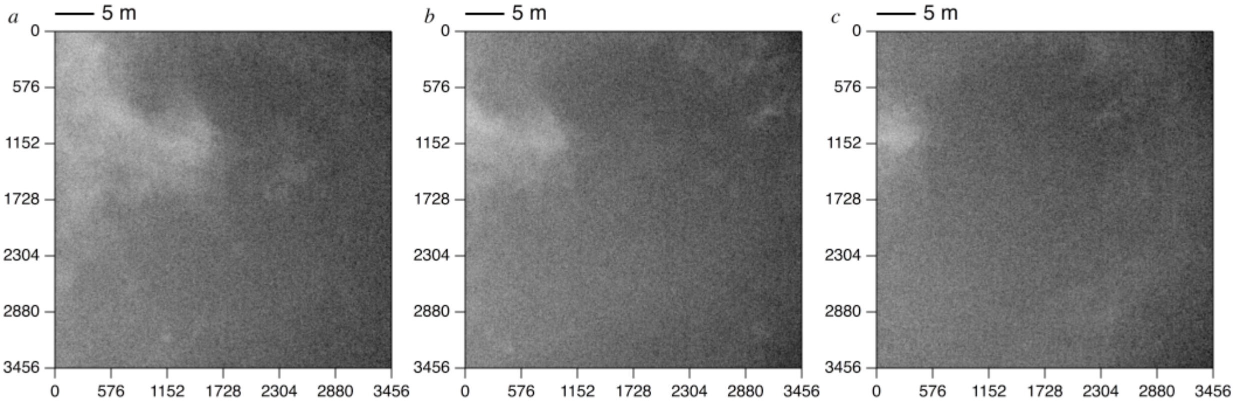

Figure 9. Successive images (grayscale display of red channel linearized counts) at 4-s intervals showing translation from right to left (West to East) of apparent cloud in dark image. (*a*) R1078; (*b*) R1079; (*c*) R1080. Length scale bars are evaluated on assumption that cloud height is 2 km.

5.3 Determination of scaling parameters

Inverting linearized counts measured by the camera to optical depth first requires relating the linearized counts in the several channels of the images to the normalized radiance as described in Section 3. For this purpose we use the brightest and darkest regions in a series of images that span the range of cloud-free to COD sufficiently great as to encompass the maximum in normalized radiance shown in Figures 1-3 to determine scaled normalized radiance by Eq. (2). It is therefore necessary first to identify the minimum and maximum values of linearized counts in such a series of images, as outlined here. It must be recognized that even in the darkest images there will inevitably be contributions to zenith radiance from any aerosol that is present, as well as from any residual unrecognized cloud. From the perspective of determination of COD, the contribution to radiance from aerosol in the darkest region used to set the zero of the scaled radiance would simply raise the floor of the minimum radiance and thus not contribute to determined COD. However the presence of any unrecognized or nascent cloud in the darkest region would artificially raise the zero of the scaled radiance, and as a consequence the COD determined by this procedure would be less than the actual COD by the optical depth of whatever cloud is present in the nominally cloud-free region used to set the scale.

The distribution of counts in a given image or set of images is conveniently examined by histograms, Figure 10. Panel *a* shows the histogram for image R1042, (Figure 8*a-c*) which spans much of the region between fairly cloud free and fairly bright cloud, as manifested by the rather broad histogram. The histogram for the red channel of the nearly cloud-free image R1080 exhibits much lower counts, and a single peak, indicative of the much greater uniformity of the intensity over the image. The breadth of the PDF for this image is indicative mainly of the gradient across the image noted above, as seen by comparison of the color bar with the colors in Figure 8*f*. The integral of the histogram, denoted $F_{<C}$ and plotted as a function of counts C, gives the fraction of pixels having counts lower than C; the complement of this quantity, denoted $F_{<C}$, gives the fraction of pixels having counts greater than C. A flat value of either integral over a certain range would mean few pixels with counts at that range of C, for example if there were a distinct region in the distribution function of few counts between a cloud-free and cloudy region.

Such a situation is not observed in the histograms of either of the two images and indeed is quite rare in the histograms of the clouds examined.

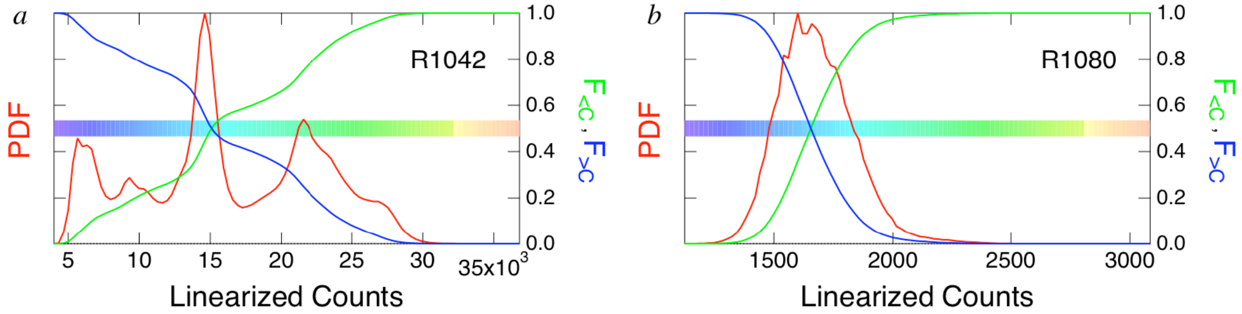

Figure 10. (*a*) Histogram (normalized probability distribution function, PDF, red) of numbers of pixels having linearized counts C in red channel of image R1042 versus C. Color bar corresponds to color scale in false-color image of that quantity, Figure 8*c*. $F_{<C}$, green, denotes integral of PDF from 0 to C, the fraction of pixels having linearized counts less than C; and $F_{>C}$, blue, denotes the complement of $F_{<C}$, the fraction of pixels having linearized counts greater than C. (*b*) As in *a*, for image R1080; color bar corresponds to Figure 8*f*.

A key objective was to identify within the series of photographs regions of maximum and minimum cloud contribution to radiance needed to anchor the scaling of the uncalibrated radiances obtained from the camera to the results of the RT calculations. Of the several images containing bright clouds, all exhibited a rather sharp cut-off in radiance in the red channel at about 35,000 counts, Figure 11; such a similarity in maximum counts is consistent with expectation based on RT calculations of a maximum in radiance with increasing COD, Figure 1. Comparison of histograms of the several images shows that the image containing pixels with maximum counts was R1043; this is most readily discerned in plots on logarithmic scales, panels *b* and *c*. In order to minimize any effect of any outliers, the maximum value of C to be used in the scaling to normalized radiance, $C_{\max}$, was rather arbitrarily selected as that value of C for which $F_{>C}$ was 2×10^{-5}, out of a total of $3456^2 = 1.19 \times 10^7$; i.e., 238 pixels.

A similar examination was made of the histograms of red channels of several dark images, *i.e.*, containing no cloud or cloud of very low optical depth, Figure 11, panels *d-f*, again with a sharp cut-off in counts at a similar value for the several images. The image containing the lowest counts, R1080, actually appears to have encompassed a region of discernible thin cloud, as discussed above. Comparison of the values of $C_{\max}$ and $C_{\min}$ determined in this way, 35,132 and 1167, with the brightest and darkest regions shown in the false color images, Figure 8*c* and *f*, respectively shows that this procedure accurately determines representative values of the maximum and minimum linearized counts in the images. In particular, the darkest region of image R1080 is the upper right (northeast) corner. Again, as even this region of the image may not be entirely free of thin cloud, the value of $C_{\min}$ obtained from this image, which is the lowest of the series of images shown in Figure 5, may not in fact be representative of a truly cloud-free sky; any cloud contribution to radiance in this would result in the COD determined using this value of $C_{\min}$ being artificially low.

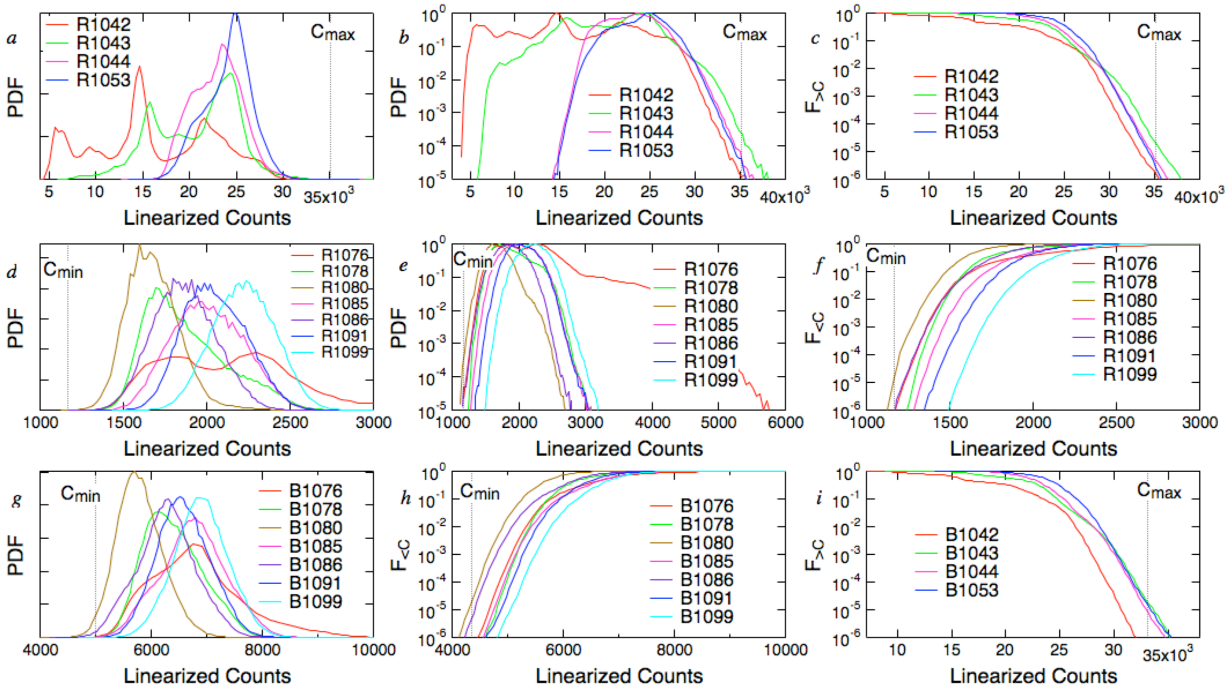

Figure 11. (*a*)-(*c*) Histograms of linearized red-channel counts of several images containing bright clouds during the time period 16:33 to 16:40 UTC. (*a*) PDFs on linear scale, normalized to equal area; (*b*) PDFs, normalized to maximum values, on logarithmic scale; (*c*) complements of the integrals of PDFs, $F_{>C}$, on logarithmic scale. (*d*)-(*f*) Same as *a*-*c*, but for dark sky scenes, and in *f*, displaying $F_{<C}$, the integrals of the PDFs. (*g*)-(*i*) Same as *d, f,* and *c*, respectively, but for blue-channel images containing dark sky scenes. $C_{\max}$ and $C_{\min}$ denote values of C for which $F_{>C}$ and $F_{<C}$, respectively, are equal to 2×10^{-5} used in calculation of cloud optical depth.

The sensitivity of retrieved NZR to choice of $C_{\min}$ and $C_{\max}$ was examined by varying the cut-off values of $F_{>C}$ and $F_{<C}$ from 2×10^{-5} to $(1 - 3) \times 10^{-5}$, showing little sensitivity to the choice of cut-off value. This insensitivity lends confidence in the use of $C_{\min}$ and $C_{\max}$ determined in this way to calculate NZR via Eq. (2) from the counts in the red and blue channels of the camera images and in the use of NZR so determined to infer cloud optical depth and related quantities.

5.4 Normalized zenith radiance

Determination of the scaling parameters permits determination of an effective cloud optical depth and other cloud properties for any of the temporally proximate images shown in Figure 5, for which solar zenith angle can be considered constant. Here two images are examined as examples, Image 1033, a rather dark, thin-cloud image with a substantial region dominated by blue Rayleigh scatter, and Image 1041, dominated by cloud exhibiting a range of brightness shown in RGB in Figure 12; here image contrast is somewhat enhanced to better display cloud features. The red channel signal, dominated by radiance from clouds, Figure 13, shows for each image much spatial structure and a wide dynamic range in counts, factor of 2.5 to 3, the ranges somewhat overlapping. This is seen also in the histograms of counts for the two images, Figure 14. The histograms for the counts in the red and blue channels of each image are rather similar but exhibit some differences, as well as showing the higher minimum count in the blue, a consequence of the Rayleigh contribution to zenith radiance.

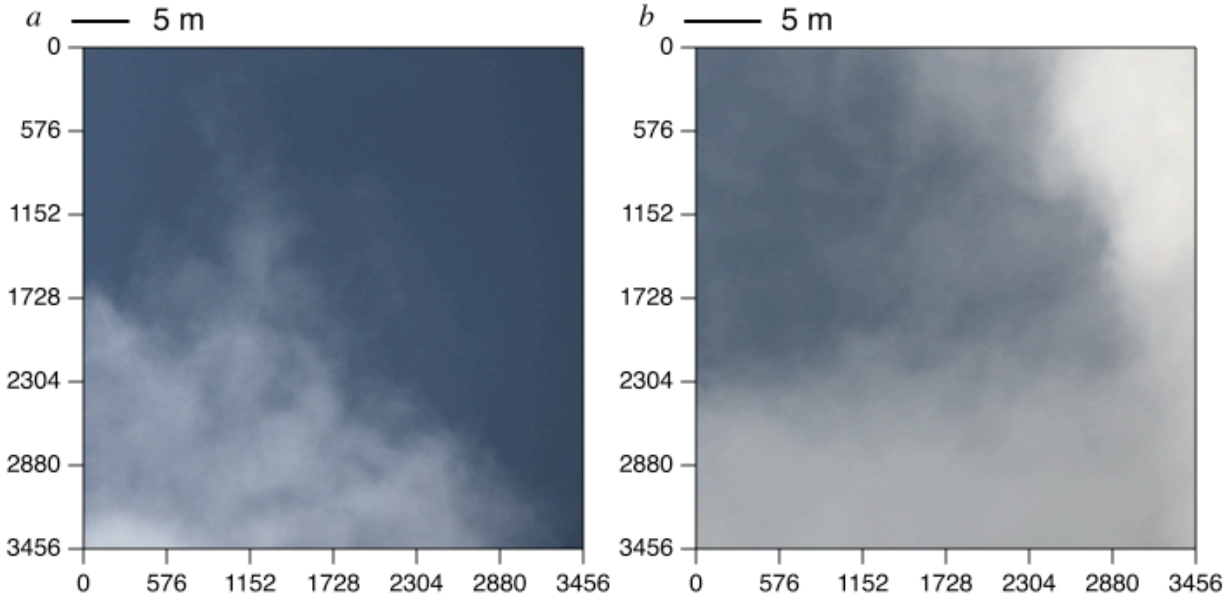

Figure 12. Red-Green-Blue (RGB) images of (*a*) Image 1033 and (*b*) Image 1041. Length scale bars as in Figure 8. For display purpose the image contrast is somewhat enhanced.

Normalized zenith radiance is determined on a pixel-by-pixel basis from the counts in the red and blue channels of the images by first calculating scaled NZR from the counts, Eq. (2). As the transformation from counts to NZR is linear, the false color image of NZR is identical to that for counts except for scale, permitting both quantities to be displayed in a single image but with different color scales, Figure 13. The transformation to NZR is manifested also in the shift and compression of the histograms of the two quantities, Figure 14. The relation between NZR determined from the blue and red channels is shown for each of the two images in Figure 15 on the template obtained from the RT calculations (Figure 3). For the cloudier image, Image 1041, the data conform rather well to expectation. However image 1033, the less cloudy image, yields blue NZR relative to red NZR that is systematically higher than expected from the RT calculations. A possible reason for this is the contribution to NZR from aerosol particles sufficiently small that their scattering coefficient exhibits wavelength dependence, greater in the blue than the red. The histograms for scaled NZR for Image 1041, Figure 14, exhibit good agreement in shape and the expected slightly greater value for blue at low NZR and slightly greater value for red at high NZR. The histograms of NZR for Image 1033 exhibit substantial displacement.

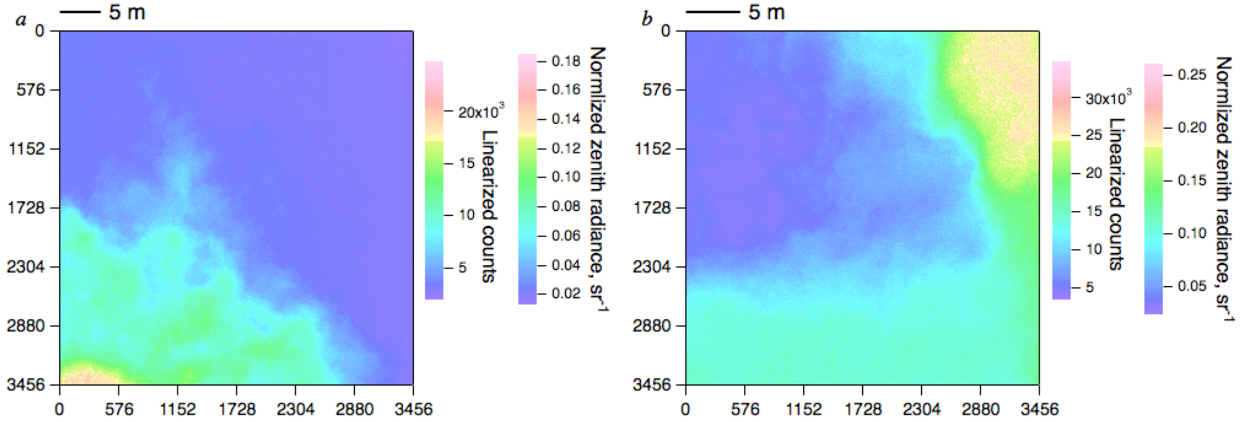

Figure 13. (*a*) False color images of linearized counts in red channel of Image 1033, with normalized zenith radiance shown by second color scale. (*b*) Same for Image 1041. Note different scales for counts and NZRs in the two images, necessary to display wide dynamic range in each image. Length scale bars as in Figure 11.

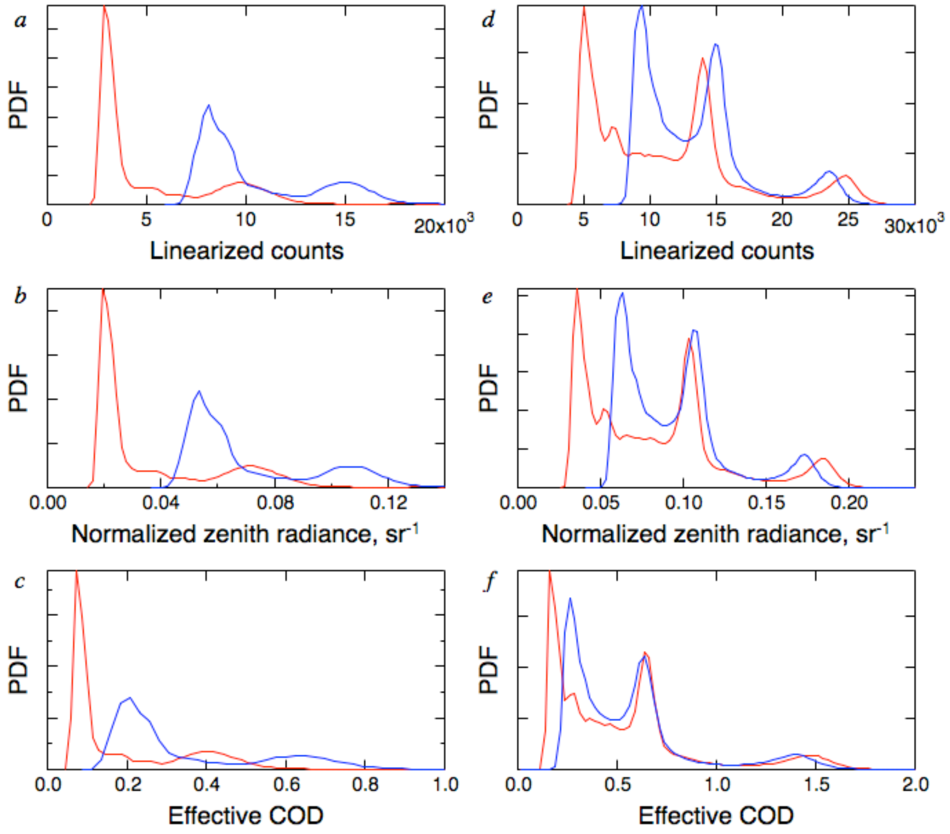

Figure 14. Histograms of linearized counts, normalized zenith radiance, and effective cloud optical depth derived from red and blue channels of Images 1033 and 1041, shown in red and blue, respectively.

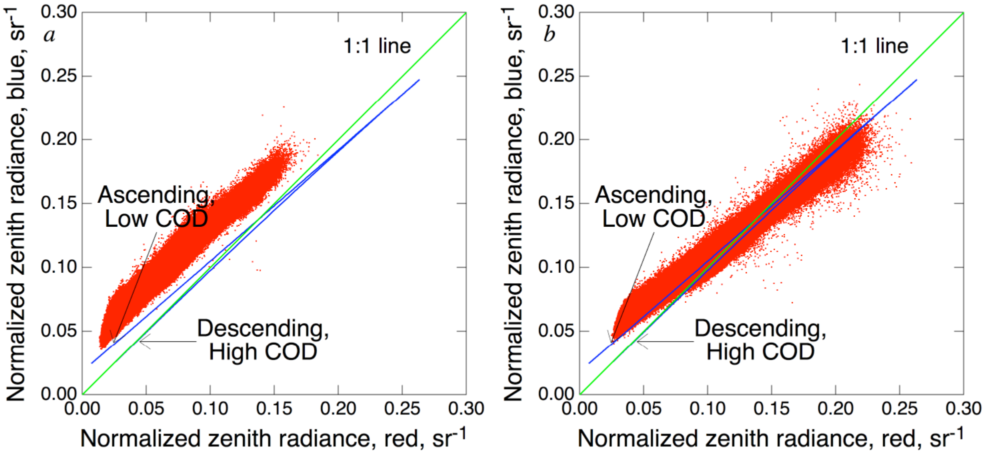

Figure 15. Scatterplots of normalized zenith radiance determined from counts in blue channel versus that from red channel for images 1033 (*left*) and 1041 (*right*). Also shown are relation determined from RT calculations for cos(SZA) = 0.85 (Figure 3), *blue*, and one-to-one line, *green*.

5.5 Effective cloud optical depth

A quantity denoted effective cloud optical depth, ECOD, was determined for each image on a pixel-by-pixel basis by interpolation in the relation between COD and NZR shown in Figure 2. As noted in Section 3, the dependence of COD on NZR given in that figure rests on plane-parallel calculations, and thus because of 3D effects the ECOD so determined for a given pixel may depart from the actual COD, the local vertical integral of the scattering coefficient. ECOD may differ from actual COD also because the calculations leading to Figure 2 were carried out with optical properties which may differ from those characteristic of the actual cloud. We return to this point in the Discussion. Fields of ECOD calculated in this way from both the red and blue NZRs for the two images are shown in Figure 16. Because NZR depends on SZA, the conversion of counts to NZR and in turn to cloud optical depth ECOD is also dependent on SZA; for the time range represented by the images in Figure 5, cos(SZA) was nearly constant, 0.85 ± 0.01, so the conversion calculated for cos(SZA) = 0.85, Figure 2, was employed throughout.

Overall the ECODs are indicative of thin clouds, mainly $\lesssim 1$ for Image 1033; mainly 0.5 – 2 for Image 1041. The spatial structure of ECOD is quite similar to that exhibited by the counts, Figure 13, but with somewhat less dynamic range mainly because conversion of NZR to ECOD subtracts out the contribution of Rayleigh radiance from the images; this is manifested also in comparison of the histograms for ECOD with those for NZR, Figure 14, which shows the much greater overlap of histograms for the red and blue images for ECOD than for NZR. The fact that the retrieved ECOD for Image 1041 was entirely less than 2 suggests little or no region in the cloud of optical depth greater than 4 that would be aliased to lesser value on account of the double valued dependence of COD on NZR, Figure 2; that is, the image consists entirely of what we denote as optically thin cloud.

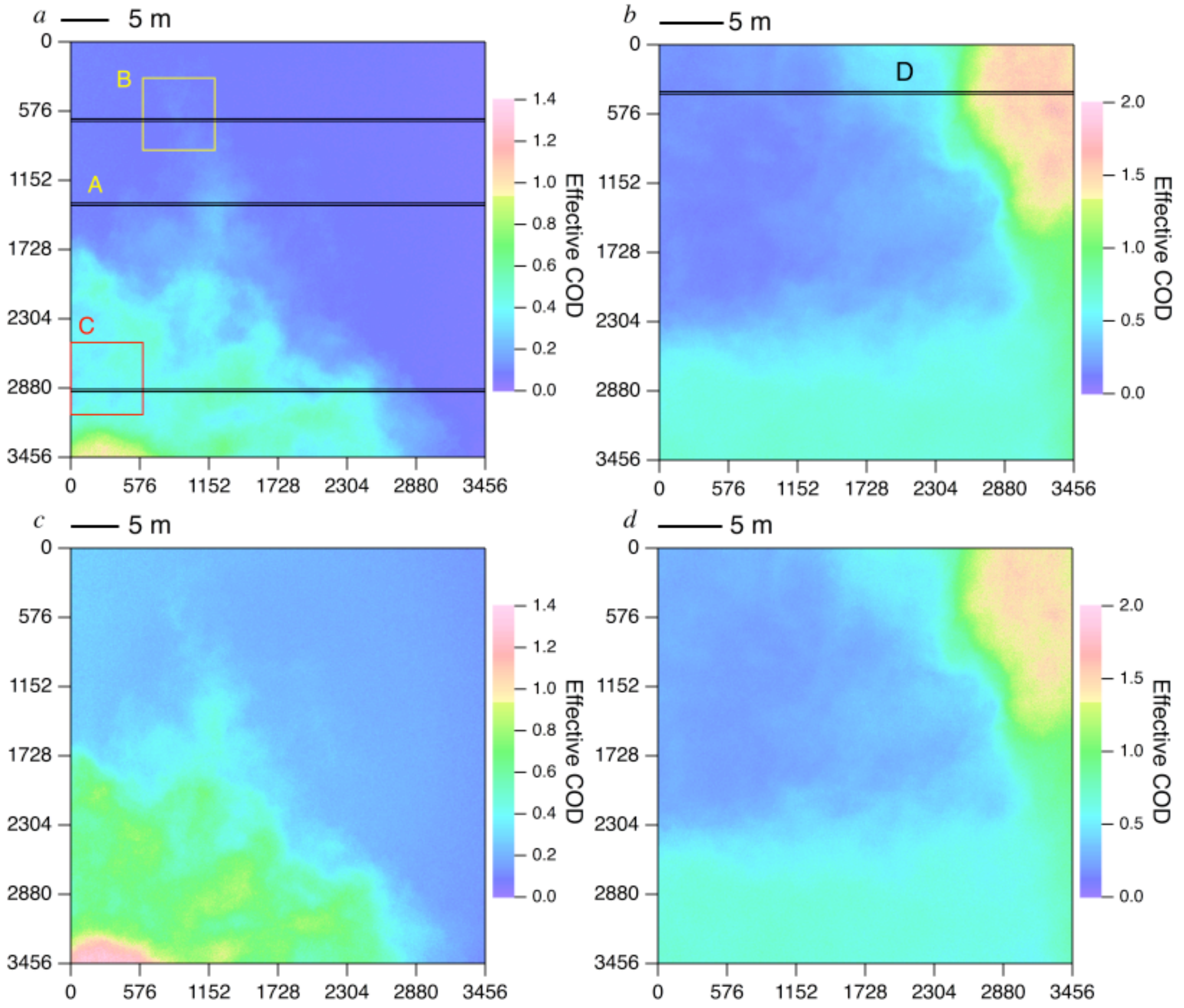

Figure 16. False color images of effective cloud optical depth for Image 1033 (*left*) and Image 1041 (*right*), retrieved from red-channel radiance (*top*), and blue channel radiance (*bottom*); note different color scales for the two Images. Length scale bars as in Figure 8. Boxes (600 pixels on a side) and swaths (21 pixels wide) denote regions examined in higher resolution and as line profiles in Section 5.8.

Although the optical depth fields retrieved from the red and blue channels are similar for each of the images, some differences can be discerned. The similarities and differences in ECOD determined independently from the counts in each of the two channels are seen also in the histograms, Figure 14, and also in scatterplots of ECOD from the blue channel counts versus that from the red channel counts, Figure 17, which show for both images an order-of-magnitude range of ECOD within the 40 m × 40 m image. In principle COD determined from the red and blue channels would be expected to yield the same values as a consequence of the near wavelength independence of the scattering coefficient of clouds. The greater value of ECOD in regions of low ECOD, especially seen in Image 1033, may be due to cloud drop radius in optically thin regions of cloud being less than the 5 µm (asymmetry parameter $g = 0.85$) assumed in the radiation transfer calculations; a smaller drop radius would result in greater optical depth in the blue than in the red. At present these differences are considered one measure of uncertainty in the retrieval of ECOD that is within about 0.1 + 15%.

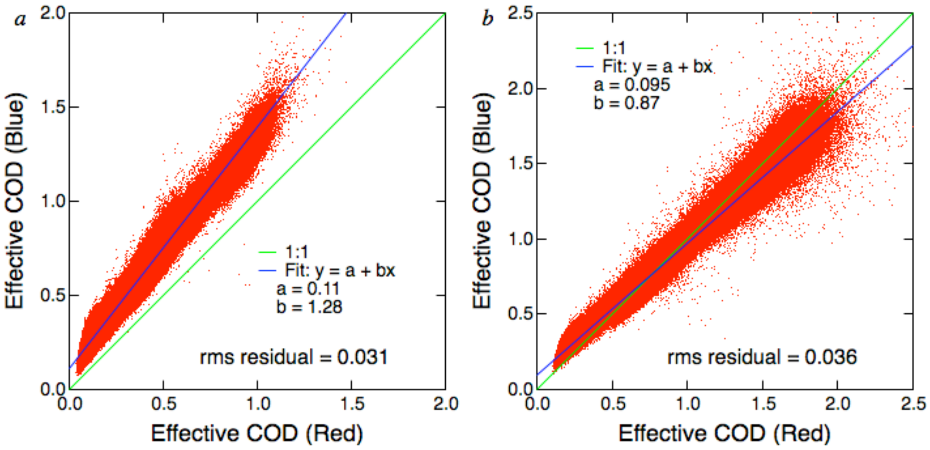

Figure 17. Scatterplots of effective cloud optical depth determined for individual pixels from counts in blue channel of image versus that determined in red channel for Images 1033 (*left*) and 1041 (*right*). Also shown are linear regression lines and associated fitting coefficients and one-to-one line; rms residual is root mean square of residual about regression fit.

A possible source of systematic error in determination of ECOD arises from sensor noise in the camera resulting in values of C_{max} that are erroneously high, or alternatively values of C_{min} that are erroneously low, systematically affecting the conversion of linearized counts to normalized zenith radiance by Eq. (2) and in turn systematically affecting the retrieval of ECOD from NZR. The magnitude of the resulting error would depend on the magnitude of sensor noise. Sensor noise examined by several approaches (SI, Section 2.4) is approximately 2.5%, one-sigma. As shown also in SI (Section 2.5), a value of C_{maz} that is erroneously high by 2.5% would yield a value of ECOD that is erroneously low by 2 to 12%, increasing with increasing ECOD up to ECOD = 3; the effect of error in C_{min} was minimal. Sensor noise would also contribute to noise in retrieved values of ECOD in individual pixels by similar percentages.

5.8 Spatial variation of cloud properties

The large number of pixels in a given image permits examination of spatial variation of radiance and derived products at a range of length scales. Figure 18 shows in panel *a* a series of line profiles across linearized counts or ECOD at specific values of North-South dimension, indicated by horizontal lines in Figure 16*a* (shown also in enhanced-contrast RGB images in Figure 12), as derived from Image 1033 and Image 1041. Panel *a* shows line profiles of linearized counts on three adjacent single-pixel swaths; also shown is an estimate of the noise associated with counts in a single pixel (estimated standard deviation of counts in a single pixel 2.5% of the count, as determined in SI Section S2.4) expressed as ± three times the estimated standard deviation. By that measure the cloud feature manifested at pixels 900-1500 stands out unmistakably from the background as an enhancement of radiance, attributable to enhanced cloud scattering, of East-West width about 8 m, with an increase in linearized counts of about 4000 counts or 40 times the estimated standard deviation of the measurement, about 100 counts. Similarly there is an increase in scattering of about 1100 linearized counts between pixels 320-443 corresponding to an East-West distance of about 1.5 m. Such systematic changes in radiances over such distances are commonly observed in the images. Corresponding values of ECOD shown in panel *b* are

0.11 at the east (left) base of the peak at 1200 pixels, and 0. 25 at the peak, a change in ECOD of 0.14 over a distance of about 4 m. The increase in ECOD at pixels 320-443 pixels corresponds to an increase in ECOD over this distance, 1.5 m, from 0.084 to 0.135 or 0.05. Panel *c* shows that the sharp increase in ECOD from 0.5 to 1.3 along the line profile D in Figure 16*b* occurs over a distance of 2.5 m.

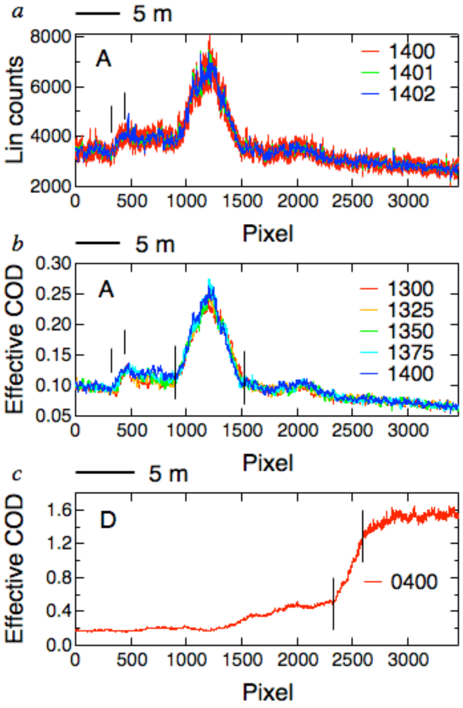

Figure 18. Line profiles, indicated by row pixel number (North-South direction), across images for linearized counts and effective COD obtained from red-channel radiance. (*a*) Linearized counts for Image 1033 for three adjacent single-pixel swaths shown at line A in Figure 15. For profile 1400 vertical uncertainty bars denote ± 3 times estimated standard deviation. (*b*) Line profile of effective COD for Image 1033 derived from red channel linear counts; swath width 21 pixels. (*c*) As for *b* but for single profile in Image 1041 corresponding to Line D in Figure 15*b*. Vertical lines denote features discussed in text.

Variation in ECOD of such magnitude and on such scales is commonly exhibited in these images, further examples of which are shown in Figure 19, which zooms in on ECOD in two subregions of the image presented in Figure 16*a*. Here, in addition to the approximately 6-fold zoom from the scale of that image, the range of the false color scales is substantially decreased to display the spatial variation in these relatively homogeneous regions of the parent image. Attention is called also to the barely discernible cloud in the corresponding region of the enhanced-contrast version of the RGB image, Figure 12*a*. The lower panels of Figure 19 show series of line profiles of ECOD across the images exhibiting coherent variation among the several proximate traces. These examples point out regions of such coherent variation by amounts ranging from a few hundredths to a tenth of an optical depth unit over a distance range as low as about 1 meter. This coherent variation lends confidence to the ascription of the variation to variation in cloud properties affecting zenith radiance.

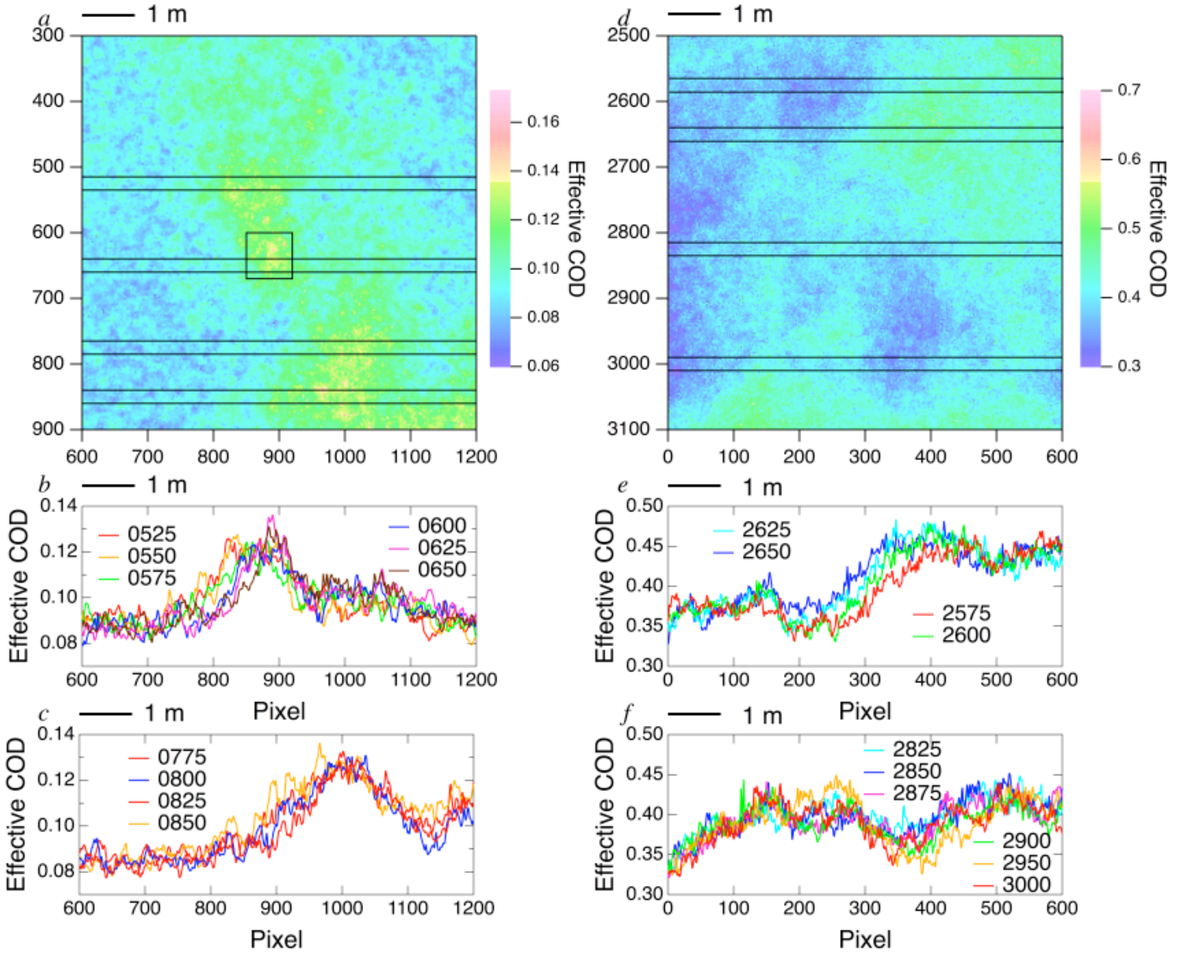

Figure 19. Zoomed images and line profiles of effective COD. (*a*) and (*d*) ECOD obtained from red channel in subregions B and C, respectively, of Image 1033 shown in Figure 16*a*. Note differences in color scales and differences also from that in Figure 16*a*. (*b*)-(*c*) and (*e*)-(*f*) Line profiles of ECOD having swath width 21 pixels (25 cm), with central pixel value denoted in legend. Horizontal stripes in *a* and *d* denote locations of northermost and southermost swaths of the two sets of line profiles shown in *b*-*c* and *e*-*f*, respectively. Length scale bars are evaluated for cloud height taken as 2 km.

A final example zooms further in on Image 1033, specifically on the subregion shown by the square in Figure 19*a*, a further factor of about 8, shown in Figure 20, which shows a region of elevated radiance and ECOD of dimension roughly 10 × 30 cm. Again attribution of the variation in red radiance and effective COD is informed by the estimation of sensor noise in Section S2.4. Panel *b* shows five single-pixel line profiles of red-channel linearized counts together with the estimated uncertainty again shown as ± 3 times the standard deviation of the noise associated with the radiance in a single pixel, about 100 counts. Also shown is the average of the five line profiles. The increase in counts between pixels 878 and 890, corresponding to a distance of 14 cm for cloud height 2 km, 740 counts, is about 7 standard deviations of the noise associated counts in a single pixel. This comparison together with the systematic enhancement of zenith radiance throughout the central portion of the subregion is taken as indicative of enhanced zenith radiance in this region of the cloud. Panels *c* and *d*, which present the conversion of the data to

ECOD and which exhibit the same spatial pattern, permit determination of the variation in ECOD over the subregion. Specifically the increase in ECOD between pixels 878 and 890, 0.034 of an optical depth unit, demonstrates the ability of the measurement to determine such small changes in ECOD over a distance of 14 cm. As may be seen in Figure 19*a* there are several additional regions that exhibit such enhanced ECOD relative to the surrounding areas within the cloud. Inspection of these and other images shows this phenomenon to be a frequent occurrence.

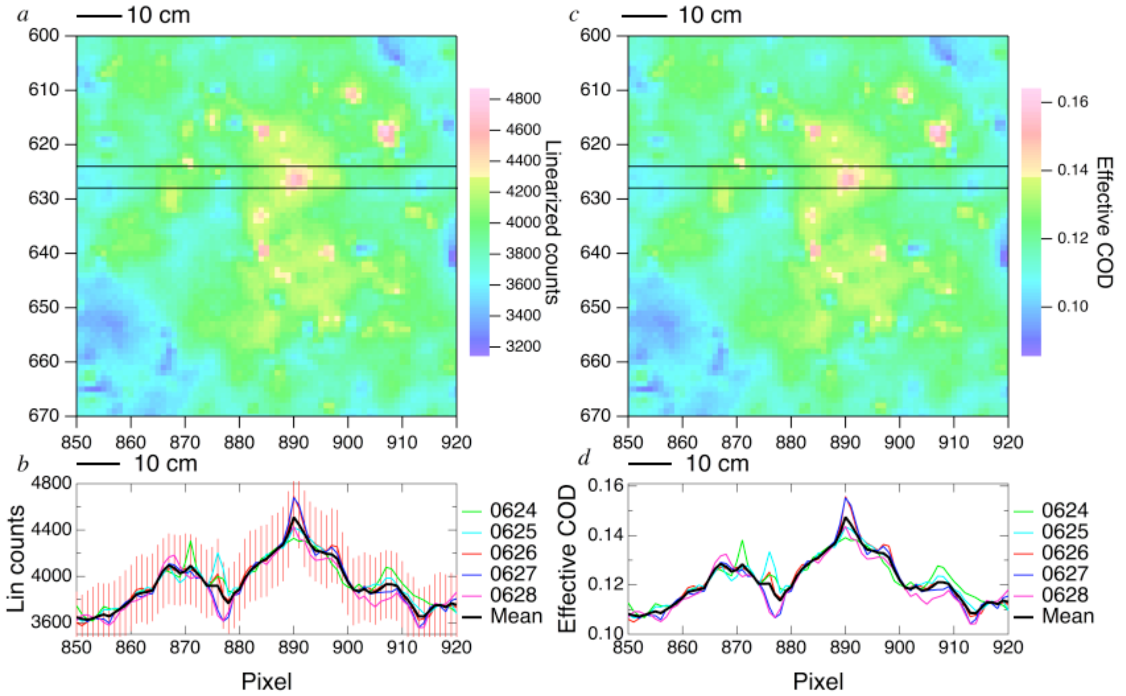

Figure 20. Linearized counts and effective optical depth at higher magnification. False color image of (*a*) linearized counts and (*c*) effective COD for the region of Image 1033 denoted by the square box in Figure 19. Five single-pixel line profiles of linearized counts (*b*) and ECOD (*d*) at pixel values bounded by horizontal lines in *a* and *c*, respectively, and indicated in legend. Also shown in panels *b* and *d* are the means of the five line profiles, and in *b*, uncertainty bars denoting ± 3 times the standard deviation of noise associated with counts in a single pixel. Individual pixels discernible in the images correspond to linear dimension 12 mm at cloud height 2 km; length scale bars are evaluated for cloud height taken as 2 km.

6 Discussion

We present and analyze photographic images of sky containing boundary-layer cumulus humilis clouds obtained with vertically pointing high-magnification, narrow field-of-view digital cameras. With such narrow field of view the amount of cloud in the images can change rapidly on a time scales of seconds to minutes, a consequence of clouds being advected into and out of the camera field of view. In the examples presented here, for a seven-minute time period on a single day at Oklahoma, cloud dimensions were tens to hundreds of meters. As well the photographs exhibit considerable structure in individual images of dimension approximately 30 meters on a side at cloud altitude.

The analysis presented here emphasizes optically thin clouds having COD $\lesssim$ 2. A 1-D radiation transfer model was used to determine normalized zenith radiance (NZR, zenith radiance per downwelling irradiance) pointwise in the images and in turn to retrieve what we have denoted an effective cloud optical depth, ECOD. The resulting fields, displayed as false color images, exhibit rich spatial structure that corresponds to the spatial structure in the original cloud photographs. The images of NZR and ECOD consist of, for each of the red and blue channels of the camera, some 3 million independent determinations at spatial resolution (~3 cm for cloud at 1.5 km) that exceeds that from common current imaging approaches by 3 to 5 orders of magnitude and surface-based non-imaging approaches such as sky photometry by 3 orders of magnitude. Examination of clouds at this resolution provides unprecedented detail of cloud properties both in relatively homogeneous regions of cloud and in regions of strong gradient in radiance showing rich spatial structure in NZR on scales at least down to about 10 cm. As discussed below, the observed variation in NZR is ascribed to corresponding variation in COD.

As the 1-D radiation transfer model employed in the retrieval of effective COD from NZR assumes horizontal homogeneity, the question arises to what extent the observed variation in NZR can be attributed to variation in COD and to what extent the retrieved effective COD approximates the actual local COD. (Similar issues arise, albeit on much different geometrical scale, in retrieval of COD from upwelling radiances measured by satellite-borne instruments, [e.g., Marshak et al, 1998; Iwabuchi and Hayasaka, 2002; Davis and Marshak, 2010]). There are three classes of reasons why the effective COD might differ from the true COD: 1) remote influences such as shadowing or sidewall reflectance by another cloud; 2) local influences due to horizontal radiation transport occasioned by inhomogeneities within the cloud, and 3) smoothing of the radiation field due to multiple scattering. For the cloud images examined here we have selected situations where remote influences appear minimal. We note as well that the short-range variation in NZR seen here is almost certainly unlikely to result from variations in downwelling radiation at the top of the cloud due to remote influences and is therefore attributed to local variation in COD. The question then arises over the equivalence between COD determined with the 1-D RT model, that is, treating each pixel as uninfluenced by horizontal RT into or out of the column (independent pixel approximation), and the actual COD, the vertical integral of scattering coefficient in the cloud. Here the argument is made that in the limit of an optically thin cloud, for which scattering is dominated by single scattering events during photon transport in the cloud, these two quantities become equivalent. Qualitatively this argument is made by reference to the several examples of photon path shown in Figure 21. Here path A depicts a single scattering event, which, for an optically thin cloud, is the dominant contribution to NZR, namely scattering in the principal plane by angle θ equal to solar zenith angle θ_0. For size parameter $x = 2\pi r / \lambda >> 1$, where r is the cloud drop radius and λ is the wavelength, characteristic of scattering of visible light by cloud drops, scattering is predominantly in the forward direction, so for small θ_0, scattering is predominantly downward. Positive (path B) or negative (Path C) contributions to NZR other than from single scattering events, which lead to horizontal radiative transfer that would couple two or more pixels, must involve multiple scattering events. Hence for optically thin clouds for which contributions from multiple scattering would be minimal, the effective COD obtained from the 1-D RT model can be confidently equated to the actual COD. A criterion for this situation is the criterion for cloud radiative effects to be linearly related to COD advanced by Gabriel and Evans [1996], namely that the scaled COD $(1-g)\tau << 1$, where g is the asymmetry parameter and τ is COD. For g =

0.85 characteristic of r = 5 µm and COD = 2 the scaled COD is 0.3; the approximate linear relation between COD and NZR for COD $\lesssim$ 2 (Figure 3) suggests that COD = 2 might be taken as the maximum value of COD for which the COD inferred from the 1-D RT model is an accurate measure of actual COD. Examination of images of retrieved COD for images 1033 and 1041 shown in Figure 16 shows this criterion to be satisfied for those retrievals.

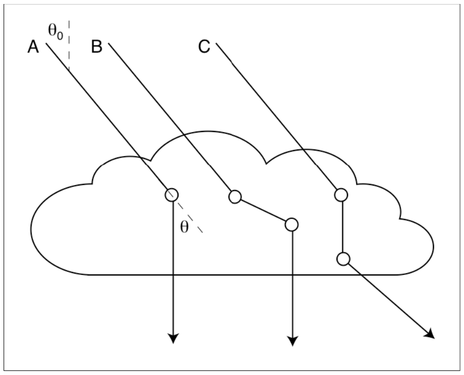

Figure 21. Single and multiple scattering in an optically thin nonuniform cloud. *A*, single scattering into zenith radiance; scattering angle θ is equal to solar zenith angle θ_0. B, multiple scattering into zenith radiance. *C*, multiple scattering out of zenith radiance.

To the extent that the effective COD determined here represents the actual local optical depth of the cloud then the 1-D RT calculations used to retrieve COD from radiance can be used to calculate other radiative effects of clouds at the same spatial resolution as that of COD, importantly the cloud albedo, the enhancement of scene albedo due to the presence of cloud, and the color ratio between red and blue NZR, a measure of cloudiness.

The emphasis here has been on optically thin clouds, COD $\lesssim$ 2, a category of clouds that is difficult to characterize [Turner et al., 2007; Zuidema et al., 2012] and under-characterized but radiatively quite important. By many measures these are thin clouds indeed. To illustrate this point Table 1 summarizes the optical and physical properties of a cloud of COD = 1 and physical thickness 50 m (Figure 7). Attention is called to the scattering coefficient 0.02 m^{-1}, or, equivalently the photon mean free path, 50 m. Such a mean free path is comparable to the cloud physical thickness. It also far exceeds the horizontal resolution in the photographs, nominally 9 mm for cloud at 1.5 km above the surface. The corresponding liquid water path (LWP), calculated for assumed drop radius 5 µm, is 3 µm or 3 g m^{-2}, 1.5 orders of magnitude less than the threshold commonly taken for thin clouds, 100 g m^{-2} [Turner et al., 2007]. Despite such low LWP the drop density is such that for pixel size at cloud height, $A \approx 1$ cm^2, the areal density N of cloud drops is sufficiently great that pixel to pixel variation in COD due to shot noise in droplet number per pixel, fractional noise $(NA)^{-1/2} \approx 1 \times 10^{-3}$, is much less than the observed variation (and also much less than the observed fractional uncertainty in counts due to sensor noise, ~0.025), supporting attribution of observed variation in NZR to environmentally induced variation in cloud properties.

The optically thin clouds such as those characterized here are radiatively quite important, with typical local and instantaneous TOA shortwave radiative effect for COD = 1, about 80 W m^{-2}. Such a substantial radiative effect underscores the climatological importance of such thin clouds and the necessity of accurately representing them and their radiative effects in climate models. The absence or under-representation of such thin clouds in a model would require enhancing the albedo of the clouds actually represented in the model to achieve the accurate albedo in large-scale averages, a phenomenon that is exhibited by many current climate models based on comparison with cloud amount determined by satellite-based remote sensing [Kay et al., 2012; Nam et al., 2012; Wang and Su, 2013]. The presence of thin radiatively important clouds such as those characterized here but missed in satellite measurements would exacerbate this "too-few, too-bright" problem.

Quantity	Symbol or formula	Value	Unit
Drop radius	r	5×10^{-6}	m
Optical depth	τ	1	
Cloud thickness	Z	50	m
Scattering coefficient	$\alpha = \tau / Z$	0.02	m^{-1}
Photon mean free path	$\Lambda = \alpha^{-1} = Z / \tau$	50	m
Scattering cross section	$\sigma = 2\pi r^2$	1.6×10^{-10}	m^2
Drop areal concentration	$N = \tau / \sigma$	6×10^9	m^{-2}
Drop volume concentration	$n = N / Z$	1.3×10^8	m^{-3}
Liquid water path	$L = \frac{2}{3} r\tau$	3×10^{-6}	$m^3\ m^{-2} = m$
Liquid water volume fraction	$W = L / Z$	6×10^{-8}	[-]
Side of pixel	Δx	0.01	m
Area of pixel	$\Delta A = (\Delta x)^2$	1×10^{-4}	m^2
Number of drops in pixel	$N \Delta A$	6×10^5	[-]

Table 1. Typical cloud physical and optical properties. Quantities in red are based on assumption (drop radius) or observations; quantities in black are derived according to indicated formulas. For this calculation cloud is assumed monodisperse with single drop radius r; cloud drop concentration n is assumed constant with height within cloud.

A key point to be emphasized here regards the use of an imager in the attribution of observed variation in radiance to variation in cloud contribution to this radiance and ultimately to variation in COD. Specifically in the example examined in Figure 20 and the attendant discussion use of an imager to provide the spatial pattern of variation (as opposed to a time series from a point measurement) was central to confident attribution of the variation in zenith radiance to variation in cloud amount.

A persistent issue associated with retrievals of COD from radiance measurements is the so-called ambiguity problem [Chiu et al., 2006; Schäfer et al., 2013; LeBlanc et al., 2015, Niple et al., 2016; Mejia et al., 2016] arising from the double-valued dependence of COD on NZR, Figure 3. For the present we rely on visual inspection of NZR fields under the assumption of spatial continuity of COD and NZR; that is NZR is expected to reach a maximum value consistent with that exhibited in the RT models at a COD of approximately 4, depending on solar zenith angle. Examining the spatial variation of NZR permits identification of maxima in radiance such that decrease in NZR on the other side of the maximum is indicative of thicker cloud in that region. This visual inspection approach contrasts with other approaches, such as that of using the color ratio (Red/Blue ratio) [Koehler, 1991; Mejia et al., 2016; Niple et al., 2016] or the isomorphic Red/(Red + Blue) ratio that is commonly employed in cloud screening [e.g., Long et al., 2006]; the ratio method is based on the fact that at low COD the ratio of blue to red NZR is high, whereas for thick cloud this ratio approaches unity. Examination of color ratio as a measure of cloud contribution to NZR and albedo in high-resolution images will be presented elsewhere. For the moment we rely on visual inspection of images to limit retrievals to regions of thin cloud.

To what extent should the short-scale variation in optical depth of clouds reported here be considered a surprise? Substantial variation in cloud radiance is exhibited in images of COD obtained from high resolution (Landsat) satellite images [Barker et al., 1996], down to the limit of the pixel size of the images, 30 m, some three orders of magnitude greater than that obtained here. Schäfer et al. [2013] presented images of thin cirrus clouds from ground-based imaging with resolution about 15 m exhibiting occasional sharp features with difference in COD between adjacent pixels by as much as about 0.5. Mejia et al. [2016] presented images of radiance from which they retrieved images of COD using a RT model, which likewise exhibited strong variation in COD on scales of 15 m (for assumed cloud base height of 1 km). Fine structure in cloud radiance, down to the limit of the resolution, estimated as about 1 m, was seen also in the film-photographic images of Sachs and Lovejoy [2002]. For that matter, frequently it is possible to visually discern filamentous structure in clouds across the diameter of a full moon (9 mrad, compared to the square images examined here, 22 mrad); such variation can be seen even at rather small zenith angle, so that one is seeing horizontal variation of perhaps 1 m at 1 km.

Certainly also there is an abundance of in-situ measurements, going back for quite some time, showing variation in cloud properties, especially at cloud edges, and showing that these changes can be quite sharp. During flights in broken stratiform clouds ten Brink et al. [1987] reported fluctuations and spikes in liquid water content and turbulent energy dissipation rate on scale of a few meters. Fluctuations on a similar spatial scale were reported also by Gerber et al. (1994). Siebert et al. [2006] presented in-situ measurements showing a change in turbulent energy dissipation rate by 4 orders of magnitude within 50 m in the vicinity of cloud edges. More recently Kumala et al. [2013] report variation in liquid water content on scale of 5 m and small scale filaments of temperature fluctuations on scale of 10 cm. Beals et al. [2015], on the basis of in-situ holographic measurements, report turbulence structure in clouds down to scales of 1 cm. These measurements suggest that the variation of cloud properties down to 10 cm or so inferred from the observations reported here should not be viewed as a surprise.

Perhaps more surprising than the finding of fine spatial structure in cloud images documented here is the ability to quantify variation in cloud radiance and inferred optical depth down to centimeter scales by remote sensing from the surface in the form of "images" consisting of some 3 million independent determinations in each of the red and blue channels. At larger scales, one to several meters up to the entire domain of the NFOV camera, 30 m, variation in COD can be attributed to transitions between cloud and clear sky associated with cloud edges or to gradients across an image. Images such as these present an unparalleled opportunity to examine such transitions and gradients, to examine their implications, and relate them to controlling processes. The short-range variation in CRE that arises from short-range variation in COD found here is substantial. For example, the variation of COD from 0.2 to 2.6 over a distance of 15 m shown in Image 1041 (Figure 18) corresponds to a variation in instantaneous TOA CRE over this distance of ~150 W m^{-2}. This sort of imaging approach and the quantitative determination of optical depth may prove useful also in examining the transition between cloud and cloud-free sky and the role of aerosol in blurring that transition into a continuum [Charlson et al., 2007; Koren et al., 2007]. We note as well the possibility of quantitatively examining cloud temporal evolution as exhibited in the successive images presented in Figure 9.

At fine scales, less than 1 m, perhaps a surprise is that the sort of spatial variation exhibited in Figure 20 is commonly exhibited in the clouds examined and thus may be the rule rather than the exception, although it would be premature to make any such claims beyond the images examined thus far. Surprising as well is the finding of what appears to be organized structure on such scales. To what can this shorter-scale organized structure of cloud radiance and inferred optical depth be attributed? We hypothesize that at the finest scales examined these quantities are manifestations of the local turbulent motions governing cloud droplet growth or evaporation that in turn influences the light scattering that is measured as zenith radiance. Given the importance of such turbulent motions in influencing the evolution of the cloud drop spectrum, the development of precipitation and ultimately the contribution of clouds to Earth's radiation budget [*e.g.*, Devenish et al., 2012; Grabowski and Wang, 2013] it would seem that measurements such as these might usefully contribute to the understanding of such turbulent motions and to their representation in cloud models. So far, with the limitation of the frequency with which we have been able to obtain successive images with the cameras employed, it has not been possible to follow these turbulent motions temporally, but that would seem a natural future direction. Such measurements might then help inform or constrain approaches to represent clouds in high resolution models such as large eddy simulations and direct numerical simulations.

A concern at the present stage of analysis is identifying minimum and maximum values of counts corresponding to cloud-free and maximum brightness clouds necessary to scale the counts in the images to the RT calculations. The use of images lends considerable confidence to the procedure, as opposed to simply examining the time series from an uncalibrated radiometer, in view of the many pixels in a given image and the spatial context provided by the images. Additional confidence would be gained if the values of $C_{\min}$ and $C_{\max}$ can be determined from multiple images, perhaps extending over multiple days, permitting a better definition of uncertainty in these quantities and the resultant implications on determination of COD and other quantities. We anticipate that it will be straightforward to extend the analysis to images with, respectively, lower and higher counts by examining the range of solar zenith angles throughout a single day's deployment, taking into account the dependence of $C_{\max}$ and $C_{\min}$ on SZA.

An additional source of possible systematic error in the present study arises out of the RT calculations that form the basis of scaling the camera to radiance and determination of ECOD. The calculations were made for a wavelength-independent COD and a single value of asymmetry parameter, 0.85 characteristic of drop radius 5 μm. For radii characteristic of cloud drops and larger aerosol particles (effective radius > 1 μm) the wavelength dependence of scattering coefficient is slight [Kokhanovsky, 2004; Schuster et al., 2006], and over this size range the asymmetry parameter decreases to 0.82. Consequently the influence of drop radius on the retrieval of COD is considered slight. However if light scattering by aerosol particles having radius less than 0.8 μm contributes substantially to the signal, the greater scattering coefficient would result in greater radiance in the blue channel than in the red and result in enhanced retrieved ECOD from the blue channel than the red. This may account for the greater effective ECOD retrieved at low COD in the blue than the red (Figure 17*a*) Likewise, the variation in Rayleigh radiance with wavelength over the range of sensitivity of the camera channels might play a role; here single wavelengths corresponding to the peak in the spectral sensitivity of the red and blue channels have been used, rather than a weighted average over the spectral sensitivity of the camera. Alternatively and additionally it may be possible to compare normalized zenith radiance determined via the RT calculations to measurements of this quantity by other approaches under conditions sufficiently homogeneous that mismatch in FOV or averaging time would be unimportant.

The short-range spatial and temporal variation of cloud contribution to zenith radiance presented here is qualitatively similar to variation observed on multiple days in the Oklahoma project and in pilot studies at Brookhaven National Laboratory (Upton, Long Island NY, June-August, 2014) and City University of New York (New York City, May, 2015). All of these studies reveal frequent occurrence of clouds exhibiting similar short-range structure and frequently consisting of an intimate mixture of blue sky with cloud and/or transmittance of blue through thin clouds. Based on these observations we have reason to believe that the high temporal and spatial variation reported here may be quite general.

From a measurement perspective perhaps yet another surprise is the ability to produce such detailed images of cloud optical depth with a low-cost commercially available camera. In this context we note that such cameras have previously been employed with careful calibration in other applications such as monitoring crop variables [Lebourgeois et al., 2008]. It thus seems that relatively inexpensive commercially available digital cameras may have much to offer in environmental studies. The high-resolution capability of such cameras seems especially promising.

The high-resolution imaging approach presented here might be contrasted with other approaches to characterizing cloud distributions. Certainly the great strength of the high resolution photography is the rich amount of spatial information that is obtained. A fundamental limitation of the approach is the inherent two dimensionality of the measurement, with no characterization of the vertical dimension. Another limitation for quantitative interpretation is that for clouds of optical depth greater than about 3, the inversion of radiance to optical depth becomes much more problematic than for optically thin clouds [Mejia et al., 2016]. Similar considerations obtain for situations with clouds at multiple levels. A further key limitation to the method is that it is restricted to daytime (sunlit) conditions, as the measurement relies on scattering of solar radiation. Also, the measurements are hyperlocal; at the maximum focal length of the camera employed here the field of view of approximately 20 mrad, corresponds, for a cloud at 1 km altitude, to 20 m. Satellite imagery likewise presents only a two dimensional image, although much information is gained from concurrent measurements in the shortwave infrared that permits inference of effective radius and in thermal infrared that permit assignment of altitude. A limitation of the satellite approach is that of spatial resolution that clearly misses much subpixel variation. Also for satellites in low-earth orbit there is no possibility of continuous measurements to follow temporal development of clouds, although such continuous measurements are readily available from geostationary satellites and are commonly used to examine transport and development of weather systems. Active sensing by lidar or radar offer valuable alternative views of clouds, especially in the vertical dimension, that is not available by the photographic approach. Still, it would seem that photographic measurements of the sort described here afford the unique prospect of providing valuable information about the spatial variation of cloud properties on unprecedented scales that would seem capable of informing understanding of the processes responsible for that variation and more generally for quantifying the radiative effects of clouds and representing these effects in models.

The imaging approach described here might also be contrasted with other studies examining clouds by surface-based photographic imaging. Several studies have used stereo imaging along more or less horizontal path to examine development of cumulus or orographic clouds, relying especially on high temporal and spatial resolution to characterize vertical structure and development [Zehnder et al., 2007; Hu et al., 2009; Öktem et al., 2014; Romps and Öktem, 2015; Ewald et al., 2016]. However none of these studies exploits the extraordinary spatial resolution of the present study, although there does not seem any hindrance to that, nor has there been an effort to quantitatively retrieve cloud optical thickness (path integral of extinction coefficient). Attention is called also to work directed at measuring cloud radiance over the hemispheric dome of the sky in red and blue and inverting to yield a map of optical depth by interpolation of radiative transfer calculations for homogeneous sky as a function of COD, SZA, and viewing geometry [Mejia et al., 2015], applied mainly to clouds of optical depth much greater than those examined here. Koren et al. [2007] present an oblique image of scattering by cloud and proximate hydrated aerosol; although the radiative transfer calculations needed to quantitatively interpret such an image would be challenging, high resolution imaging of such situations would seem to be quite informative of the transition between aerosol and cloud.

Finally the imaging approach presented here should be contrasted with non-imaging approaches. Marshak et al. [2009] and Chiu et al. [2009, 2010] use spectrally resolved measurements obtained with a calibrated zenith spectral radiometer with temporal resolution (1 s) comparable to that of the camera as employed here, but with limited spatial resolution (1.4° = 24 mrad). These investigators find that zenith radiance in the vicinity of clouds can be expressed as a linear combination of contributions from cloud and cloud-free sky with a single wavelength-independent weighting factor, a finding that is supported by radiation transfer calculations with a model similar to that used in the calculations presented in Section 3. Scatterplot graphs (not shown) of the weighting coefficients determined on a pixel-by pixel basis from the red and blue radiances for Images 1033 and 1041 by the procedure of Marshak et al. [2009] are essentially identical to scatterplots for the radiances themselves, Figure 18, a consequence of the linear transformation between NZR and the weighting coefficient introduced by Marshak et al. [2009]. LeBlanc et al [2015] report the use of a zenith pointing spectrometer with spectral range 300 – 1600 nm and field of view 50 mrad together with the 1-D DISORT RT code to retrieve multiple cloud properties including optical depth, effective radius and phase (liquid or solid or mixed). Measurements with the camera presented here might be considered complementary to those with zenith radiance spectrometers, providing 7 orders of magnitude more independent measurements with roughly 3 orders of magnitude greater spatial resolution at the expense of spectral resolution. However the finding in the studies of Marshak et al. [2009] and Chiu et al. [2009, 2010] that the weighting factors are independent of wavelength, and indeed the spectrally flat scattering coefficient of cloud droplets throughout much of the visible spectrum, support the utility of the two-wavelength approach taken here for determining cloud contribution to the measured radiance on a pixel-by-pixel basis with little loss of information that might be gained from spectrally resolved measurements.

7 Concluding remarks

This paper has presented an initial account of measurements using a commercially available digital camera of downwelling shortwave radiance by resolution photography from the surface looking vertically upward. Such measurements provide two-dimensional images of radiance in three color channels with high spatial resolution (6 μrad nominal, corresponding for clouds at height of 2 km, to 12 mm), high signal-to-noise ratio (~40) for a single-pixel measurement, and high time resolution (0.5 ms exposure time). Images of clouds obtained in this way are found to exhibit high spatial variation that is attributed to variation in cloud optical depth within the spatial domain of the images (as small as 20 × 20 mrad, corresponding for clouds at height of 1.5 km, to 30 × 30 m) and high temporal variation due mainly to advection of clouds across the field of view of the cameras.

Quantitative analysis of the images has been restricted thus far to optically thin clouds, optical depth $\lesssim 2$. A method is presented to infer cloud optical depth COD on a pixel-by-pixel basis from the images by scaling the counts in the camera images to RT calculations. A concern over this scaling is that it requires scenes (subsets of images) at minimum brightness in the absence of cloud and at maximum cloud brightness, before the cloud becomes so optically thick that further increase in COD decreases downward scattered radiation; failure to meet these requirements would lead to error in retrieved COD. Based on comparisons of scaled normalized radiance and COD retrieved independently from red and blue channels retrieved COD is considered uncertain to 10% for COD in the range 0.5 to 2, although other sources of error cannot be excluded.

The spatial resolution achieved with the surface-based camera images opens up a vast new domain for examination of spatial structure of clouds. We find that there is commonly considerable variation in radiance at all scales examined, with coherent spatial structures at scales as low as 10 cm. We attribute this variation to variation in cloud optical depth on such scales, that we hypothesize to be due to local turbulence. Should this turn out to be the case, then it suggests that high resolution imaging of clouds from the surface may be a means of remotely examining the variation of such turbulence at scales approaching the Kolmogorov scale that may provide an approach to relating these variations to atmospheric turbulence, which we hypothesize may be responsible for the fluctuations in radiance observed on the centimeter scale. Finally, this examination would likely be enhanced by measurements at greater temporal frequency than reported here. The rate of taking images. limited here to 4 s intervals by the write speed to the memory card of the camera, may be expected to be readily overcome.

In summary, the results presented here, albeit limited to a short time period, show similarities and differences in the spatial distribution of COD, all within a domain of about 30 m × 30 m. Such measurements afford the prospect of a powerful new means of studying the properties of clouds at unprecedented spatial resolution that can be expected to enormously advance understanding of cloud properties and the processes responsible for shaping these properties.

Acknowledgments and Data

Supported by the U.S. Department of Energy (DOE) Atmospheric System Research Program (Office of Science, OBER) under Contract No. DE-AC02-98CH10886. We thank the staff at the

ARM Central Great Plains site in Lamont, OK, particularly Matt Gibson and James Martin, for assistance in the deployment. Pilot studies at Brookhaven National Laboratory were carried out with Antonio Aguirre (New York City College of Technology, Brooklyn), with support from the National Science Foundation, Louis Stokes Alliance for Minority Participation (LSAMP), and Clement Li (City College of the City University of New York) with support from the DOE Office of Science, Office of Workforce Development for Teachers and Scientists under the Visiting Faculty Program; and at the City University of New York, with assistance from Yonghua Wu and Zaw Thet Han. We thank Ivan Kotov and Peter Takacs of BNL for assistance in the calibrations. We thank Lorraine Remer, four additional, anonymous reviewers, and the associate editor Anthony Davis for helpful comments.

Original images are archived at http://iop.archive.arm.gov/arm-iop/2015/sgp/sciusi/schwartz-tsi/

Data sets used here from the Atmospheric Radiation Measurement (ARM) Climate Research Facility Southern Great Plains Central Facility, Lamont, OK, all for 07-31-2015, are as follows:

Balloon-Borne Sounding System (SONDEWNPN). Compiled by D. Holdridge, J. Kyrouac and R. Coulter. Accessed 2016-03-22 at http://dx.doi.org/10.5439/1021460

Doppler Lidar (DELFT). Compiled by R. Newsom. Accessed 2015-08-14 at http://dx.doi.org/10.5439/1025185

Multifilter Rotating Shadowband Radiometer (MFRSR). Compiled by G. Hodges. Accessed 2015-10-26 at http://dx.doi.org/10.5439/1023898

Cimel Sunphotometer (CSPHOTAOT). 2015-07-31. Compiled by L. Gregory, L. Ma and R. Wagener. Accessed 2015-10-27 at http://dx.doi.org/10.5439/1025174

Broadband Radiometer Station (BRS). Compiled by M. Sengupta, Y. Xie, A. Habte, I. Reda, M. Dooraghi, A. Andreas and M. Kutchenreiter. Accessed 2016-04-21 at http://dx.doi.org/10.5439/1025160

References

Ansmann, A., Wandinger, U., Riebesell, M., Weitkamp, C. and Michaelis, W., 1992. Independent measurement of extinction and backscatter profiles in cirrus clouds by using a combined Raman elastic-backscatter lidar. *Appl. Optics* **31**, 7113-7131. https://www.osapublishing.org/abstract.cfm?uri=ao-31-33-7113

Barker, H. W., Wielicki, B. A., and Parker, L. (1996). A parameterization for computing grid-averaged solar fluxes for inhomogeneous marine boundary layer clouds. Part II: Validation using satellite data. *J. Atmos. Sci.* **53**, 2304-2316. http://journals.ametsoc.org/doi/abs/10.1175/1520-0469(1996)053%3C2304:APFCGA%3E2.0.CO%3B2

Barron, J. (2015), An Expensive View (but Hardly Expansive) of New York City, *The New York Times*, *June 28*. http://www.nytimes.com/2015/06/29/nyregion/an-intimate-view-of-new-york-through-a-1200-millimeter-lens.html. Accessed 2016-03-16.

Beals, M. J., J. P. Fugal, R. A. Shaw, J. Lu, S. M. Spuler, and J. L. Stith (2015), Holographic measurements of inhomogeneous cloud mixing at the centimeter scale, *Science* **350**, 87-90. http://science.sciencemag.org/content/350/6256/87.short

Bohren, C. F., J. R. Linskens, and M. E. Churma (1995), At What Optical Thickness Does a Cloud Completely Obscure the Sun?, *J. Atmos. Sci.* **52**, 1257-1259, doi:10.1175/1520-0469(1995)052<1257:AWOTDA>2.0.CO;2.

Charlson, R. J., S. E. Schwartz, J. M. Hales, R. D. Cess, J. A. Coakley, J. E. Hansen, and D. J. Hofmann (1992), Climate Forcing by Anthropogenic Aerosols, *Science* **255**, 423-430.

Charlson, R. J., Ackerman, A. S., Bender, F. A. M., Anderson, T. L., and Liu, Z. (2007). On the climate forcing consequences of the albedo continuum between cloudy and clear air. *Tellus* **B 59**, 715-727. http://onlinelibrary.wiley.com/doi/10.1111/j.1600-0889.2007.00297.x/full

Chiu, J. C., A. Marshak, Y. Knyazikhin, W. J. Wiscombe, H. W. Barker, J. C. Barnard, and Y. Luo (2006), Remote sensing of cloud properties using ground-based measurements of zenith radiance, *J. Geophys. Res. Atmos.* **111**, doi:10.1029/2005JD006843.

Chiu, J. C., Marshak, A., Knyazikhin, Y., Pilewski, P., and Wiscombe, W. J. (2009). Physical interpretation of the spectral radiative signature in the transition zone between cloud-free and cloudy regions. *Atmos. Chem. Phys.* **9**, 1419-1430. http://atmos-chem-phys.org/9/1419/2009/acp-9-1419-2009.html

Chiu, J. C., Marshak, A., Knyazikhin, Y., and Wiscombe, W. J. (2010). Spectrally-invariant behavior of zenith radiance around cloud edges simulated by radiative transfer. *Atmos. Chem. Phys.* **10**, 11295-11303. http://www.atmos-chem-phys.net/10/11295/2010/acp-10-11295-2010.pdf

Clark, R. (2016), Notes on the resolution and other details of the human eye, http://www.clarkvision.com/articles/eye-resolution.html. Last updated January 31, 2016; Accessed 2016-03-15.

Cleveland, W.S., Robust locally weighted regression and smoothing scatterplots, *J. Am. Stat. Assoc*. **74**, 829-836, 1977. http://amstat.tandfonline.com/doi/abs/10.1080/01621459.1979.10481038

Clothiaux, E.E., Ackerman, T.P., Mace, G.G., Moran, K.P., Marchand, R.T., Miller, M.A. and Martner, B.E., 2000. Objective determination of cloud heights and radar reflectivities using a combination of active remote sensors at the ARM CART sites. Journal of Applied Meteorology, 39(5), pp.645-665. http://journals.ametsoc.org/doi/abs/10.1175/1520-0450(2000)039%3C0645:ODOCHA%3E2.0.CO%3B2

Davis, A.B. and Marshak, A., 2010. Solar radiation transport in the cloudy atmosphere: a 3D perspective on observations and climate impacts. *Repts. Prog. Phys.* **73**, 026801, pp 1-70. http://iopscience.iop.org/article/10.1088/0034-4885/73/2/026801/meta

Davis, A.B., Marshak, A., Gerber, H. and Wiscombe, W.J., 1999. Horizontal structure of marine boundary layer clouds from centimeter to kilometer scales. *J. Geophys. Res.: Atmospheres* **104**, 6123-6144. http://onlinelibrary.wiley.com/doi/10.1029/1998JD200078/full

Devenish, B. J., B.J., Bartello, P., Brenguier, J.L., Collins, L.R., Grabowski, W.W., IJzermans, R.H.A., Malinowski, S.P., Reeks, M.W., Vassilicos, J.C., Wang, L.P. and Warhaft, Z. (2012), Droplet growth in warm turbulent clouds, *Q. J. Roy. Meteorol. Soc.* **138**, 1401-1429, doi:10.1002/qj.1897.

Eastman, R., and S. G. Warren (2012), A 39-Yr Survey of Cloud Changes from Land Stations Worldwide 1971–2009: Long-Term Trends, Relation to Aerosols, and Expansion of the Tropical Belt, *J. Clim.* **26**, 1286-1303, doi:10.1175/JCLI-D-12-00280.1.

Ehrlich, A., Bierwirth, E., Wendisch, M., Herber, A., and Gayet, J.-F.: Airborne hyperspectral observations of surface and cloud directional reflectivity using a commercial digital camera, *Atmos. Chem. Phys*. **12**, 3493-3510, doi:10.5194/acp-12-3493-2012, 2012.

Ewald, F., Kölling, T., Baumgartner, A., Zinner, T., and Mayer, B.: Design and characterization of specMACS, a multipurpose hyperspectral cloud and sky imager, *Atmos. Meas. Tech*. **9**, 2015-2042, doi:10.5194/amt-9-2015-2016, 2016.

Gabriel, P.M. and Evans, K.F., 1996. Simple radiative transfer methods for calculating domain-averaged solar fluxes in inhomogeneous clouds. *J. Atmos. Sci.* **53**, 858-877. http://journals.ametsoc.org/doi/abs/10.1175/1520-0469(1996)053%3C0858:SRTMFC%3E2.0.CO%3B2

Garcia Mendoza, J., 2012. Characterisation of a multispectral digital camera System for quantitatively comparing complex animal Patterns in natural environments. Thesis, RMIT University, Melbourne, Australia, 2012. https://researchbank.rmit.edu.au/view/rmit:160776/GarciaMendoza.pdf

Gerber, H., Arends, B.G. and Ackerman, A.S., 1994. New microphysics sensor for aircraft use. *Atmos. Res*. **31**, 235-252. http://www.sciencedirect.com/science/article/pii/0169809594900019

Giannakaki, E., Balis, D. S., Amiridis, V., and Kazadzis, S.: Optical and geometrical characteristics of cirrus clouds over a Southern European lidar station, *Atmos. Chem. Phys.* **7**, 5519-5530. doi:10.5194/acp-7-5519-2007, 2007.

Glickman, T. S. (1999), *Glossary of Meteorology*, 2nd Edition ed., American Meteorological Society, Boston. ISBN 9781878220349. http://glossary.ametsoc.org/wiki/Cloud. Last updated 25 April, 2012; Accessed 2015-0320.

Grabowski, W. W., and L.-P. Wang (2013), Growth of cloud droplets in a turbulent environment, *Ann. Rev. Fluid Mechanics* **45**, 293-324. http://www.annualreviews.org/doi/abs/10.1146/annurev-fluid-011212-140750

Harrison, E. F., P. Minnis, B. R. Barkstrom, V. Ramanathan, R. D. Cess, and G. G. Gibson (1990), Seasonal variation of cloud radiative forcing derived from the Earth Radiation Budget Experiment, *J. Geophys. Res. Atmos.* **95**, 18687-18703, doi:10.1029/JD095iD11p18687.

Harrison, L., J. Michalsky, and J. Berndt (1994), Automated multifilter rotating shadow-band radiometer: an instrument for optical depth and radiation measurements, *Appl. Opt.* **33**, 5118-5125. https://www.osapublishing.org/abstract.cfm?uri=ao-33-22-5118

Henyey, L.G. and Greenstein, J.L., 1941. Diffuse radiation in the galaxy. *Astrophys. J.* **93**, 70-83. http://adsabs.harvard.edu/full/1941ApJ....93...70H

Holben, B. N., Eck, T.F., Slutsker, I., Tanre, D., Buis, J.P., Setzer, A., Vermote, E., Reagan, J.A., Kaufman, Y.J., Nakajima, T. and Lavenu, F.. (1998), AERONET—A Federated Instrument Network and Data Archive for Aerosol Characterization, *Remote Sens. Environ.* **66**, 1-16, doi:http://dx.doi.org/10.1016/S0034-4257(98)00031-5.

Hu, J., Razdan, A., and Zehnder, J. A. (2009). Geometric calibration of digital cameras for 3D cumulus cloud measurements. *J. Atmos. Ocean. Tech.* **26**, 200-214. http://journals.ametsoc.org/doi/abs/10.1175/2008JTECHA1079.1

Iwabuchi, H. and Hayasaka, T., 2002. Effects of cloud horizontal inhomogeneity on the optical thickness retrieved from moderate-resolution satellite data. *J. Atmos. Sci*. **72**, 2227-2242. http://dx.doi.org/10.1175/1520-0469(2002)059%3C2227:EOCHIO%3E2.0.CO;2

Kay, J. E., Hillman, B.R., Klein, S.A., Zhang, Y., Medeiros, B., Pincus, R., Gettelman, A., Eaton, B., Boyle, J., Marchand, R. and Ackerman, T. P. (2012), Exposing Global Cloud Biases in the Community Atmosphere Model (CAM) Using Satellite Observations and Their Corresponding Instrument Simulators, *J. Clim.* **25**, 5190-5207, doi:10.1175/JCLI-D-11-00469.1.

Koehler, T.L., Johnson, R.W. and Shields, J.E., 1991. Status of the whole sky imager database. In Proceedings of the Cloud Impacts on DOD Operations and Systems, 1991 Conference (pp. 77-80). http://jshields.ucsd.edu/publications/pdfs/11%20Koehler%20CIDOS%2091.pdf

Koren, I., Remer, L.A., Kaufman, Y.J., Rudich, Y. and Martins, J.V., 2007. On the twilight zone between clouds and aerosols. Geophys, Res. Lett. **34**, L08805. http://onlinelibrary.wiley.com/doi/10.1029/2007GL029253/full

Kokhanovsky, A. (2004). Optical properties of terrestrial clouds. *Earth-Science Revs.* **64**, 189-241. doi:10.1016/S0012-8252(03)00042-4

Kumala, W., K. E. Haman, M. K. Kopec, D. Khelif, and S. P. Malinowski (2013), Modified ultrafast thermometer UFT-M and temperature measurements during Physics of Stratocumulus Top (POST), *Atmos. Meas. Tech.* **6**, 2043-2054, doi:10.5194/amt-6-2043-2013.

Leahy, L. V., R. Wood, R. J. Charlson, C. A. Hostetler, R. R. Rogers, M. A. Vaughan, and D. M. Winker (2012), On the nature and extent of optically thin marine low clouds, *J. Geophys. Res. Atmos.* **117**, doi:10.1029/2012JD017929.

LeBlanc, S. E., Pilewskie, P., Schmidt, K. S., and Coddington, O.: A spectral method for discriminating thermodynamic phase and retrieving cloud optical thickness and effective radius using transmitted solar radiance spectra, *Atmos. Meas. Tech*. **8**, 1361-1383, doi:10.5194/amt-8-1361-2015, 2015.

Lebourgeois, V., Begue, A., Labbe, S., Mallavan, B., Prevot, L., and Roux, B.: Can commercial digital cameras be used as multispectral sensors? A crop monitoring test. *Sensors* **8**, 73007322, doi:10.3390/s8117300, 2008.

Lewis, G. M., P. H. Austin, and M. Szczodrak (2004), Spatial statistics of marine boundary layer clouds, *J. Geophys. Res*. **109**, D04104, doi:10.1029/2003JD003742

Li, Q., W. Lu, and J. Yang (2011), A Hybrid Thresholding Algorithm for Cloud Detection on Ground-Based Color Images, *J. Atmos. Ocean. Tech.* **28**, 1286-1296, doi:10.1175/JTECH-D-11-00009.1.

Long, C. N., J. M. Sabburg, J. Calbó, and D. Pagès (2006), Retrieving Cloud Characteristics from Ground-Based Daytime Color All-Sky Images, *J. Atmos. Ocean. Tech.* **23**, 633-652, doi:10.1175/JTECH1875.1.

McFarquhar, G. M., Heymsfield, A. J., Spinhirne, J., and Hart, B. (2000). Thin and subvisual tropopause tropical cirrus: Observations and radiative impacts. *J. Atmos. Sci.* **57**, 1841-1853. http://journals.ametsoc.org/doi/full/10.1175/1520-0469(2000)057%3C1841:TASTTC%3E2.0.CO%3B2

Marchand, R., T. Ackerman, M. Smyth, and W. B. Rossow (2010), A review of cloud top height and optical depth histograms from MISR, ISCCP, and MODIS. *J. Geophys. Res. Atmos.* **115**, doi:10.1029/2009JD013422.

Marshak, A., Davis, A., Cahalan, R.F. and Wiscombe, W., 1998. Nonlocal independent pixel approximation: Direct and inverse problems. *IEEE Trans. Geosci. Remote Sensing* **36**, 192-205. http://ieeexplore.ieee.org/xpls/abs_all.jsp?arnumber=655329

Marshak, A., Knyazikhin, Y., Chiu, J. C., and Wiscombe, W. J. (2009). Spectral invariant behavior of zenith radiance around cloud edges observed by ARM SWS. *Geophys. Res. Lett.* **36**. http://onlinelibrary.wiley.com/doi/10.1029/2009GL039366/full

Martins, E., V. Noel, and H. Chepfer (2011), Properties of cirrus and subvisible cirrus from nighttime Cloud-Aerosol Lidar with Orthogonal Polarization (CALIOP), related to atmospheric dynamics and water vapor, *J. Geophys. Res. Atmos.* **116**, doi:10.1029/2010JD014519.

Mather, J. H., and J. W. Voyles (2012), The Arm Climate Research Facility: A Review of Structure and Capabilities, *Bull. Amer. Meteorol. Soc.* **94**, 377-392, doi:10.1175/BAMS-D-11-00218.1.

Mauer, C 2009 Measurement of the spectral response of digital cameras with a set of interference filters Diploma Thesis University of Applied Sciences Cologne. http://www.image-engineering.de/content/library/diploma_thesis/christian_mauer_spectral_response.pdf

Mitrescu, C., Lidar model with parameterized multiple scattering for retrieving cloud optical properties, *J. Quant. Spectrosc. Radiat. Transf.* **94**, 201–224, doi: 10.1016/j.jqsrt.2004.10.006, 2005

Mejia, F. A., Kurtz, B., Murray, K., Hinkelman, L. M., Sengupta, M., Xie, Y., and Kleissl, J. 2016. Coupling sky images with radiative transfer models: a new method to estimate cloud optical depth. *Atmos. Meas. Tech.* **9**, 4151-4165. http://www.atmos-meas-tech.net/9/4151/2016/amt-9-4151-2016.pdf

Nam, C., S. Bony, J.-L. Dufresne, and H. Chepfer (2012), The ‘too few, too bright’ tropical low-cloud problem in CMIP5 models, *Geophys. Res. Lett.* **39**, L21801, doi:10.1029/2012GL053421.

Niple, E. R., Scott, H. E., Conant, J. A., Jones, S. H., Iannarilli, F. J., and Pereira, W. E.: Application of oxygen A-band equivalent width to disambiguate downwelling radiances for cloud optical depth measurement, *Atmos. Meas. Tech.* **9**, 4167-4179, doi:10.5194/amt-9-4167-2016, 2016.

Öktem, R., Lee, J., Thomas, A., Zuidema, P., and Romps, D. M. (2014). Stereophotogrammetry of Oceanic Clouds. *J. Atmos. Ocean. Tech.* **31**, 1482-1501. http://journals.ametsoc.org/doi/abs/10.1175/JTECH-D-13-00224.1

Pearson, G., F. Davies, and C. Collier (2009), An Analysis of the Performance of the UFAM Pulsed Doppler Lidar for Observing the Boundary Layer, *J. Atmos. Ocean. Tech.* **26**, 240-250, doi:10.1175/2008JTECHA1128.1.

Pincus, R., McFarlane, S. A., and Klein, S. A. (1999). Albedo bias and the horizontal variability of clouds in subtropical marine boundary layers: Observations from ships and satellites. *J. Geophys. Res. Atmos.* **104**, 6183-6191.

Pincus, R., S. Platnick, S. A. Ackerman, R. S. Hemler, and R. J. P. Hofmann (2012), Reconciling Simulated and Observed Views of Clouds: MODIS, ISCCP, and the Limits of Instrument Simulators, *J. Clim.* **25**, 4699-4720, doi:10.1175/JCLI-D-11-00267.1.

Platnick, S., and S. Twomey (1994), 11th conference on clouds and precipitation Remote sensing the susceptibility of cloud albedo to changes in drop concentration, *Atmos. Res.* **34**, 85-98, doi:http://dx.doi.org/10.1016/0169-8095(94)90082-5.

Qian, Y., C. N. Long, H. Wang, J. M. Comstock, S. A. McFarlane, and S. Xie (2012), Evaluation of cloud fraction and its radiative effect simulated by IPCC AR4 global models against ARM surface observations, *Atmos. Chem. Phys.* **12**, 1785-1810, doi:10.5194/acp-12-1785-2012.

Romps, D. M., and Öktem, R. (2015). Stereo photogrammetry reveals substantial drag on cloud thermals. *Geophys. Res. Lett.* **42**, 5051-5057. http://onlinelibrary.wiley.com/doi/10.1002/2015GL064009/full

Rossow, W. B., and R. A. Schiffer (1999), Advances in Understanding Clouds from ISCCP, *Bull. Amer. Meteorol. Soc.* **80**, 2261-2287, doi:10.1175/1520-0477(1999)080<2261:AIUCFI>2.0.CO;2.

Sachs, D., Lovejoy, S., and Schertzer, D. (2002). The multifractal scaling of cloud radiances from 1 m to 1 km. *Fractals* **10**, 253-264. http://www.worldscientific.com/doi/abs/10.1142/S0218348X02001385

Saito, M., Iwabuchi, H. and Murata, I., 2016. Estimation of spectral distribution of sky radiance using a commercial digital camera. *Appl. Opt.* **55**, 415-424. https://www.osapublishing.org/abstract.cfm?uri=ao-55-2-415

Schade, N. H., Macke, A., Sandmann, H., and Stick, C.: Total and partial cloud amount detection during summer 2005 at Westerland (Sylt, Germany), *Atmos. Chem. Phys*. **9**, 11431150, doi:10.5194/acp-9-1143-2009, 2009

Schäfer, M., Bierwirth, E., Ehrlich, A., Heyner, F., and Wendisch, M.: Retrieval of cirrus optical thickness and assessment of ice crystal shape from ground-based imaging spectrometry, *Atmos. Meas. Tech*. **6**, 18551868, doi:10.5194/amt-6-1855-2013, 2013

Schuster, G. L., O. Dubovik, and B. N. Holben (2006), Angstrom exponent and bimodal aerosol size distributions, *J. Geophys. Res*. **111**, D07207, doi:10.1029/2005JD006328.

Siebert, H., K. Lehmann, and M. Wendisch (2006), Observations of Small-Scale Turbulence and Energy Dissipation Rates in the Cloudy Boundary Layer, *J. Atmos. Sci.* **63**, 1451-1466, doi:10.1175/JAS3687.1.

Stamnes, K., S. Tsay, W. Wiscombe, and K. Jayaweera (1988), Numerically stable algorithm for discrete-ordinate-method radiative transfer in multiple scattering and emitting layered media, *Appl. Opt.* **27**, 2502-2509.

Stephens G. L., D.G. Vane, R.J. Boain, G. G. Mace, K. Sassen, Z. Wang, A. J. Illingworth, E. J. O'Connor, W.B. Rossow, S. L .Durden, S. D. Miller, R. T. Austin, A. Benedetti, C. Mitrescu, and the CloudSat Science Team. The CloudSat mission and the A-Train: A new dimension of space-based observations of clouds and precipitation. *Bull. Am. Meteorol. Soc*. **83**, 1771–1790, 2002. http://journals.ametsoc.org/doi/abs/10.1175/BAMS-83-12-1771

Stokes, G. M., and S. E. Schwartz (1994), The Atmospheric Radiation Measurement (ARM) Program: Programmatic Background and Design of the Cloud and Radiation Test Bed, *Bull. Amer. Meteorol. Soc.* **75**, 1201-1221, doi:10.1175/1520-0477(1994)075<1201:TARMPP>2.0.CO;2.

Stubenrauch, C. J., Rossow, W.B., Kinne, S., Ackerman, S., Cesana, G., Chepfer, H., Di Girolamo, L., Getzewich, B., Guignard, A., Heidinger, A. and Maddux, B.C. (2013), Assessment of Global Cloud Datasets from Satellites: Project and Database Initiated by the GEWEX Radiation Panel, *Bull. Amer. Meteorol. Soc.* **94**, 1031-1049, doi:10.1175/BAMS-D-12-00117.1.

Sun, W., Videen, G., Kato, S., Lin, B., Lukashin, C., and Hu, Y. (2011). A study of subvisual clouds and their radiation effect with a synergy of CERES, MODIS, CALIPSO, and AIRS data. *J. Geophys. Res. Atmos.* **116**. http://onlinelibrary.wiley.com/doi/10.1029/2011JD016422/full

Sun, W., G. Videen, and M. I. Mishchenko (2014), Detecting super-thin clouds with polarized sunlight, *Geophys. Res. Lett.* **41**, 688–693, doi:10.1002/ 2013GL058840

ten Brink, H. M., S. E. Schwartz, and P. H. Daum (1987), Efficient scavenging of aerosol sulfate by liquid-water clouds, *Atmos. Environ.* **21**, 2035-2052, doi:http://dx.doi.org/10.1016/0004-6981(87)90164-8.

Turner, D. D., A. M. Vogelmann, R. T. Austin, J. C. Barnard, K. Cady-Pereira, J. C. Chiu, S. A. Clough, C. Flynn, M. M. Khaiyer, J. Liljegren, K. Johnson, B. Lin, C. Long, A. Marshak, S. Y. Matrosov, S. A. McFarlane, M. Miller, Q. Min, P. Minnis, W. O'Hirok, Z. Wang and W. Wiscombe. (2007), Thin Liquid Water Clouds: Their Importance and Our Challenge, *Bull. Amer. Meteorol. Soc.* **88**, 177-190, doi:10.1175/BAMS-88-2-177.

Twohy, C.H., Coakley, J.A. and Tahnk, W.R., 2009. Effect of changes in relative humidity on aerosol scattering near clouds. *J. Geophys. Res.: Atmos* **114** D05205. http://onlinelibrary.wiley.com/doi/10.1029/2008JD010991/full

Twomey, S. (1974), Pollution and the planetary albedo, *Atmos. Environ.* **8**, 1251-1256, doi:http://dx.doi.org/10.1016/0004-6981(74)90004-3.

Urquhart, B., Kurtz, B., Dahlin, E., Ghonima, M., Shields, J.E. and Kleissl, J., 2015. Development of a sky imaging system for short-term solar power forecasting. *Atmos. Meas. Tech*. **8**, 875-890. http://www.atmos-meas-tech.net/8/875/2015/amt-8-875-2015.html

Wang, H., and W. Su (2013), Evaluating and understanding top of the atmosphere cloud radiative effects in Intergovernmental Panel on Climate Change (IPCC) Fifth Assessment Report (AR5) Coupled Model Intercomparison Project Phase 5 (CMIP5) models using satellite observations, *J. Geophys. Res. Atmos*. **118**, 683–699, doi:10.1029/2012JD018619.

Wang, P.-H., P. Minnis, M. P. McCormick, G. S. Kent, G. K. Yue, D. F. Young, and K. M. Skeens (1998), A study of the vertical structure of tropical (20°S–20°N) optically thin clouds from SAGE II observations, *Atmos. Res.* **47–48**, 599-614, doi:http://dx.doi.org/10.1016/S0169-8095(97)00085-9.

Warren, S. G., C. J. Hahn, J. London, R. M. Chervin, and R. L. Jenne (1986), Global distribution of total cloud cover and cloud type amounts over land. NCAR Technical note TN—273+STR National Center for Atmospheric Research, Boulder CO. http://www.atmos.washington.edu/CloudMap/Atlases/DistLand.pdf

Warren, S. G., C. J. Hahn, J. London, R. M. Chervin, and R. L. Jenne (1988), Global distribution of total cloud cover and cloud type amounts over the ocean. NCAR Technical note TN—317+STR National Center for Atmospheric Research, Boulder CO. http://www.atmos.washington.edu/CloudMap/Atlases/SimLand.pdf

Wielicki, B. A., and L. Parker (1992), On the determination of cloud cover from satellite sensors: The effect of sensor spatial resolution, *J. Geophys. Res. Atmos.* **97**, 12799-12823, doi:10.1029/92JD01061.

Winker, D., B. Getzewitch, and M. Vaughan (2008), Evaluation and applications of cloud climatologies from CALIOP. 24th International Laser Radar Conference, Natl. Cent. for Atmos. Res., Boulder, Colo. http://ntrs.nasa.gov/archive/nasa/casi.ntrs.nasa.gov/20080024183.pdf

Xi, B., X. Dong, P. Minnis, and M. M. Khaiyer (2010), A 10 year climatology of cloud fraction and vertical distribution derived from both surface and GOES observations over the DOE ARM SPG site, *J. Geophys. Res. Atmos.* **115**, doi:10.1029/2009JD012800.

Zehnder, J. A., Hu, J., and Razdan, A. (2007). A stereo photogrammetric technique applied to orographic convection. *Mon. Weather Rev.* **135**, 2265-2277. http://journals.ametsoc.org/doi/abs/10.1175/MWR3401.1

Zhao, G., and L. Di Girolamo (2007), Statistics on the macrophysical properties of trade wind cumuli over the tropical western Atlantic, *J. Geophys. Res. Atmos.* **112**, doi:10.1029/2006JD007371.

Zuidema, P., D. Leon, A. Pazmany, and M. Cadeddu (2012), Aircraft millimeter-wave passive sensing of cloud liquid water and water vapor during VOCALS-REx, *Atmos. Chem. Phys.* **12**, 355-369, doi:10.5194/acp-12-355-2012.

High-Resolution Photography of Clouds from the Surface: Retrieval of Cloud Optical Depth down to Centimeter Scales

Supporting Information

Stephen E. Schwartz[1], Dong Huang[1]*, and Daniela Viviana Vladutescu[2]

With contributions from Antonio Aguirre[2]†, Clement Li[3]‡

[1]Environmental and Climate Sciences, Brookhaven National Laboratory. [2]New York City College of Technology of the City University of New York. [3]City College of the City University of New York.

*Current address, Science Systems and Applications Inc., Greenbelt, MD

†Graduated (sadykov1@yahoo.com)

‡Graduated (liclement.h@gmail.com)

S1 Radiation transfer calculations

The DISORT code (Stamnes et al., 1998) was used, with 16 streams for the angular discretization. A single layer was assumed, as the vertical distribution of clouds has only secondary effects on the nadir radiance for plane-parallel calculations. The radiation transfer (RT) calculations were performed for the incident radiation consisting of the direct (solar) beam only; the lower boundary was taken as non-reflective.

The scattering phase function $p(\theta)$, where θ is the scattering angle, was computed as the optical-depth–weighted average of the phase functions for Rayleigh scattering (R, $\omega = 1.0$, $g = 0.5$) and Mie scattering (M, $\omega = 1.0$, $g = 0.85$; Kokhanovsky, 2004), where ω is the single scattering albedo, taken as unity (conservative scattering), and g is the asymmetry parameter; *i.e.*,

$$p = (p_R \tau_R + p_M \tau_M)/(\tau_R + \tau_M) .$$

The Rayleigh phase function, normalized to unity, is

$$p_R(\theta) = \frac{3}{16\pi}(1 + \cos^2\theta) .$$

The Mie phase function, also normalized to unity, was approximated using the Henyey-Greenstein (1941) parameterization,

$$p_M(\theta) = \frac{1}{4\pi}\frac{1 - g^2}{[1 + g^2 - 2g\cos\theta]^{3/2}} .$$

The Rayleigh optical depths were taken as 0.2043 and 0.0572 for the blue (460 nm) and red (640 nm) wavelengths, respectively. The RT calculations were performed for Mie optical depth from 0 to 150 and for solar zenith angle from 0 to 80°. The output of the RT calculation is the normalized zenith radiance, the zenith radiance per hemispheric solar irradiance at the top of the atmosphere, with unit sr^{-1}, Figure 1.

S2 Camera Properties

S2.1 Resolution tests.

Photographs were taken at a distance of 1.06 km of target on which had been printed rectangles of height 3.1 cm and width 1, 2, 4, and 8 cm (with the same separation distances). Shown in Figure S1 are a full 4608 × 3456 pixel RGB image and successive zooms, an image of the target, false color image of red channel of target area, and line profile, of single pixel height, of the red-channel image of 4 cm wide rectangles showing the ability of the camera to resolve images of this angular dimension (4 cm at 1 km is 40 mrad). The 2 cm rectangles are also discernible in the false color image. The resolution determined in this way conforms closely to that expected by diffraction limitation for the camera optics.

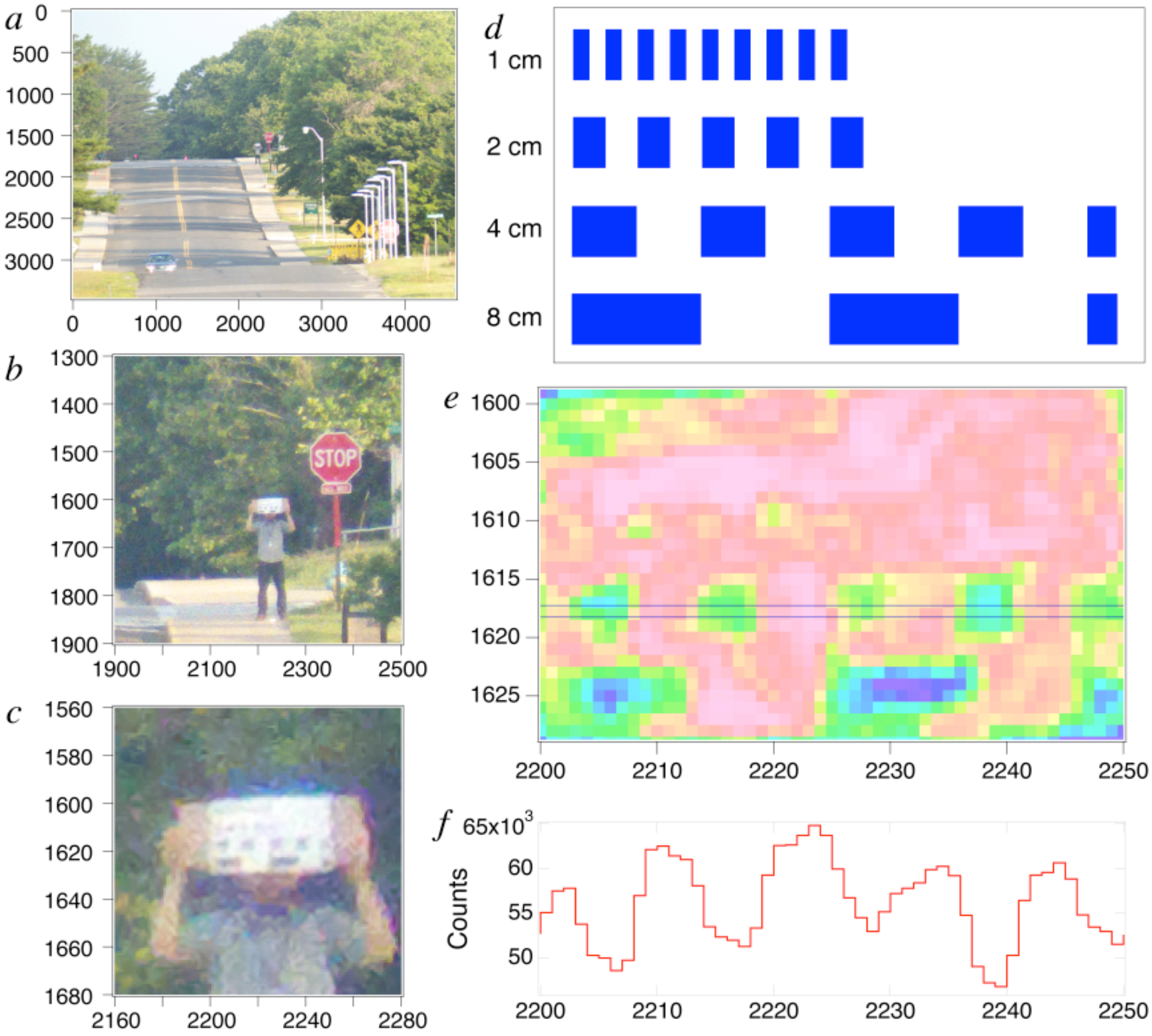

Figure S1. Examination of resolving power of camera. (*a*) Full 4608 × 3456 RGB photo at 1.06 km; axes give pixel number. (*b*), (*c*) Image in *a* at successively higher zoom. (*d*) Image of target, showing dimensions of rectangles. (*e*) False color image of target, with lines bounding pixels for which counts are determined. (*f*) Line profile of counts, on pixel-by-pixel basis of pixels demarcated in *e*, vertically aligned with images in *d* and *e*.

S2.2 Spectral sensitivity.

Spectral responses of CMOS (Complementary Metal Oxide Semiconductor) sensors employed in digital cameras depend on manufacturing details and differ from camera to camera [Lebourgeois et al., 2008; Mauer, 2009; Garcia Mendoza, 2012; Ehrlich et al., 2012; Saito et al., 2016]. Here a relative calibration of the wavelength response of the three color channels of the camera was made with an integrating sphere, mercury xenon source, and NIST calibrated photodiode; the photodiode was mounted adjacent to the lens of the camera in the output beam of the integrating sphere. Relative sensitivity, calculated as counts per second of exposure time divided by power received by the photodiode, counts/joule, does not take into account area of the photodiode nor area of the limiting aperture of the camera. Absolute sensitivity was not required to determine the scaled normalized zenith radiance for each channel as described in Text.

The relative spectral sensitivity determined for each of the color channels, Figure S2, exhibits peaks for the blue and red channels, respectively, of 460 and 640 nm. The strong dip in blue channel response at 440 nm is attributed to saturation of the camera sensor at this wavelength because of a high-intensity mercury line. No explanation was identified for the apparent slight sensitivity of the blue channel in the vicinity of 650 nm. As this sensitivity extends over several wavelength intervals, it is considered a property of the camera, which is attributed to transmittance of the dye employed for color separation at the sensor. However, as the magnitude of this response is small it was neglected in the analysis.

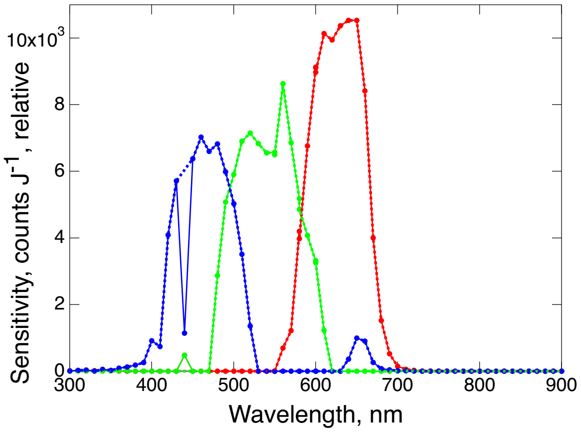

Figure S2. Relative spectral sensitivity of each of the three color channels. Dip in blue sensitivity (and peak in green sensitivity) at 440 nm is considered an artifact.

Determination of the relative wavelength response also permits examination of the magnitude of error that might arise from using the single peak wavelength in the RT calculations and in the retrieval of COD. The asymmetry parameter for Rayleigh scatter is wavelength independent, and for the cloud drops nearly unchanged [e.g., Kokhanovsky, 2004]. Likewise the cloud drop scattering is nearly wavelength-independent. So the only significant wavelength dependence is that of Rayleigh scattering, which varies as λ^{-4}. For the red and blue channels, $\langle \lambda^{-4} \rangle^{-1/4}$ = 622 and 461 nm, respectively, quite close to the peaks of the wavelength response employed in the analysis, 640 and 460 nm, respectively. Hence the consequence of the non monochromatic response of the red and blue channels is considered minimal in the RT calculations and in the retrievals.

S2.3 Intensity calibrations and correction for nonlinearity

Radiometric calibrations were carried out to ascertain the response function of the camera. The Hg-Xe lamp / monochromator / integrating-sphere source was used as in the wavelength calibrations. Calibrations were carried out at 460 and 640 nm. At each wavelength a series of photographs was taken at diminishing intensities as controlled by decreasing the width of the inlet slit of the monochromator. Camera exposure was ~1 s and aperture ratio *f*/5.6, but other camera settings were used as in field measurements (35-mm equivalent focal length, 1200 mm; focus ~ ∞). Radiant intensity was measured by a calibrated photodiode located within the integrating sphere. The number of counts in a given pixel was read from 16-bit TIFF files generated from the raw image files using the software provided with the camera (Raw File Converter EX by Silkypix, Version 3.2.20.0) with the parameter γ set equal 1, γ being the exponent of a power law used to relate intensity to counts in the generated TIFF file. At any given intensity the TIFF image obtained in this way appeared quite uniform spatially, as shown in an example obtained for 640 nm, Figure S3. Departure from uniformity was manifested as slight gradient in counts across the image; this is tentatively attributed to the camera not being perfectly aligned with the central axis of the divergent beam exiting from the integrating sphere. The corresponding histogram, Figure S4, was quite sharply peaked; attention is called to the non-zero count rate in the blue channel indicative of the slight sensitivity of this channel to the red wavelength noted above.

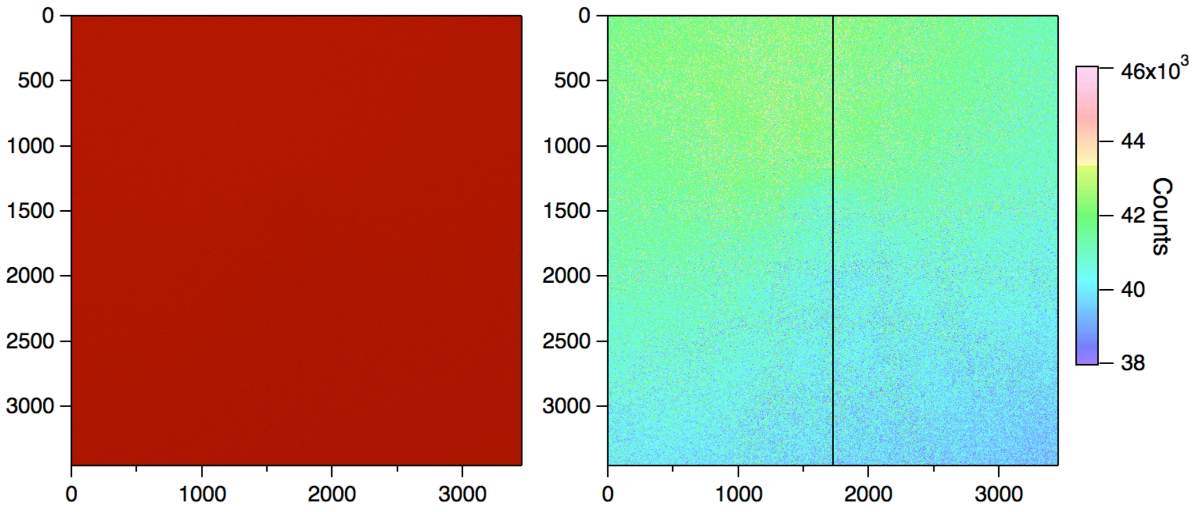

Figure S3. Example of RGB image and false color image of red channel counts obtained for calibration with 640 nm radiation. Vertical line is locus of line profile used in sensor noise analysis, Section S2.4.

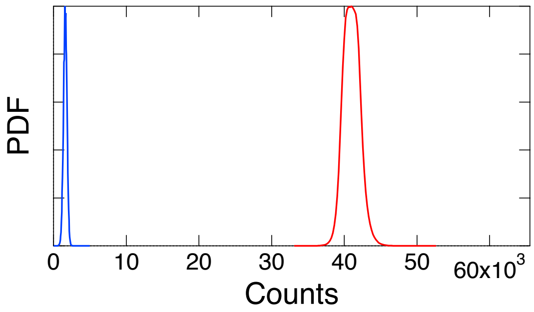

Figure S4. Histograms of counts in red and blue channels of image shown in Figure S3 for illumination by 640 nm radiation.

Calibration was performed by examining dependence of mean counts on radiant intensity exiting from the integrating sphere (as measured by photodiode current), examples of which are shown in Figure S5 (top row) for the red and blue channels, both of which exhibited a negative departure from linearity. Such decrease in counts with increasing intensity is employed in digital photography to artificially enhance dynamic range by increasing apparent response at low light level and decreasing it at high light level; commonly a power law is used for this relation. In order to linearize the response the photocurrent the photodiode current was fit to a power law with exponent denoted here β, $I = C^{\beta}$; both the red and blue channels were found to be closely fit for $\beta = 1.8$, Figure S5, second row. Using this exponent to determine what is denoted here as a linearized count rate from the count rate as $C_{\text{lin}} = C^{\beta}$ yielded a quantity that conforms closely to the desired linear relation. This power-law transform was employed in the analysis of the TIFF images examined in this study.

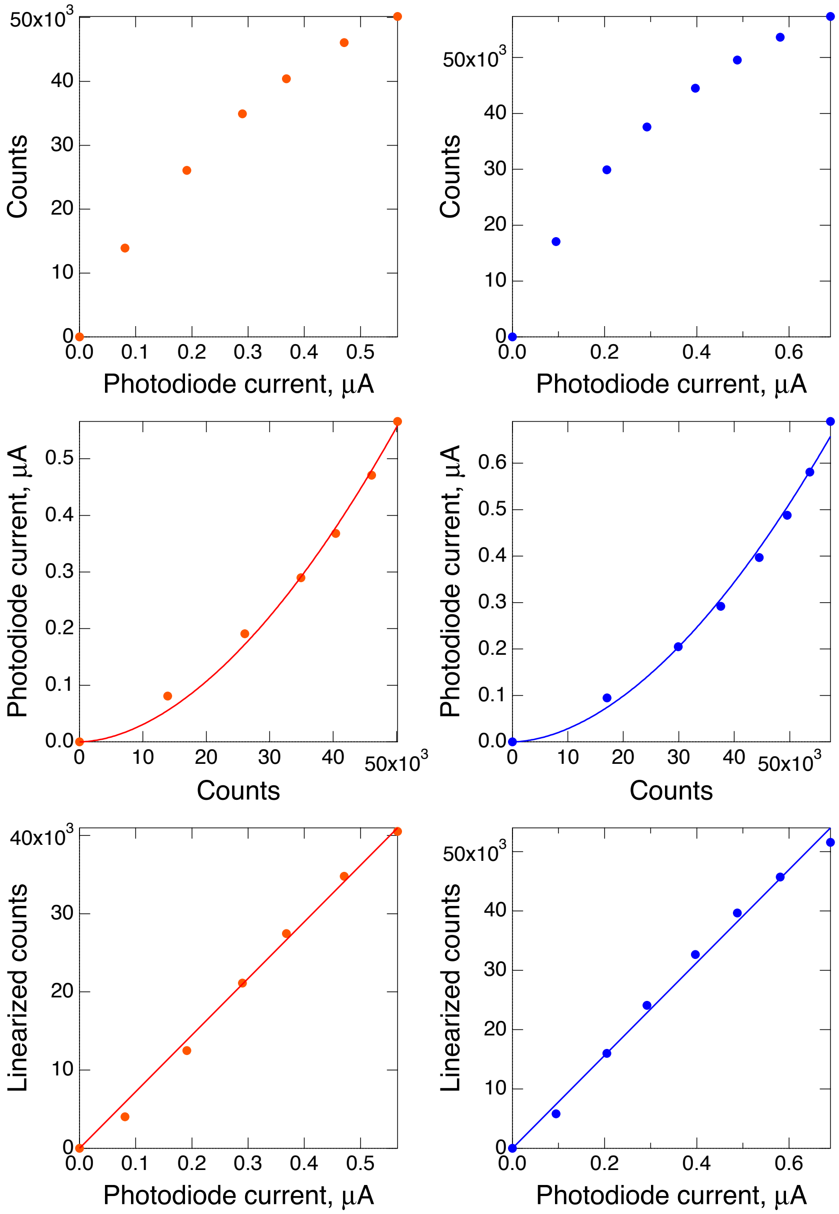

Figure S5. *Top*: Dependence of counts on radiant intensity (as measured by photodiode current) in red (*left*) and blue (*right*) channels. *Middle*: Fit of photodiode current to counts by power law with exponent β = 1.8. *Bottom*: Graph of linearized counts evaluated from measured counts by power law with exponent β = 1.8 versus photodiode current.

S2.4 Sensor noise

Sensor noise was examined using calibration images and also in cloud images. For the calibration images, if the image of the beam emanating from the integrating sphere were entirely uniform, it would be possible to infer camera noise simply from the variance in the signal. As seen in Figure S3 there is a gradient in the signal (tentatively ascribed to the camera not being centered on the optical axis of the integrating sphere). This problem was circumvented in several ways. First, a homogeneous region of radiant intensity was identified and spread in signal was quantified, Figure S6. The histogram is reasonably symmetric and roughly gaussian. The mean and standard deviation of the counts in the sub-region were 42195 and 863 counts; relative standard deviation, RSD, 0.020.

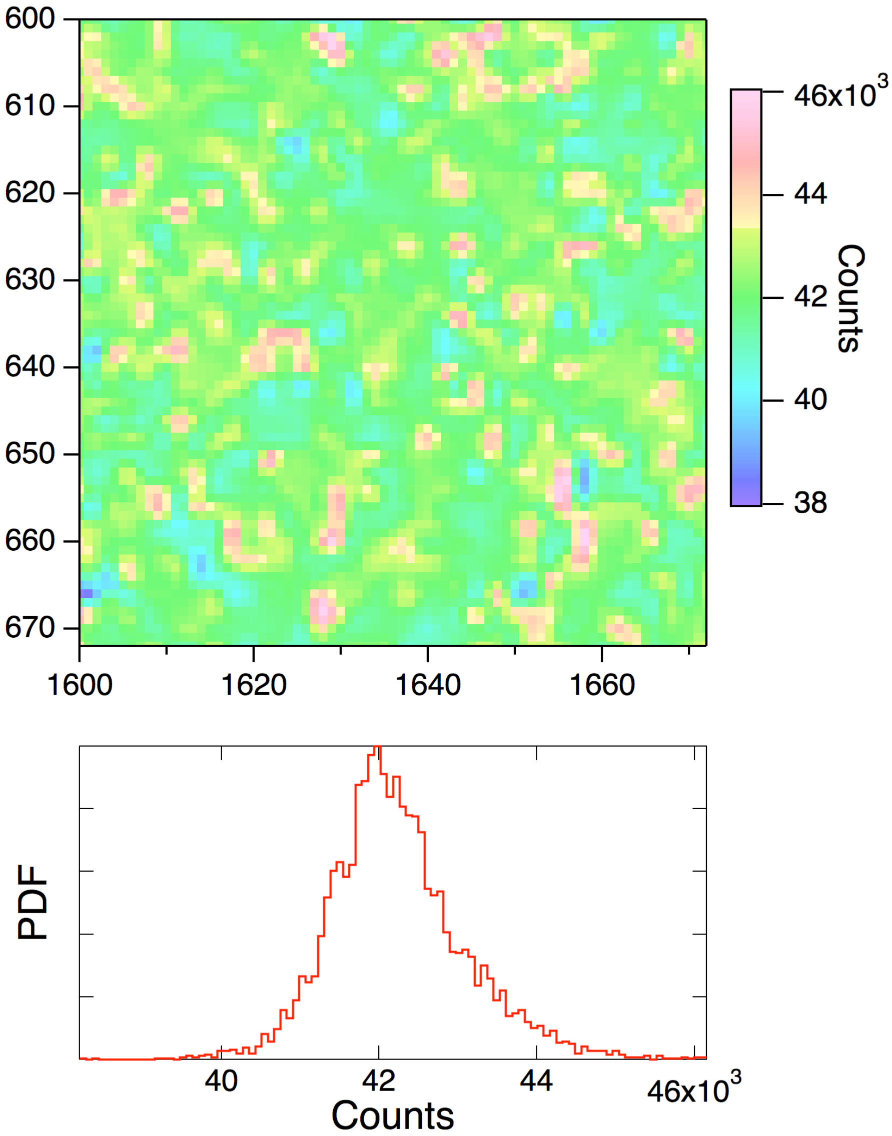

Figure S6. *Top*, Homogeneous region of image shown in Figure S3 identified as suitable for noise analysis. *Bottom*, Histogram of counts in that figure.

A second, less subjective approach was analyze line profiles in a single dimension. For this analysis three intensities were selected to examine the dependence of noise on signal. At each intensity a single line profile was selected for analysis. Because of gradient across the image it was necessary to subtract a smoothed curve that represented the larger scale variation in intensity, for which purpose the LOESS (locally weighted scatterplot smoothing [Cleveland et al., 1977]) procedure was employed. The LOESS procedure is rather robust against the effects of outliers, making it well suited for noise analysis. For this analysis a line profile of counts was obtained for width of a single pixel down the entire image, as shown in Figure S3; the corresponding line profile is shown in Figure S7 along with three LOESS fits and the corresponding residuals. The LOESS fitting procedure requires specification of the width of the window that influences the value of a given point in the fit. Sensitivity to width of the fitting window was slight, with RSD of the residual calculated as standard deviation of the residual divided by the mean of the original counts, 0.023 – 0.024, essentially identical to that obtained in the analysis for a homogeneous area. Examination of RSD at several intensities spanning the range in the cloud photographs showed it to essentially constant, 0.025 ± 0.002, increasing slightly for lower intensities.

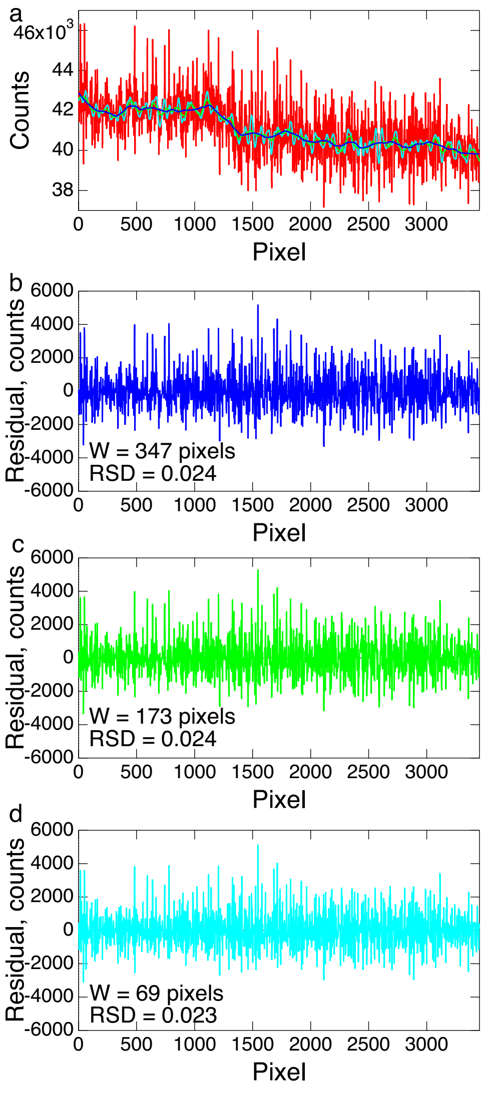

Figure S7. (*a*) Line profile of counts in individual pixels along the line shown in Figure S3*b*, red, and of LOESS fits to that profile using windows of 347 (blue), 173 (green), and 69 (cyan) pixels. (*b*)-(*d*) Difference between counts along the line profile and LOESS fits for the three window values. Relative standard deviation RSD for each of the differences is calculated as standard deviation of the difference divided by mean of the line profile.

A third approach to determination of sensor noise was from the difference signal of successive calibration images, as illustrated in Figure S8. Panel *a* shows line profiles vertically down the image for a single pixel as shown in Figure S3. Here the two line profiles are displaced by 2000 counts as indicated by the two scales. Although the trend along the line profile is similar for each image, a consequence of gradient in intensity across the image; the gradient is absent in the difference. The noise features in the two line profiles are uncorrelated, as indicted by panel *b*, which shows a scatter plot between identical pixels in the successive images, the correlation in that graph being due to the overall gradient across the line profiles. Panel *c* shows the virtual identity of the histograms of the two images (the entire images, not just the line profiles) and the near-zero histogram of the difference, the slight displacement of the difference histogram from zero being attributed to slight change in lamp intensity between the two images. The standard deviations of the counts in the two images are 557 and 563 counts; the standard deviation of the difference is 520 counts, the lower value reflective of the gradient being absent in the difference. Under the assumption that the noise in each of the two line profiles is uncorrelated, the standard deviation in the difference signal would be expected be greater than that of the noise in an individual line profile. Dividing that standard deviation by square root of 2 yields another estimate of the standard deviation noise of the measurement, 368 counts, corresponding to RSD 0.027.

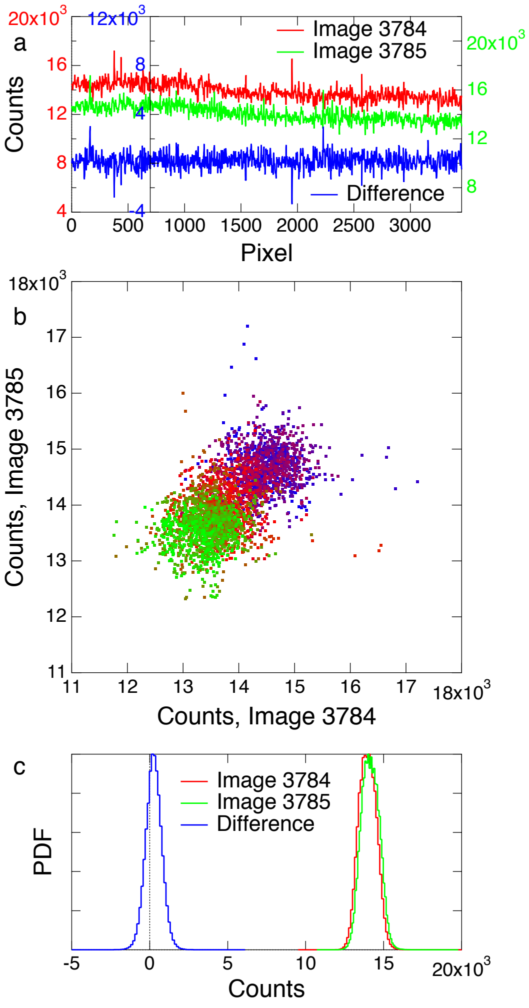

Figure S8. Comparison of two successive images. (*a*) Line profiles of single pixel width for the two images and for the difference. (*b*) Pixel-by-pixel scatter plot of counts in the line profiles of the two images; color code denotes pixel location: blue, low; green, high. (*c*) Histograms of the images (entire images, not just the line profiles) and of the difference.

A final examination of noise was conducted using actual cloud images; an example is shown in Figure S9. Panel *a* shows line trace for which the profile of single-pixel linearized counts drawn through sub-regions of fairly uniform values of radiance (low value, A; high value C) and a region of strong gradient, B; panel *b* shows corresponding line profile. Because of the variation in signal with position, noise is evaluated as the difference between the data and a LOESS fit, although this difference includes any actual spatial variation of radiance within the window of the LOESS fit. Attention is called to the increasing magnitude of the difference with increasing signal. RSDs for the two sub-regions of fairly constant count rate, 0.031 and 0.037, evaluated as standard deviation of the difference between the signal and the fit divided by the mean of the signal were insensitive to the width of the LOESS window. The fact that these values are slightly higher than the values obtained with the calibration data suggests slight contribution to variance from variation of the cloud radiance within the width of the LOESS windows.

Camera dark noise was examined by inspection of dark images (taken with lens cap on). The signal consists mainly of a regular pattern, average about 6 counts, standard deviation 5 counts, on scale of 0 to 65535, a consequence of the averaging of adjacent pixels of the same color on the CMOS (Complementary Metal Oxide Semiconductor) array that comprises the detector to obtain registered RGB counts. An error of this magnitude is of no consequence here. However somewhat surprising was the existence of star-like patterns consisting of a central pixel of magnitude up to several hundred counts, falling off to background within 2 pixels of the central peak in all four directions, perhaps 1000 such stars in a given image, not at the same location in successive images, although none of this has been systematically examined. It is hypothesized that such stars are caused by energetic charged particles (cosmic rays, radioactive decay), but the number of such stars, if they are all produced during the time of the exposure (0.5 ms) far exceeds expectation of the frequency of such events. In any event such individual events are small relative to noise values and are of little consequence here.

In sum the assessments of sensor noise suggest a noise associated with the measurements, expressed as relative standard deviation, of about 0.025.

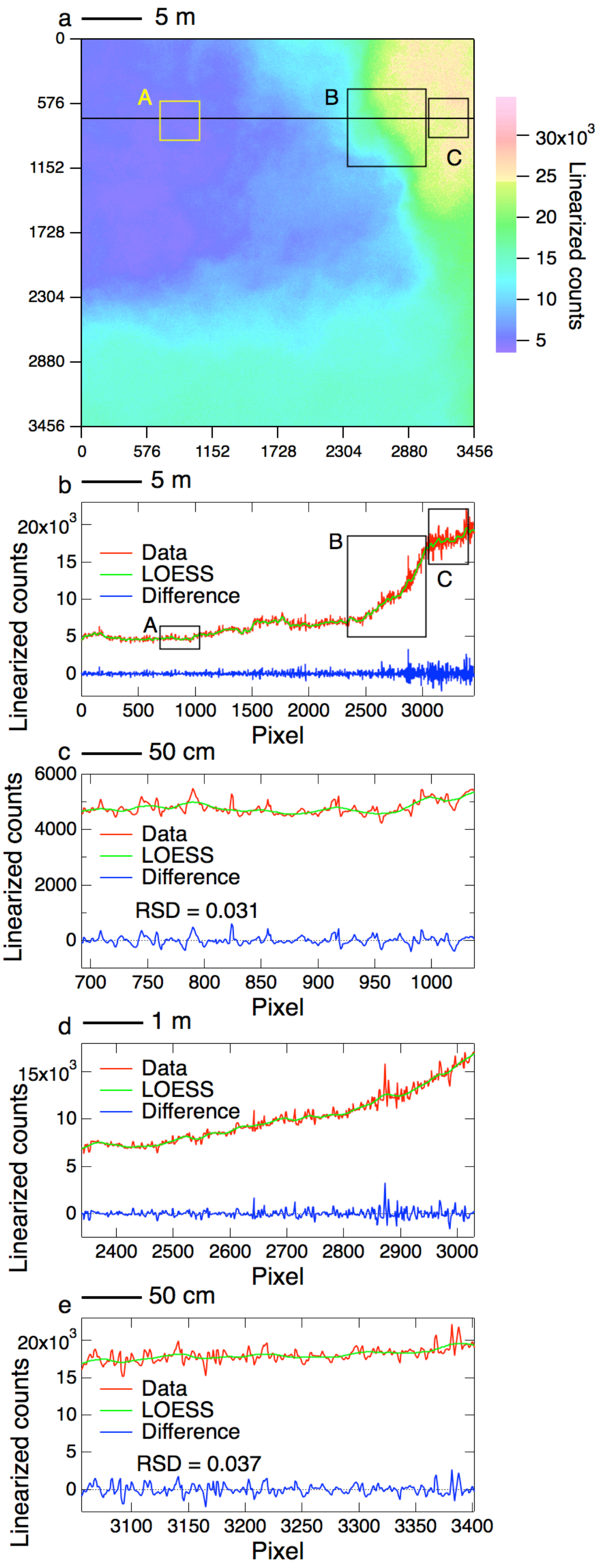

Figure S9. Examination of noise in cloud photograph. (*a*) False color image of linearized counts from image 1041; horizontal line shows locus of line profile in panel *b*, and boxes show loci of line profiles in panels *c*-*e*. RSD denotes relative standard deviation evaluated as standard deviation of difference divided by mean of the data.

S2.5 Sensitivity of retrievals of COD to uncertainty in C_{min} and C_{max}

Uncertainty in counts in a given pixel arising from sensor noise will propagate pointwise into uncertainty in retrieved COD. More important is the possibility of systematic error arising from mis-determination of the minimum and maximum count rates that will affect all the retrievals via Eq. (2). The magnitude of this systematic error was assessed by decreasing the value of C_{max} by 2.5% and by increasing the value of C_{min} by 2.5%, the magnitudes of the changes being given by the uncertainty associated with sensor noise discussed in Section S2.4. The results, Figure S10, determined using the RT results for cosine of the solar zenith angle 0.85 given in Figure 2, show that the change in retrieved COD due to increase in C_{min} by that amount is negligible through the entire count range. For the decrease in C_{max} there is a small but appreciable increase in retrieved COD, increasing with increasing number of counts, to about 0.4 in both the red and blue channels for COD = 3, the maximum retrievable value for this quantity. The corresponding fractional error that would result from decreasing the value of C_{max} by 2.5% ranges from -0.02 at low count number to about -0.12 at the count number corresponding to COD = 3.

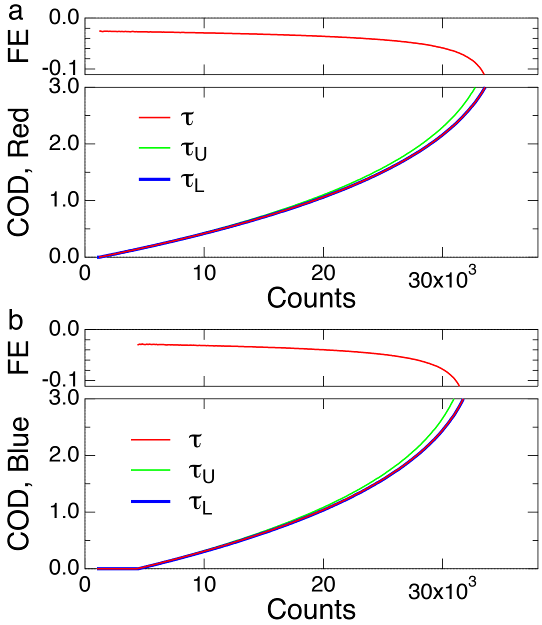

Figure S10. Examination of sensitivity of retrieved COD to maximum and minimum counts in (*a*) red and (*b*) blue channels. Red curves (τ) denote retrieved COD assuming accurate determination of count rates, C_{max} and C_{min} corresponding to maximum and minimum normalized zenith radiance as given by the radiative transfer calculations. Green curves (τ_{U}) denote retrieved COD when C_{max} is diminished by 2.5%; blue curves (τ_{L}, essentially identical to red curves) denote retrieved COD when C_{max} is increased by 2.5%. Upper panels denote fractional error FE in retrieved value of COD that would result from identifying the value of C_{max} erroneously high by 2.5% because of noise contributions to measured counts. Calculations were carried out for cosine of the solar zenith angle equal to 0.85.

S3 Deployment

Cameras were deployed on tripods facing upwards, Figure S11. Cameras were oriented to vertical within 0.1˚ (1.7 mrad) using an electronic level and oriented to North within 1˚. Cameras were located within 2 m of the Doppler Lidar. At the time of the photograph cameras were shaded by a structure to the left, but later in the day they were subjected to direct sunlight. Tubes mounted on the lenses prevented sunlight from hitting the lens directly. Cameras were powered by internal battery, which lasted about 4 hours (~ 4000 images). Cameras were triggered every 4 s by an external trigger. Size of each raw image is about 25 Mbyte, corresponding to ~25 Gbyte per hour or ~100 Gbyte per 4-h deployment; data were stored on 128 Gbyte SDXC (Secure Digital eXtended Capacity) memory cards. As the cameras were unattended, they were deployed mid morning preferentially on days without likelihood of rain. The Fujifilm Finepix S1 camera, also shown in Figure S11 with zoom lens fully extended, is stated to be water and dust resistant.

Figure S11. *Left*, deployment of cameras at ARM Southern Great Plains Site in north central Oklahoma. Tubes mounted on lenses prevent direct solar beam from hitting the lens. At rear is Doppler Lidar. *Right*, camera with zoom lens fully extended to 1200 mm 35-mm equivalent focal length (actual focal length 215 mm for the so-called 1/2.3-inch (6.17 × 4.55 mm) sensor).

Orientation of the camera relative to solar position over the course of a day is shown in Figure S12. Minimum solar zenith angle SZA is 18.4˚ (321 mrad) well greater than half FOV of 15 mrad for NFOV camera and 80 mrad for WFOV camera; note that sun diameter and FOV for NFOV camera are shown in the figure at 10 times actual angular dimension as actual angular diameter of NFOV camera, also shown, is difficult to discern. Over the time period encompassed by the images shown in Figure 7, 16:33 to 16:40 UTC, cos(SZA) ranged from 0.841 to 0.853 and was treated in the analysis as constant at 0.85.

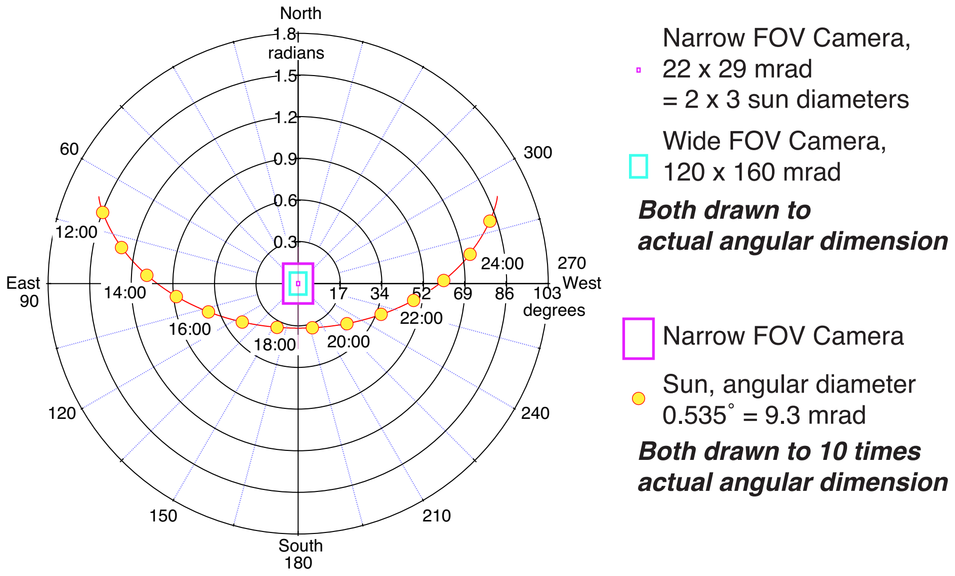

Figure S12. Solar zenith and azimuth angles as function of time of day (GMT) for July 31, 2015; local sun time lags GMT by 6.5 h.

S4 Doppler lidar, aerosol optical depth, irradiance time series and soundings

Several data sets taken at the Department of Energy Atmospheric Radiation Measurement Central Facility in Lamont OK were utilized here to provide context for the camera measurements, as presented in the text and further here.

Figure S13 shows time series of the attenuated backscatter and vertical velocity from the Doppler Lidar and of aerosol optical depth AOD from the MFRSR. Over the course of the hour the aerosol layer was more or less constant and is thus likely a widespread, transported aerosol. The strong return at 16:00 - 16:06 and again after 16:44 are evidently instances of increased relative humidity or incipient cloud formation. The time period of the images shown in Figure 4, 16:33 to 16:40 UTC, and discussed in the paper and shown in Figures 5 and S13 encompassed instances of well defined single level cloud at about 2 km followed by a period of no strong return, as well as periods of return from the layer at about 1.5 km and the layer at 2 km. Subsequent to 16:40 and again 16:48 – 16:52 there is indication of modest convective activity associated with a new, lower cloud layer forming at the top of the aerosol layer at about 800 m.

Both the MFRSR and the Cimel sunphotometer require line of sight to the sun, as the direct solar beam intensity is recorded by the instrument. Optical depth at 500 nm of 0.4 - 0.5 (16:15 – 16:29; 16:35 – 16:40) is taken as that of the humidified aerosol layer despite intermittent indication of overhead clouds which clouds are evidently not obscuring the direct solar beam). Higher optical depths. 4 - 5, are attributed to thin clouds. This ascription is supported by decrease in Ångström exponent from about 1, indicative of moderate wavelength dependence, consistent with humidified aerosol particles, to about 0, wavelength independent, characteristic of clouds. The lack of exact registration of the lidar with the presence of clouds in the MFRSR signal is a consequence of the lidar looking vertically upward, whereas the solar zenith angle is 32°, as well as displacement of the instruments, about 50 m. Similar magnitude AOD signal is found in measurements by the MFRSR and the Cimel sunphotometer (measurement interval nominally 15 min) over a more extended period, 15:00 – 1800, Figure S14; absence of AOD measurement by the Cimel sunphotometer indicates that the instrument was unable to detect the solar disk and the measurement was aborted.

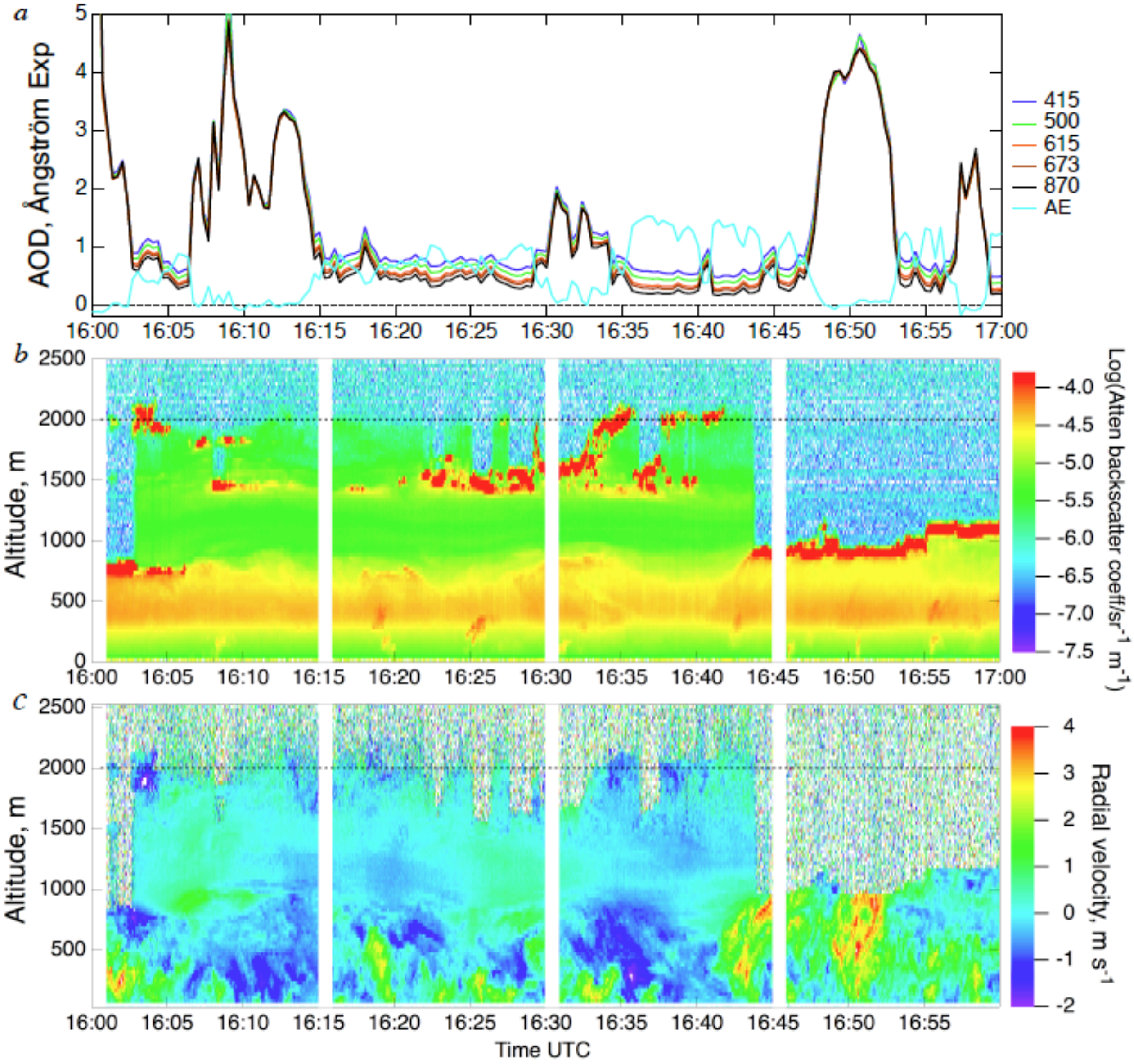

Figure S13. Time series of MFRSR and Doppler Lidar signals for 16:00 to 17:00 UTC; local sun time is UTC - 6.5 h. (*a*) Aerosol or cloud optical depth for indicated wavelengths (nm) and Ångström exponent AE. (*b*) Attenuated backscatter coefficient. (*c*) Vertical velocity. Dashed line denotes cloud height 2 km.

Surface irradiance measured by three instruments, shaded and unshaded pyranometers and normal incidence pyrheliometer, is also shown in Figure S14. Direct solar irradiance, evaluated as the product of direct normal solar irradiance times cos(SZA) shows a rather smooth envelope punctuated by periods of near zero irradiance that coincide closely with instances of high optical depth measured by the MFRSR, consistent with intermittent obscuration of the sun by clouds. Diffuse downwelling shortwave irradiance exhibits a rather smooth contour, consistent with thin and/or broken clouds. Hemispheric downwelling shortwave irradiance exhibits an envelope that is likewise punctuated by decreases attributed to cloud obscuration of the direct solar beam. The value of the envelope of hemispheric irradiance at the time of the measurements examined here in detail, 16:33 to 16:40, about 1100 W m^{-2}, is used to estimate cloud radiative effect.

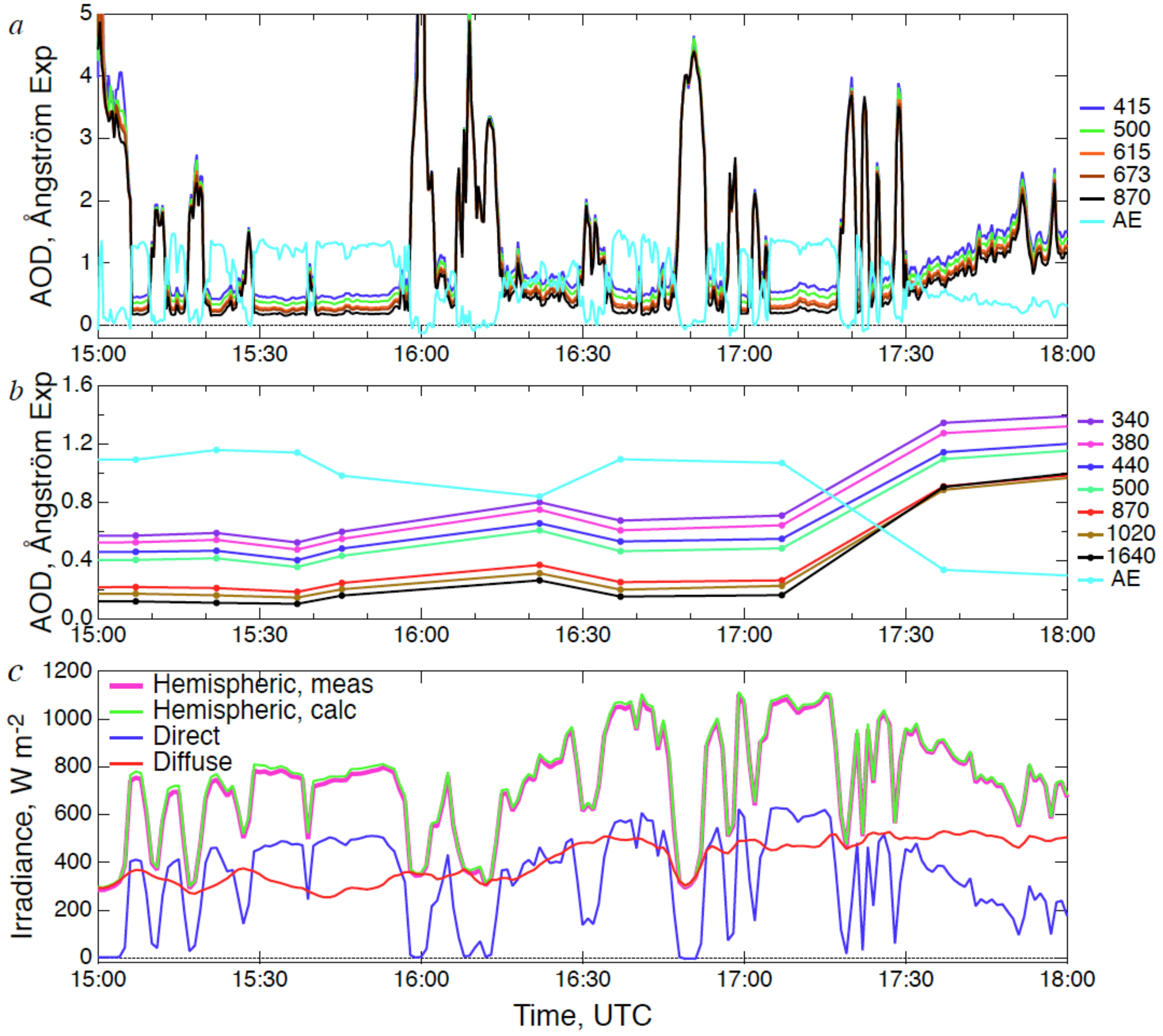

Figure S14. Time series of MFRSR, Cimel sunphotometer, and irradiance components for 15:00 to 18:00 UTC; local sun time is UTC - 6.5 h. (*a*) MFRSR and (*b*) Cimel aerosol or cloud optical depth for indicated wavelengths (nm) and Ångström exponent AE. (*c*) Hemispheric measured irradiance, unshaded pyranometer; hemispheric diffuse irradiance, shaded pyranometer; direct solar irradiance, pyrheliometer times cos(SZA); hemispheric irradiance calculated as sum of diffuse plus direct.

Balloon-borne radiosondes regularly launched at the SGP site provided information on the vertical structure of temperature, relative humidity, and dew point, atmospheric stability, and wind speeds, Figure S15. As noted in the text (Section 5.1) the relative humidity and dew point were consistent with clouds present only below 2 km, and the wind speeds were consistent with those inferred from angular translation velocity of the clouds together with cloud height determined by the Doppler Lidar.

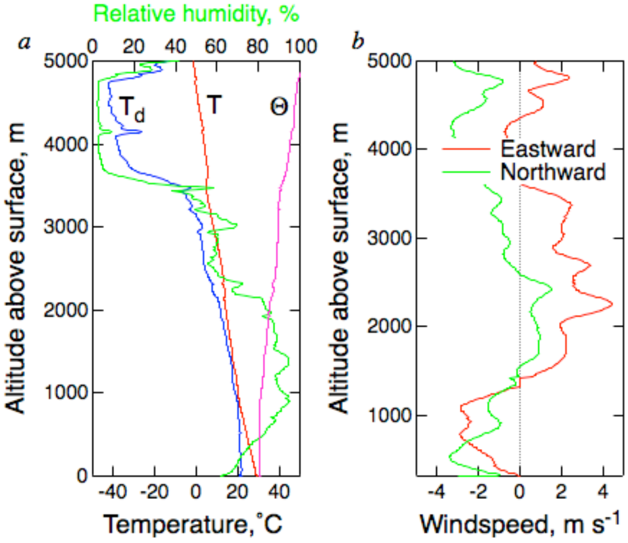

Figure S15. Sounding of (*a*) temperature *T*, potential temperature Θ, dew point temperature, T_d, and relative humidity vs. altitude for balloon launch, at SGP site, at 17:30 UTC, and (*b*) eastward and northward wind speeds evaluated from drift rate of sonde.

In sum these measurements support the interpretation in the text of the time period 16:33 to 16:40 as one of relatively stable boundary layer air with stable or modestly dissipating cloud intermittently at 2 km and 1.5 km.